INFORMATION TO USERS

This manuscript has been reproduced from the microfilm master. UMI films the text directly from the original or copy submitted. Thus, some thesis and dissertation copies are in typewriter face, while others may be from any type of computer printer.

The quality of this reproduction is dependent upon the quality of the copy submitted. Broken or indistinct print, colored or poor quality illustrations and photographs, print bleedthrough, substandard margins, and improper alignment can adversely affect reproduction.

In the unlikely event that the author did not send UMI a complete manuscript and there are missing pages, these will be noted. Also, if unauthorized copyright material had to be removed, a note will indicate the deletion.

Oversize materials (e.g., maps, drawings, charts) are reproduced by sectioning the original, beginning at the upper left-hand corner and continuing from left to right in equal sections with small overlaps. Each original is also photographed in one exposure and is included in reduced form at the back of the book.

Photographs included in the original manuscript have been reproduced xerographically in this copy. Higher quality 6" x 9" black and white photographic prints are available for any photographs or illustrations appearing in this copy for an additional charge. Contact UMI directly to order.

UMI

A Bell & Howell Information Company
300 North Zeeb Road, Ann Arbor MI 48106-1346 USA
313/761-4700 800/521-0600

UNIVERSITY OF OKLAHOMA

GRADUATE COLLEGE

ELECTRODE MATERIALS FOR LITHIUM RECHARGEABLE BATTERIES: SYNTHESIS, SPECTROSCOPIC STUDIES AND ELECTROCHEMICAL PERFORMANCE

A DISSERTATION

SUBMITTED TO THE GRADUATE FACULTY

in partial fulfillment of the requirements for the

degree of

DOCTOR OF PHILOSOPHY

By

XULONG ZHANG

Norman, Oklahoma

1997

ELECTRODE MATERIALS FOR LITHIUM RECHARGEABLE BATTERIES: SYNTHESIS, SPECTROSCOPIC STUDIES AND ELECTROCHEMICAL PERFORMANCE

A DISSERTATION

APPROVED FOR THE DEPARTMENT OF CHEMISTRY AND BIOCHEMISTRY

By

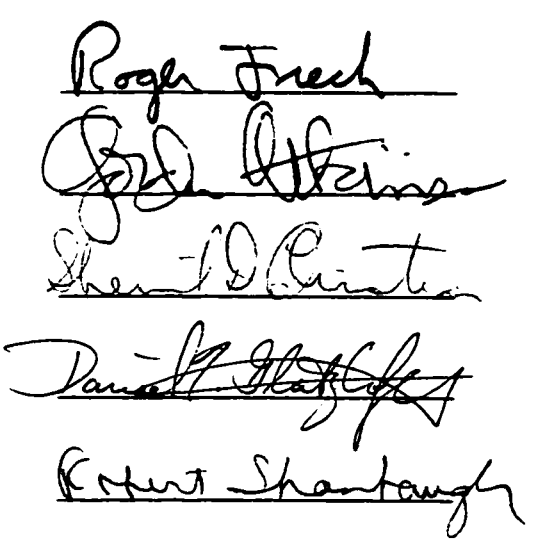

ACKNOWLEDGMENTS

I would like to express my sincere gratitude to Dr. Roger Frech for his guidance, support, encouragement, and friendship throughout my graduate study at University of Oklahoma. I have been fortunate enough to benefit from such a mentor with profound knowledge and integrity. I will always respect Dr. Frech as a scientist, teacher, and a caring individual.

I would like to extend my thanks to Drs. Sherril Christian, Daniel Glatzhhofer, Robert Shambaugh and Golden Atkinson for their advice, support and willingness to serve as members of my advisory committee. Their advice has always been invaluable to my graduate study. I especially thank Dr. Christian for his tremendous help and patience when I was his teaching assistant.

I would like to thank Dr. Masood Khan for his efforts on collecting x-ray diffraction data and solving the crystal structures of my compounds, Dr. Weaver for the powder x-ray experiment and Dr. Halterman for letting me use the Parr autoclave so I can synthesize the mesostructural materials.

I would like to thank the Department of Chemistry and Biochemistry, National Science Foundation, Army Research Office and EPSCoR, Graduate College for providing me financial assistance in terms of teaching and reserach assistantships, tuition and fee waivers and conference travel grants.

I wish to express my thanks to the present and past members of Dr. Frech's research group, Reneé Cole, Barry Klasson, Palmer Graves, Shawna Starkey, Sangmithra Chintapalli, Weiwei Huang, Gamini Dharmasena, Andy Mattioda, Corbin Zea, Chri Rhodes, Sharon Sanderson and Dave Roth. They have been extremely helpful by stimulating scientific thinking and by providing an enjoyable working atmosphere.

I feel very lucky that I can reach this point. I have been blessed with the companionship and immeasurable help of many good friends and teachers. Special thanks go to my middle school principle Huiteng Liu, high school teacher Min Zhu and my research advisor and good friend in China, Professor Yunzhang Yuan. Their encouragement and friendship are truly appreciated.

My greatest thanks go to the members of my family. I am greatly indebted to my wife, Xiaobei Qiu, for her love, understanding, support, and encouragement during the entire course of my study. Thanks to my lovely daughter for bringing joy and happiness to my life. Education is very important to my parents, although they did not have any opportunities for attending school. They have provided support in every possible way for their children's education. Their love and faith in my ability have served as my inspiration for this work. I dedicate this work to them with all my love.

TABLE OF CONTENTS

LIST of TABLES

LIST OF FIGURES

LIST OF ABBREVIATIONS

Ni-cad	Nickel-cadmium
Ah	Ampere-hours
Wh	Watt-hours
V	Volts
P	Specific energy density
I	Current
V_{oc}	Open circuit voltage
R	Resistance
EC	Ethylene carbonate
PC	Propylene carbonate
DEC	Diethylene carbonate
DMC	Dimethylene carbonate
PPP	Poly(paraphenylene)
PAc	Poly(acetylene)
PEO	Poly(ethylene oxide)
PAN	Poly(acrylonitrile)
PVDF	Poly(vinylidene) fluoride
THF	Tetrahydrofuran
TEOS	Tetraethyl orthosilicate
CTAB	Cetyltrimethylammonium bromide
IR	Infrared
NMR	Nuclear magnetic resonance
EPR	Electron paramagnetic resonance
EXAFS	Extended X-ray absorption fine structure
TEM	Transmission electron microscopy
JCPDS	Joint Committee on Powder Diffraction Standard
VO_6	Vanadium-oxygen octahedra
VO_5	Vanadium-oxygen trigonal bipyramids
w	Weak
vs	Very strong
m	Medium
s	Strong
sh	Shoulder

ABSTRACT

The lithium rechargeable battery is the newest member of the rechargeable battery family and is best known for its high energy density, long battery life, low self-discharge rate and light weight. This battery may become one of the most important energy sources in consumer market, industrial and military applications. Intercalation compounds play a critical role in determining the overall performance of a lithium rechargeable battery. The common intercalation materials for battery applications are layered structure Li_xCoO_2, spinel $Li_xMn_2O_4$ and lithium vanadium oxides, $Li_xV_2O_5$ and $Li_xV_3O_8$.

Three distinct $Li_xV_2O_5$ phases, δ, ε, and γ-$Li_xV_2O_5$, were obtained through a chemical intercalation reaction and solid state reactions. Infrared and Raman spectra were recorded for the three phases. The spectral changes were interpreted in terms of the local structural changes of the vanadium-oxygen polyhedra. Although the δ and ε phases have very similar powder x-ray diffraction patterns, IR and Raman studies showed these two phases adopt distinctive local structural environments. These results demonstrate that IR and Raman spectroscopy are important techniques for the structural analysis of intercalation materials.

Single crystals of $Li_{1.1}V_3O_8$ and $^6Li_{1.1}V_3O_8$ were prepared using solid state synthesis techniques. IR spectra and polarized Raman spectra were recorded on the $Li_{1.1}V_3O_8$ and $^6Li_{1.1}V_3O_8$ crystals and a lithiated phase, $Li_4V_3O_8$. Factor group analysis method was used to interpret the spectral changes. These spectroscopic results provide insight into the structural modifications originating from lithium intercalation/deintercalation processes.

In situ Raman spectra of $Li_xV_2O_5$ were successfully recorded on a operating lithium rechargeable battery. Distinctive spectral changes were observed at different lithium intercalation levels and interpreted in terms of the slight rearrangements of the V-O structural units. The results show that *in situ* Raman spectroscopy may become an important nondestructive technique in investigating the irreversible structural changes in electrode materials and evaluating battery performance.

For the first time novel mesostructural materials were synthesized as electrode materials for the lithium rechargeable battery. The well-ordered mesostructural materials provide an ideal host for lithium transport processes. The preliminary results on the manganese oxide-based cathode and tin oxide-based anode show that the templating synthesis technique may provide important electrode materials for battery applications.

Chapter I INTRODUCTION

1.1 General Introduction

Batteries in the marketplace are of two types: primary and rechargeable batteries, with world battery sales currently around 20 billion dollars a year. Conventional rechargeable batteries such as lead-acid, nickel-cadmium (Ni-cad), and nickel metal hydride batteries occupy a large part of the market [1]. However, increasing use of the heavy metal-containing rechargeable batteries has raised many environmental concerns. On the other hand, the miniaturization trend and rapid developments in portable electronics such as mobile phones, laptop computers, and video cameras have created an increasing demand for lightweight, compact, and high energy density batteries. In response to this demand, lithium rechargeable batteries have attracted intense interest both in fundamental research and industrial applications since the early 1970's [2-28].

The lithium rechargeable battery is best known for its high energy density, long cycling life, low self-discharge rate, and light weight. Fig. I-1 compares the gravimetric and volumetric energy densities of the lithium rechargeable battery and conventional rechargeable batteries. The most attractive merit of the lithium rechargeable battery is that the working voltage is at least two and a half times that of conventional batteries. Table I-1 summarizes some properties of different batteries.

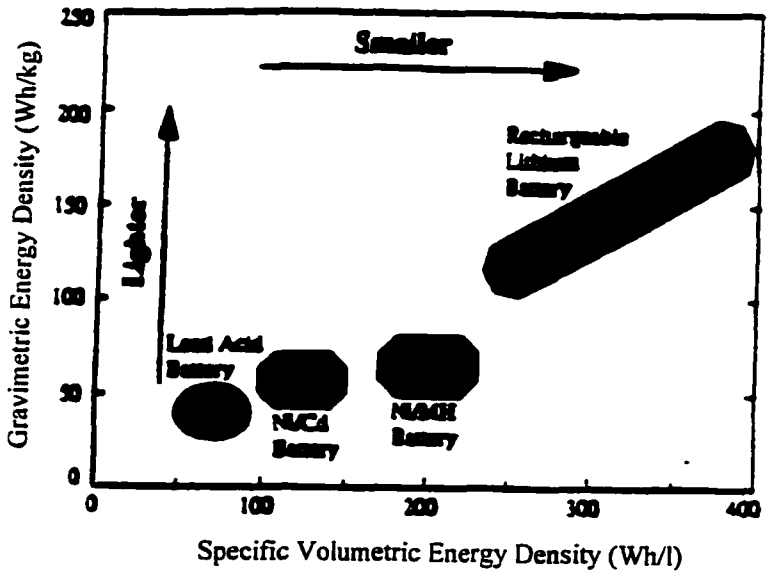

Fig. I-1 Comparison of the gravimetric and volumetric energy densities of rechargeable batteries [25]

Table I-1 Performance comparison of size AA batteries [8]

Performance	Primary alkaline	Lead acid	Secondary alkaline	Nickel cadmium	Nickel hydride	Lithium manganese	Lithium ion
Capacity (Ah/cell)	2.2	0.3	0.75	0.7	1	0.6	0.5
voltage (V)	1.25	2	1.25	1 .20	1.2	2.8	3
Wh/cycle	2.75	0.6	0.94	0.84	1.2	1.5	1.5
No. of cycles	1	400	30	400	500	200	800
Wh/all cycles	2.75	240	28	336	600	300	1200
Retail price ($/cell)	0.75	1	1.4	2.5	5	7	6.5

Ah = Ampere•hours, Wh=watt•hours

The working mechanism of a lithium rechargeable battery is based on the reversible insertion of lithium ions in solid hosts. A typical lithium rechargeable battery is schematically illustrated in Fig. I-2. An intercalation compound is used as the positive electrode and metallic Li (**A**) or another intercalation compound (**B**) such as graphite is used as the anode. Electrolytes are ion-conducting, non-aqueous solvent/lithium salt complexes or high molecular weight polymer/lithium salt complexes. Although anions may participate in the charge transport during the cell operation, Li^+ cations are the primary contributor to the ionic conductivity of the electrolyte [29, 30]. During the discharge process lithium ions form at the anode, are then transported through the electrolyte and finally intercalate into the host structures of the cathode. The opposite electrochemical process occurs during the charge cycle. The performance of a lithium rechargeable battery depends on the choice of cathode, anode, electrolyte and their interfacial behavior.

1.2 Materials Overview in Lithium Batteries.

1.2.1 Anode Materials

Metallic lithium was the natural choice as the anode in lithium rechargeable batteries due to its high specific capacity (3861 Wh/kg) and the highest electropositive potential. In the 70's and 80's, almost all lithium battery work was based on metallic Li as the anode. However the use of lithium metal presented some technical concerns. Due to its

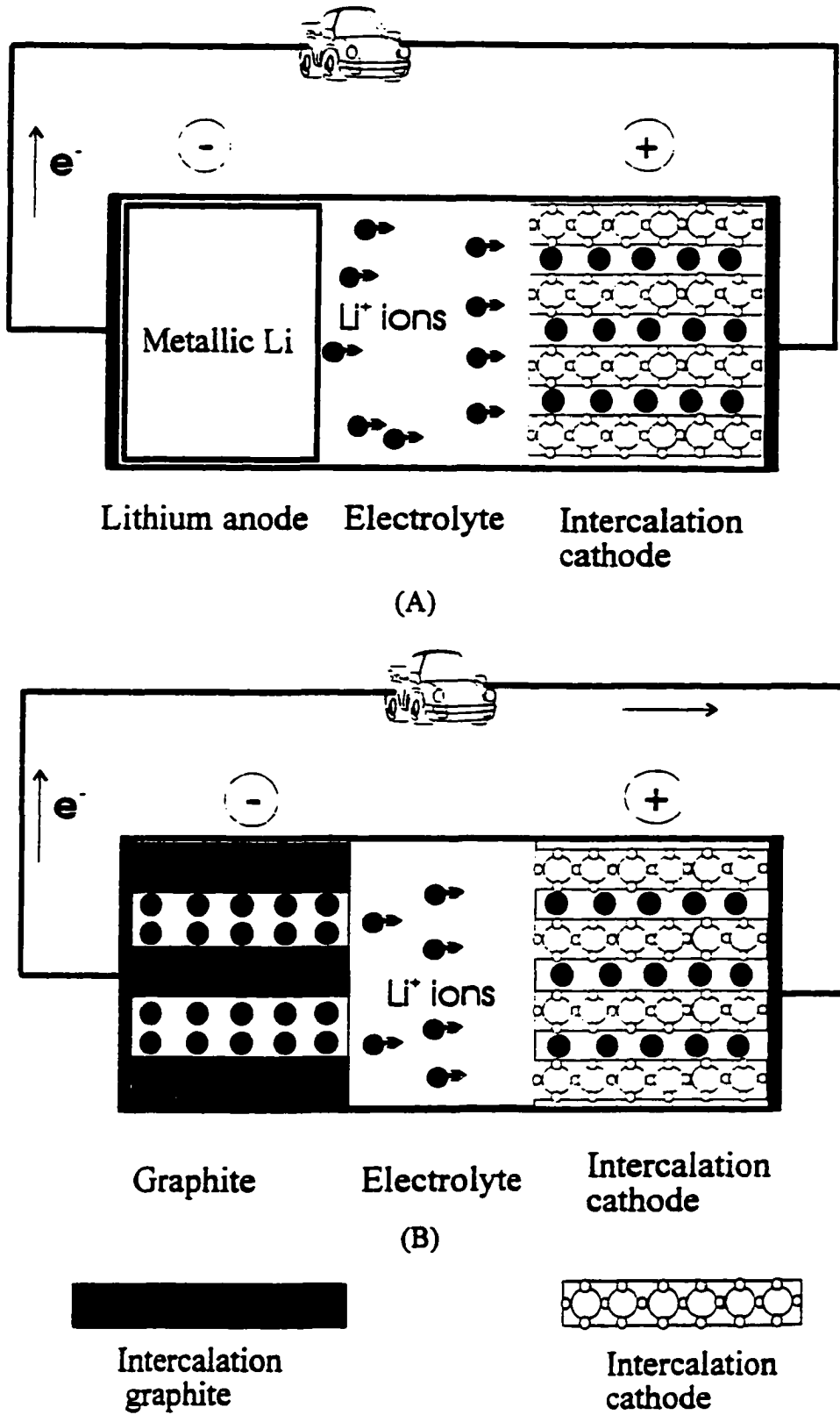

Fig. I-2 Schematic representation of (A) a lithium rechargeable battery, and (B) a rocking-chair rechargeable battery under discharge

high chemical activity, lithium may react with organic electrolytes during the storage and cycling processes and lead to the formation of dendrites and passivating layers [31]. Accumulation of dendrites and passivating layers increases the impedance on the lithium/electrolyte interface and eventually contributes to the battery failure through internal shorting [25, 32]. The use of metallic lithium as the anode in lithium rechargeable batteries has been limited by safety considerations.

The "rocking-chair" or lithium ion battery concept was proposed to cope with the disadvantages from the use of a metallic lithium anode [33-35]. In a rocking-chair battery, an insertion material is used as the cathode and another insertion material as the anode. The cell voltage is determined by the potential differences of the two insertion compounds. Lithium ions can reversibly transfer between the two electrodes and "rocking-chair" refers to the to-and-fro motion of the lithium ions during cycling. However, the lithium ion transport process does not involve oxidation of metallic lithium, nor reduction of Li^+ to Li(s). Carbonaceous materials (carbon black or graphite) have been extensively studied as the insertion anode [36-40]. The rocking-chair battery is usually assembled in the discharged state. During the charging operation, lithium ions are forced to move into the carbon layers. Six carbon atoms can accept up to one lithium atom and form the LiC_6 complex with an anode capacity of 372 Ah/kg. The working voltage and energy density of the rocking-chair battery are lower compared to the battery with a metallic lithum anode.

Improvements in safety and cyclability make the lithium ion battery especially promising. Sony Energytec first commercialized a lithium ion battery based on this concept in 1990 and it has been a great success [20, 41]. The Sony lithium ion battery uses a carbon material as the insertion anode and Li_xCoO_2 as the cathode. Other intercalation materials, such as lithium metallic alloys [42], transition metal oxides [43, 44], chalcogenides, and redox polymers [45] have also been explored as possible anodes in lithium rechargeable batteries. Fauteux and Koksbang reviewed different anodes in lithium rechargeable batteries [46]. Table I-2 lists some intercalation anode materials and their electrochemical behavior.

1.2.2 Electrolytes

The choice of the electrolyte is determined by the materials compatibility and the magnitude of the open circuit voltage of a battery. The electrolyte should not be reduced or oxidized by the electrodes. From a thermodynamic standpoint, the highest electron-donor state in the anode should lie below the lowest electron-acceptor state in the electrolyte, or the lowest electron-acceptor state in the cathode should lie above the highest electron-donor state of the electrolyte. Therefore, non-aqueous electrolytes are required for high voltage lithium batteries. In addition to high conductivity, electrolytes should be chemically stable with respect to the electrodes up to an operating voltage of 4 volts in a typical lithium battery. Organic solvents, such as ethylene carbonate (EC),

propylene carbonate (PC), diethylene carbonate (DEC) and dimethylene carbonate (DMC) are common electrolyte solutions in lithium batteries due to desirable properties such as high dielectric constants. However, their high viscosity may slow down lithium transport at low temperature. Therefore, it is a common practice to make a solvent mixture to optimize electrochemical behavior. The most suitable lithium salts are $LiAsF_6$, $LiClO_4$, $LiCF_3SO_3$, and $LiN(CF_3SO_3)_2$ [47-49]. There may be environmental concerns with $LiClO_4$.

Table I-2 Anode materials and their electrochemical properties [50]

Materials	Theorectical capacity (mAh/g)	Average voltage vs Li (V)
Li	3861	0
LiAl	790	0.36
$Li_{4.4}Si$	2012	0.2
LiC_6	372	0.5
$LiWO_2$	120	0.75
$Li_6Fe_2O_3$	799	0.9
$LiMoO_2$	168	1.5
$Li_7Ti_5O_{12}$	168	1.56
PPP[a]	190	0.7
PAc[b]	340	1.0

a: PPP = Poly (paraphenylene),

b: PAc = polyacetylene

Polymer electrolytes have been extremely attractive for use in high energy density batteries [29, 30, 51]. Polymers can be readily processed in different shapes, which provides the polymer electrolyte lithium batteries great flexibility for various applications. Poly (ethylene oxide) (PEO) has been intensively investigated for potential use in solid lithium rechargeable batteries. $LiAsF_6$, $LiClO_4$ and $LiCF_3SO_3$ are salts commonly used with the polymer [30]. Extensive research work has been underway in order to optimize the electrochemical performance of the polymer electrolytes. Further research has been focused on improvements in the room temperature conductivity, cyclability, cost, and reliability of lithium batteries.

Nonaqueous electrolyte solvents have been used with polymers such as PEO to prepare hybrid polymer electrolytes. PC and EC solvents act as plasticizers to modify the polymer dynamics, thus improving the low temperature electrochemical performance. The PEO-plasticizer, plasticizer-ion, PEO-ion and ion-ion interactions have been investigated using different techniques such as nuclear magnetic resonance (NMR) [52-54] and vibrational spectroscopy [55]. Gel electrolytes using polyacrylonitrile (PAN) [56] [57, 58] and comb-like polymers have also been used in lithium batteries. With increasing improvement of the room temperature conductivity, the polymer electrolyte lithium battery shows high promise for the future.

1.2.3 Intercalation Cathode Materials

The discovery of intercalation compounds is the cornerstone for the development of the high energy density lithium battery. A lithium intercalation compound is a solid host matrix into which lithium ions can be reversibly inserted without significant structural changes of the host. To be useful in a lithium battery, an insertion host should have a stable open structure to facilitate intercalation reactions. Transition metal dioxides and chalcogenides have been intensively explored as intercalation materials [8, 59-62]. In the close-packed oxygen or sulfur anion layers, the transition metal ions locate at the octahedral sites and lithium ions can be reversibly inserted into the octahedral or tetrahedral sites. Fig. I-3 illustrates two prime insertion structures: layered and spinel structures.

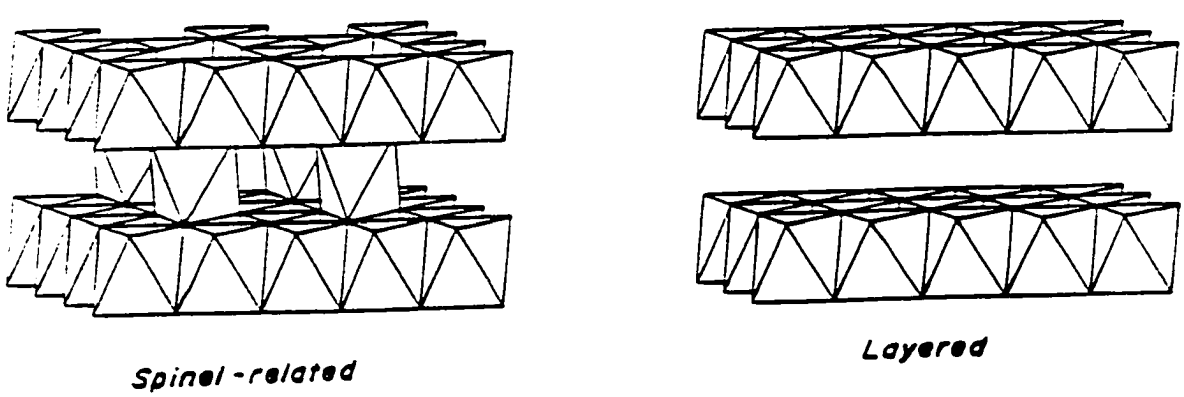

Fig I-3 The structures of intercalation compounds [63]

Li_xTiS_2 was the first intercalation compound in which a lithium intercalation reaction was demonstrated [64]. The Li_xTiS_2 structure is characterized by Ti-S polyhedra forming a layered structure. Upon insertion of lithium ions, the following reversible reaction takes place within the layers.

$$x\,Li^+ + x\,e^- + TiS_2 \Longrightarrow Li_xTiS_2 \qquad (1.1)$$

The inserted lithium ions are accommodated inside the octahedral sites, and this reaction causes only a layer expansion. The basic Ti-S layer structures remain intact during the insertion process.

Although Li_xTiS_2 is the ideal material to demonstrate the intercalation concept in lithium rechargeable batteries application, it does not have high enough voltage (2.2 V) and its practical energy density is too low (under 100 mAh/g) for practical applications. In addition, sulfide-based compounds are not stable during the charge/discharge process [65]. Therefore transition metal oxides have been the focus for use as insertion electrodes in lithium rechargeable batteries during the past two decades. Layered transition metal oxides $LiMO_2$ (M = Co, Ni, Mn, V) and spinel transition metal oxides such as $LiMn_2O_4$ are the most attractive insertion cathodes. As in the Li_xTiS_2 structure, layered compounds such as Li_xCoO_2 [20] and Li_xNiO_2 [66, 67] undergo only a slight layer expansion upon lithium intercalation. Lithium ions can reversibly transport inside the two-dimensional open layers, as shown in Fig. I-3. The spinel structure offers a three

dimensional interstitial space for lithium ion transport. Due to the cubic close-packed arrangement, the spinel structure (e.g. $Li_xMn_2O_4$) provides a remarkably stable host framework for lithium insertion/extraction reactions [60, 62, 68-75].

The family of lithium vanadium oxides, such as $Li_xV_2O_5$, $Li_xV_3O_8$, and V_6O_{13}, also appear to be very promising candidates for cathode materials [76-84]. In vanadium oxide structures, there are two types of sites, octahedral and tetrahedral, which can be utilized to accommodate the lithium ions. The potential, capacity, and structural reversibility are the three most important factors in evaluating electrode materials. Fig. I-4 shows the electrochemical potentials (*vs* Li) of various intercalation materials and Table I-3 summarizes the properties of the common cathode materials.

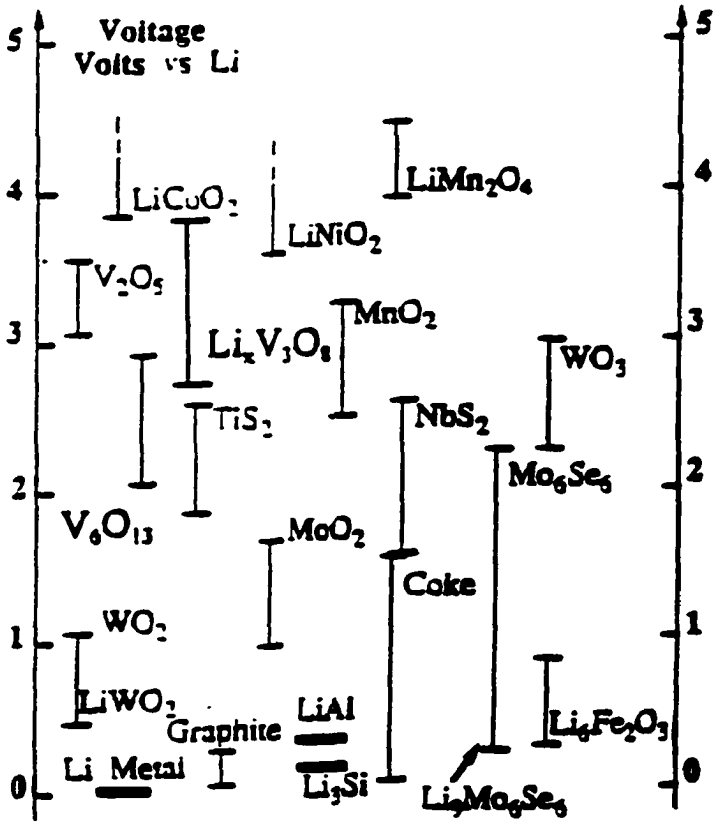

Fig. I-4 Potentials (vs Li V) of various intercalation materials [50]

Table I-3 Properties of Cathode Materials [50]

Material	Theoretical Capacity (mAh/g)	Average Voltage vs Li
$Li_{1-x}CoO_2$	274	3.9
$Li_{1-x}NiO_2$	275	3.8
$Li_{1-x}Mn_2O_4$	148	4.0
$Li_xV_2O_5$	147	3.1
$Li_xV_3O_8$	194	3.5
V_6O_{13}	188	2.3
$LiTiS_2$	225	2.2

1.3 Energy Density-Determining Parameters

Energy density is the practical power that a battery can deliver and is one of the most important properties of a battery. The specific energy density can be expressed as the following:

$$P = (I * V * t)/(\text{wt or vol}) \qquad (1.2)$$

where P = specific energy density (Wh/kg or Wh/liter)

I = working current (ampere)

V = working voltage (volts)

t = discharge time (hours)

wt = total weight of the cell (kg)

vol = total volume of the cell (liter)

Therefore the energy density-determining factors are operating voltage, working current, electrode capacity and the weight of inactive materials.

The operating voltage (V) of a cell is determined as following:

$$V = V_{OC} - IR \qquad (1.3)$$

where V_{oc} = open-circuit voltage of the cell

I = operating current

R = internal resistance of the cell

The operating voltage of a cell is limited by the open-circuit voltage (V_{oc}):

$$V_{oc} = (\mu_A - \mu_C)/(-nF) \qquad (1.4)$$

$\mu_A - \mu_C$ is the electrochemical potential difference between the anode and the cathode, n is the charge of the charge carriers and F is Faraday's constant.

The internal resistance R is determined by the ionic conductivity σ_i, the interfacial resistance R_{int}, and the resistance to the collection of the electronic transport within the electrodes R_e.

$$R = (L/\sigma_i A) + R_{int} + R_e \qquad (1.5)$$

where L/A is the thickness/area ratio of the electrolyte membrane.

The operating voltage plays a key role in determining the energy density. Transition metal oxides, such as spinel $Li_xMn_2O_4$, layered structure Li_xCoO_2 and Li_xNiO_2 possess the highest potential, around 4V (vs Li) (Fig. I-4), and have been the focus in the development of the high energy density lithium battery.

The Sony lithium ion battery uses the layered structure $Li_{1-x}CoO_2$ as the cathode, and it can be cycled for x between 0 and 0.6 with a practical energy density close to 100 Wh/kg [85]. Layered structure lithium cobalt oxide can be prepared through a solid state reaction at around 650 °C. $Li_{1-x}NiO_2$ can also be cycled with $x < 1$ with satisfactory electrochemical performance [67]. However the layered $Li_{1-x}NiO_2$ material is not easy to synthesize with stoichiometric compositions. Despite their early success in lithium ion batteries, $Li_{1-x}CoO_2$ and $Li_{1-x}NiO_2$ cathode materials are too expensive and toxic for large-scale applications. Therefore, the development of cheap and environmentally benign cathodes has been the focus for the past ten years. Extensive research has led to

the development of lithium manganese oxide and lithium vanadium oxide-based cathodes.

Spinel $Li_xMn_2O_4$ shows two plateaus at 4V ($0 < x < 1$) and 3V ($1 < x < 2$) upon lithium intercalation/deintercalation processes [9]. Vanadium oxides such as $Li_xV_2O_5$, V_6O_{13}, and $Li_xV_3O_8$ also provide moderate potentials (3.5V vs Li) upon discharge reactions. These materials have been actively investigated as the cathodes in lithium rechargeable batteries. [78, 80-84, 86-88].

The effect of the working current on the energy density is equally important as the operating voltage (equation 1.2). However, the magnitude of the working current is limited to a great degree by the conductivity of the electrolyte, the cathode/electrolyte/anode interfacial behavior and lithium ionic diffusion within the electrodes. The increase of the working current could result in a high internal I^2R loss and decrease the voltage (equation 1.3). High discharge rates can be obtained by improving the conductivity of the electrolyte and interfacial layers. The use of open structural electrodes also enhances lithium ion transport, thereby increasing the working current. Intercalation compounds are usually not good electronic conductors, therefore electron-conducting components such as carbon black are combined with these electrode materials. Polymer binders such as poly(vinylidene fluoride) (PVDF) are also added to improve the contact between the carbon and the electrode particles.

The discharge time is a measure of the capacity of the electrodes. Under a constant current, longer discharge times indicate that more lithium ions can be inserted into the cathode. The capacity is determined by the intrinsic structure of the electrode. It is critical that the insertion host material has a constant and wide range of discharge voltage. High capacity can be obtained by increasing available sites for lithium ions without unfavorable structural modifications.

In addition to the active materials such as the cathode, electrolyte and anode, electrochemically inactive materials are also involved in the manufacture of lithium rechargeable batteries. These inactive materials include current collectors, conducting wires, separation films, and sealing materials. Excessive use of the inactive constituents reduces the energy density of a battery. From the point of view of practical application, the volumetric energy density is more critical than the gravimetric energy density. Although carbonaceous materials are common anode materials in lithium batteries, their low volumetric energy density has been a main driving force in searching for alternative anodes with significantly higher volumetric and gravimetric energy densities.

1.4 Cyclability-Determining Parameters

Cyclability is another critical criterion for a rechargeable battery in the market place. Repeated charge/discharge processes lead to capacity fade and eventually battery failure. Development of *in situ* or *ex situ* examination techniques will be key to the successful development of lithium ion rechargeable batteries. Intensive research work has been focused on understanding the cause of battery failure. To date, the energy density loss in a lithium rechargeable battery can be attributed to the following:

1) Degradation of the electrolyte-lithium interface. As described in section 1.2.1, the formation of the dendrites and passivating layers reduces the contact between the electrolyte and the anode and increases the interfacial resistance. Impedance spectroscopy has been used to investigate the interfacial complex impedance changes during charge/discharge cycling. Carbonaceous materials used as the anode instead of metallic lithium improve the electrolyte/anode contact, therefore increasing the cyclability of the lithium rechargeable battery.

2) Decomposition of the electrolytes during repeated cycling. Some organic electrolyte solvents become chemically and electrochemically unstable at the high voltages attained during the charge/discharge process (>4V). For instance, propylene carbonate (PC) appears to react with the carbon anode during the battery cycling [30, 46, 68].

3) Irreversible structural modifications in both the cathode and anode. *In situ* X-ray diffraction data shows that the interlayer spacing of the carbon anode expands with increasing lithium intercalation. The fully lithiated graphite anode has a layer spacing of 3.89 Å compared to 3.52 Å for pristine graphite. Raman spectroscopy has also been used to study the lithium intercalation mechanism in the carbon anode [89, 90]. However, the effect of structural changes of the cathode material on the cyclability is one of the least understood phenomena at the present time.

Impedance spectroscopy analysis showed that the Li_xCoO_2/electrolyte interface does not undergo notable change upon repeated cycling [91]. However *in situ* X-ray diffraction data showed that Li_xCoO_2 undergoes an ordering process when x went beyond 0.6 [92]. A unusual phase transition from an orthorhombic structure to a monoclinic structure was observed during the ordering process. After the structural ordering, some cobalt atoms enter the lithium layers, which could decrease the availability of octahedral sites for lithium ions and limit lithium transport through the layers. A similar phase transition occurs in the Li_xNiO_2 cathode at x = 1. Significant structural changes are also observed in other cathode materials. The sharp potential drop from 4V to 3V of the spinel $Li_xMn_2O_4$ originates in a Jahn-Teller structural distortion. At x = 1, the crystal symmetry of $Li_xMn_2O_4$ undergoes a transition from cubic to tetragonal with a volume change of about 10% [9, 50, 60, 69, 70]. X-ray diffraction measurements have also identified structural changes of $Li_xV_2O_5$ [77, 83, 93], $Li_xV_3O_8$ [94, 95], and $Li_xV_6O_{13}$ [4] over a wide range of intercalation/deintercalation processes.

X-ray and neutron diffraction methods are, at present, the most powerful techniques for characterizing structural changes of various materials. Although *in situ* X-ray diffraction has successfully identified the evolution of the unit cell parameters of insertion materials over a wide range of x values, this powerful tool is quite limited in investigating the topotactic structural modifications induced by lithium intercalation reactions. This technical limitation is due to the following: a) from the standpoint of practical battery design, it is necessary to avoid phase transitions or big potential drops during the cycling. In other words, charge/discharge processes should only take place at single voltage plateaus, e.g. the 4V spinel $Li_xMn_2O_4$ or 3.9V Li_xCoO_2 regions, under normal operating conditions; b) during normal lithium battery operation, structural changes within the electrodes should only occur as a slight rearrangement of the M-O or M-S layers. Consequently the topotactic structural modifications and the presence of inserted lithium ions are not readily detectable by X-ray diffraction methods; c) repeated cycling may lead to self-grinding of the cathode particles which will then appear to be in an amorphous state; d) the increasing emphasis on the use of amorphous materials as the cathode will further limit the power of the X-ray diffraction method. Therefore development of new techniques is the key to successful investigation of the irreversible and subtle structural changes in the host structures.

Laser Raman and infrared spectroscopy (IR) can provide important structural information and have been powerful supplemental tools to X-ray diffraction methods.

The spectroscopic measurements are especially sensitive to local structural modifications related to small atomic displacements. It would be extremely significant to develop Raman and IR techniques as nondestructive tools to investigate lithium intercalation and storage mechanisms during the battery cycling.

1.5 Battery Life, Safety, Cost and other factors

The lithium rechargeable battery offers many technical advantages over the traditional batteries. The improvement of the cyclability will increase the operating time of lithium rechargeable batteries. This can be accomplished by optimizing battery design, improving interfacial behavior, and developing new intercalation materials. For example, a three-dimensional open structural framework would reduce diffusion barriers, therefore enhancing lithium transport performance. Due to the unique electrochemical insertion mechanism, the lithium rechargeable battery has a lower self discharge rate when compared to conventional batteries, thus a longer battery life.

Battery safety is another primary concern in the marketplace. Theoretically, solid state polymer electrolyte batteries have better safety properties because there is no heavy metal or liquid phase involved. However, the battery based on a metallic lithium anode from Moli Energy Ltd. (Canada) was recalled in 1989 due to the existence of a fire hazard. The lithium ion battery based on intercalation compounds seems to satisfy the

safety requirements and has been a great success in the competitive market. The success comes from the fact that the use of intercalation carbon materials rather than metallic lithium as the anode reduces the formation of dendrites at the electrolyte-anode interface and removes the fire hazard.

Although Li_xCoO_2 is currently the successful example of intercalation compounds in a commercial lithium rechargeable battery, the expense of this material prohibits its use in widespead competitive markets. The high toxicity of cobalt oxide is another concern for environmental protection. Therefore the discovery of new materials, optimization of existing synthesis methods and the development of new synthetic procedures might be the key for the commercialization of new inexpensive lithium rechargeable batteries [59, 78, 86, 94].

1.6 Overview of my dissertation and objectives of my research

This dissertation is divided into five chapters. Chapter one gives a brief overview of lithium rechargeable batteries emphasizing: a) the choices of cathodes, anodes and electrolytes; b) factors that govern the performance of lithium batteries; c) technical difficulties that impede the commercialization of lithium batteries; and d) battery evaluation techniques. Chapter two focuses on the fundamental aspects of lithium vanadium oxide cathodes. This chapter describes the synthesis, structural

characterization, and vibrational spectroscopic studies of several lithium vanadium pentoxide phases. The spectroscopic results from $Li_xV_2O_5$ provide a basis for *in situ* Raman spectroscopy technique for lithium battery evaluation, which is later discussed in chapter four. Chapter three presents the spectroscopic results from lithium trivanadate, $Li_xV_3O_8$. The $Li_xV_3O_8$ is an interesting cathode material and can be prepared as a single crystal. Both $Li_xV_3O_8$ and $^6Li_xV_3O_8$ single crystals were grown using solid state synthesis methods. The availability of both crystals is critical, since the FTIR and Raman spectral changes upon isotopic substitution are very useful in elucidating the lithium intercalation mechanism in insertion compounds. Chapter four describes the *in situ* Raman spectroscopic studies of $Li_xV_2O_5$ in a working lithium battery. These results shows that *in situ* Raman spectroscopy is an important technique for fundamental studies of intercalation materials and in evaluating electrochemical behavior of lithium batteries. Chapter five describes the development of the templating synthesis of mesostructural materials for high capacity cathodes and anodes in lithium rechargeable batteries. Mesostructural manganese oxides and lithium tin oxides are synthesized through hydrothermal synthesis techniques in the presence of templating molecules. The preliminary charge/discharge results show that these novel mesostructural materials possess desirable properties for applications in rechargeable lithium batteries.

References:

1. Powers, R.A. and MacArther, D., *The 1993 Review and Analysis of Battery Industry Development*, 1994, Powers Associate: Westlake.
2. Abraham, K.M. and Alamgir, M., *J. Power Sources*, **43/44** 195 (1993).
3. Abraham, K.M. and Jiang, Z., *J. Electrochem. Soc.*, **143** 1 (1996).
4. Anderman, M., *Solid State Ionics*, **69** 336 (1994).
5. Brandt, K., *Solid State Ionics*, **69** 173 (1994).
6. Dahn, J., Sleigh, A., Shi, H., Way, B., Weydanz, W., Reimers, J., *Lithium Batteries*. Industrial Chemistry Library, ed. G. Pistoia. Vol. 5. 1994, Amsterdam and London: Elsevier.
7. Fauteux, D., Massuco, A., and Shi, J., *Electrochim. Acta.*, **40** 2185 (1995).
8. Doughty, D.H., *Sampe (Sandia National Lab Report)*, **32** 75 (1996).
9. Goodenough, J.B., *Solid State Ionics*, **69** 184 (1994).
10. Gottschalk, M., *Design News*, **49** 113 (1993).
11. Halpert, G. and Surampudi, S., *Space Power*, **9** 221 (1990).
12. Jones, S.D. and Akridge, J.R., *Solid State Ionics*, **69** 357 (1994).
13. Kakuda, S., Momma, T., and Scrosati, B., *J. Electrochem. Soc.*, **142** L1 (1995).
14. Lave, L.B., Henrickson, C.T., and McMichael, F.C., *Science*, **268** 268 (1995).
15. Li, W., Dahn, J.R., and Wainwrght, D.S., *Science*, **264** 1115 (1994).
16. Maekava, Y., Myasaka, T., Kagawa, O., and Matsufuji, A., *Secondary Nonaqueous-Electrolyte Lithium Batteries with Improved Anodes, Kokai*

Tokkyo Koho, 1995, Fuji Photo Film: Japan.

17. Munshi, M.Z.A. and Owens, B.B., *Solid State Ionics*, **38** 87 (1990).

18. Munshi, M.Z.A. and Owens, B.B., *Solid State Ionics*, **38** 95 (1990).

19. Munshi, M.Z.A. and Owens, B.B., *Solid State Ionics*, **38** 103 (1990).

20. Nagaura, T. and Tozawa, K., *Prog. Battery Solar Cells*, **9** 209 (1990).

21. News, *Paper-Thin Batteries*, in *Electronics World + Wireless World*, 1997. p. 79.

22. Owens, B.B. *Rechargeable Lithium Polymer Electrolyte Battery*. in *1992 IEEE 35th International Power Sources Symposium*. 1992. Cherry Hill: Industrial Application Society.

23. Pistoia, G., ed. *Lithium Batteries, New Materials, Developments and Perspectives* Industrial Chemistry Library, ed. S.T. Sie. Vol. 5. 1994, Elservier: Amsterdam-London-New York-Tokyo.

24. Scholey, N., *Elect. & Commu. Eng. J.*, **7** 93 (1995).

25. Scrosati, B., *Nature*, **373** 557 (1995).

26. Smith, P.H., Chua, D.L., and James, S.D., *Naval Engineers J.*, **103** 158 (1991).

27. Tarascon, J.M., Gozdz, A.S., Schmutz, C., Shokoohi, F., and Warren, P.C., *Solid State Ionics*, **86/88** 49 (1996).

28. Will, F.G., *J. Power Sources*, **63** 23 (1996).

29. MacCallum, J.R. and Vincent, C.A., eds. *Polymer Electrolyte Reviews-I & II*. 1987. Elsevier: London.

30. Armand, M., *Solid State Ionics*, **69** 309 (1994).

31. Peled, E., *Lithium Batteries*, ed. J.P. Gabano. 1983, New York: Academic Press.

32. News, *Cellular phone recall may cause setback for Moli*, in *Toronto Globe and Mail*, August 15, 1989: Toronto.

33. Armand, M., *Lithium Ion Battery*, in *Materials for Advanced Batteries*, ed. by Murphy, D.W. Broadhead, J. and Steele, B.C.H. 1980, Plenum: New York. p. 145.

34. Mizushima, K., Jones, P.C., Wiseman, P.J., and Goodenough, J.B., *Mat. Res. Bull.*, **15** 783 (1980).

35. Lazzari, M. and Scrosati, B., *J. Electrochem. Soc.*, **127** 773 (1980).

36. Takami, N., *J. Electrochem. Soc.*, **142** 371 (1995).

37. Dahn, J.R., *Phys. Rev. B: Condensed Matter.*, **44** 9170 (1991).

38. Ohzuku, A., Iwakoshi, Y., and Sawai, K., *J. Electrochem. Soc.*, **140** 2490 (1993).

39. Sato, K., Noguchi, M., Demachi, A., Oki, N., and Endo, M., *Science*, **264** 556 (1994).

40. Sawai, K., Iwakoshi, Y., and Ohzuku, T., *Solid State Ionics*, **69** 273 (1994).

41. Nagaura, T., Nagamine, M., Tanabe, I., and Miyamoto, N., *Prog. Batt. Solar Cell*, **8** 84 (1989).

42. Holmes, R.W. *Alloy Anode for Lithium Battery* in *Proceedings of the ECS Symposium on Lithium Batteries*. 1984. Pennington, NJ.

43. Murphy, D.W., DiSalvo, F.J., Carides, J.N., and Waszczak, J.V., *Mat. Res. Bull.*, **13** 1395 (1978).

44. Morzili, S., Scrosati, B., and Sgarlata, F., *Electrochim. Acta.*, **30** 1271 (1985).

45. Oyama, N., Tatsuma, T., Sato, T., and Satomura, T., *Nature*, **373** 598 (1995).

46. Fauteux, D. and Koksbang, R., *J. Appl. Electrochem.*, **23** 1 (1993).

47. Blomgren, G.E., ed. *Liquid Electrolytes for Nonaqueous Batteries*. The Science of Advanced Batteries, ed. D.A. Schearson. 1995, Case Western Reserve University: Cleveland, OH.

48. Dudley, J. T., Wilkinson, D.D., Thomas, G., and Dahn, J.R., *J. Power Sources*, **35** 59 (1991).

49. Strauss, S.H., *Chem. Rev.*, **93** 927 (1993).

50. Thackeray, M.M., *Mat. Res. Soc. Proc.*, **369** 17 (1995).

51. Koksbang, R., Olsen, I.I., and Shackle, D., *Solid State Ionics*, **69** 320 (1994).

52. Berthier, C., Gorecki, W., Minie, M., Armand, M.B., Chabagn,o J.M., and Rigaud, P., *Solid State Ionics*, **11** 91 (1983).

53. Ries, M.E., Brereton, M.G., Cruichshank, J.M., Klein, P.G., and Ward, M. *Macromolecules*, **28** 3282 (1995).

54. Manning, J.P., Frech, C.B., Fung, B.M., and Frech, R.E., *Polymer*, **32** 2939 (1991).

55. Chintapalli, S., Ph.D dissertation, University of Oklahoma, 1996.

56. Watanabe, M., Kamba, M., Matsuda, H., and Tsunemi, K., *J. Polym. Sci. Polym. Phys.*, **13** 9 (1981).

57. Nazri, G.A., MacArthur, D.M., and Ogara, J.F., *Polymer Prep.*, **30-1** 430 (1989).

58. Blonsky, P.M., Schriver, D.F., Austin, P., and Allcock, H.R., *J. Am. Chem. Soc.*, **106** 6854 (1984).

59. Manthiram, A., *J. of Materials (JOM)*, **March** 43 (1997).

60. Rahner, D., Machill, S., Schlorb, H., Klob, M., and Plieth, W., *Solid State Ionics*, **86-88** 891 (1996).

61. Farrington, G.C. and Dunn, B., *Naval Res. Rev.*, **2** 27 (1985).

62. Koksbang, R., Barker, J., Shi, H., and Saidi, M.Y., *Solid State Ionics*, **84** 1 (1996).

63. Ohzuku, T., *Trantion Metal Oxides as Cathodes*, in *Lithium Batteries*, ed . by Pistoia,G.1994, Elsevier: Amsterdan. p. 205.

64. Whittingham, M.S., *Science*, **192** 1126 (1976).

65. Matsuda, Y., *J. Electrochem. Soc.*, **134** 2107 (1987).

66. Goodenough, J.B., Wickham, D.G., and Croft, W.J., *J. Appl. Phys.*, **29** 382 (1958).

67. Ebner, W., Fouchard, D., and Xie, L., *Solid State Ionics*, **69** 238 (1994).

68. Guyomard, D. and Tarascon, J.M., *Solid State Ionics*, **69** 222 (1994).

69. Miura, K., Yamada, A., and Tanaka, M., *Electrochim. Acta.*, **41** 249 (1996).

70. Gummow, R.J., Liles, D.C., and Thackeray, M.M., *Mat. Res. Bull.*, **28** 1257 (1993).

71. Huang, H. and Bruce, P.G., *J. Electrochem. Soc.*, **141** L106 (1994).

72. Tarascon, J.M. and Guyomard, D., *Electrochim. Acta.*, **38** 1221 (1993).

73. Liu, W., Farrington, G.C., Chaput, F., and Dunn, B., *J. Electrochem. Soc.*, **143** 879 (1996).

74. Barboux, P., Tarascon, J.M., and Shokoohi, F.K., *J. Solid State Chem.*, **94** 185

(1991).

75. Gao, Y. and Dahn, J.R., *J. Electrochem. Soc.*, **143** 1783 (1996).

76. McCklin, W.J., Neat, R.J., and Sandhu, S.S., *Electrochim. Acta.*, **37** 1715 (1992).

77. Delmas, C., Cognac-Auradou, H., Cocciantelli, J.M., and Menetrier, D., J. P., *Solid State Ionics*, **69** 257 (1994).

78. Liu, Y.J., DeGroot, D.C., Schindler, J.L., Kannewurf, C.R., and Kanatzidis, M.G., *Chem. Mater.*, **3** 992 (1991).

79. Manev, V., Momchilov, A., Nassalevska, A., Pistoia, G., and Pasquuali, M., *J. Power Sources*, **54** 501 (1995).

80. Gourier, D., Tranchant, A., Baffier, N., and Messina, R., *Electrochim. Acta*, **37** 2755 (1992).

81. Galy, P.J. and Hardy, A., *Acta Cryst.*, **19** 435 (1965).

82. Dickens, P.G., French, S.J., Hight, A.T., and Pye, M.F., *Mat. Res. Bull.*, **14** 1295 (1979).

83. Cocciantelli, J.M., Menetrier, M., Delmas, C., Doumerc, J.P., Pouchard, M., Broussely, M., *Solid State Ionics*, **78** 143 (1995).

84. Cocciantelli, J.M., Gravereau, P., Doumerc, J.P., Pouchard, M., and Hagenmuller, P., *J. Solid State Chem.*, **93** 497 (1991).

85. Reimers, J.N. and Dahn, J.R., *J. Electrochem. Soc.*, **139** 2091 (1992).

86. Chirayil, T., Zavalij, P., and Whittingham, M.S., *Solid State ionics*, **84** 163 (1996).

87. Costa, J.L., Morales, E., Paleo, M., and Jurado, J.R., *Eur. Polym. J.*, **32** 13

(1996).

88. Pistoia, G., Pasquali, M., Wang, G., and Li, L., *J. Electrochem. Soc.*, **137** 2365 (1990).

89. Huang, W. and Frech, R., *J. Electrochem. Soc*, **submitted** .

90. Inaba, M., Yoshida, H., and Ogumi, Z., *L. Electrochem. Soc.*, **143** 2572 (1996).

91. Ozawa, K., *Solid State Ionics*, **69** 212 (1994).

92. Reimers, J.N. and Dahn, J.R., *J. Electrochem. Soc.*, **139** 2091 (1992).

93. Cocciantelli, J.M., Menetrier, M., Delmas, D., Doumerc, J.P., Pouchard, M., and Hagenmuller, P., *Solid State Ionics*, **50** 99 (1992).

94. Manev, V., Momchilov A., Nassalevska A., Pistoia G., and Pasqali M., *J. Power. Sources*, **54** 501 (1995).

95. de Picciotto, L.A., Adendorff K.T., Liles D.C., and Thackeray M.M., *Solid State Ionics*, **62** 297 (1993).

Chapter II Vibrational Spectroscopic Studies of $Li_xV_2O_5$

2.1 Introduction

$Li_xV_2O_5$ ($0<x<1$), one of the promising cathode materials for lithium rechargeable batteries, has attracted tremendous research interest for the past few years [1-3]. Previous studies have shown that $Li_xV_2O_5$ synthesized from solid-state reactions (at about 650 °C) exists in several different phases, depending on the stoichiometry of the lithium ions (x). Murphy *et al.* [4] reported that low temperature (LT) $Li_xV_2O_5$ can be obtained through chemical or electrochemical lithium intercalation reactions. The phase diagram of the stable $Li_xV_2O_5$ phases is shown in Fig. II-1.

Several ambient temperature $Li_xV_2O_5$ phases can be directly synthesized through the lithium intercalation reaction in an acetonitrile solution:

$$V_2O_5 + xLiI \rightarrow Li_xV_2O_5 + x/2\ I_2$$

These phases are α, ε and δ-$Li_xV_2O_5$. The α–$Li_xV_2O_5$ phase occurs with $0<x<0.1$. The ε-phase exists in the range $0.30<x<0.90$ and the δ-phase appears with x between 0.90 and 1.0. The δ-$Li_{0.95}V_2O_5$ phase is reversibly transformed to ε-$Li_{0.95}V_2O_5$ at 135 °C through a first-order phase transition and then irreversibly transformed to γ-$Li_{0.95}V_2O_5$ at 350 °C [4].

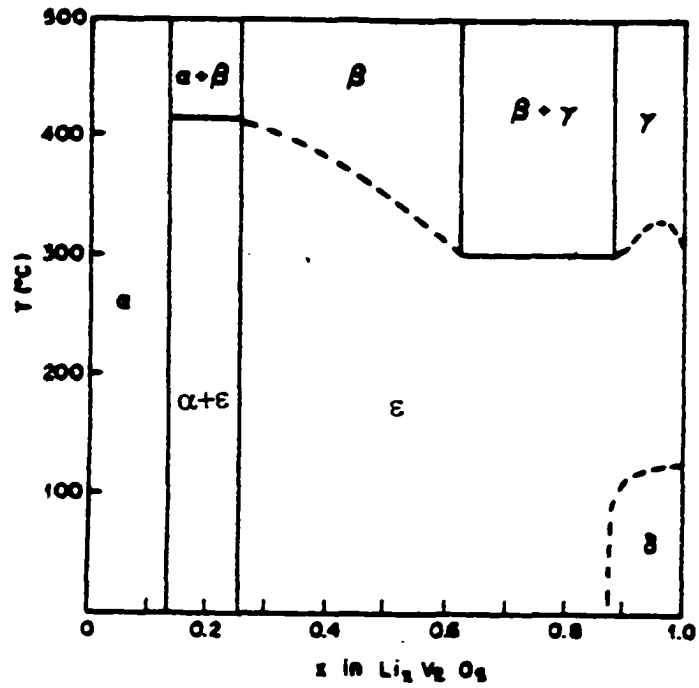

Fig. II.1 Phase diagram of $Li_xV_2O_5$ [4]

The crystal structures of the δ and γ phases have been previously solved using powder X-ray and neutron diffraction analysis [5-6]. Each vanadium atom in the δ and γ phases is coordinated with five oxygen atoms to form a distorted bipyramid as shown in Figure II-2. The bipyramids share two edges to form double-ribbon chains along the (001) direction. The double ribbons are then connected through an apex oxygen atom (O_1) to form a V-O pyramid layer. Lithium atoms are located between the layers with coordination numbers of four, five and six. The structural difference between the δ and γ phases can be easily distinguished from the powder X-ray diffraction experiments. But the ε-$Li_xV_2O_5$ structure is still elusive because its powder X-ray diffraction pattern is very similar to that of δ-$Li_xV_2O_5$ [5]. Therefore it is worthwhile to investigate the structural relationship between the three phases.

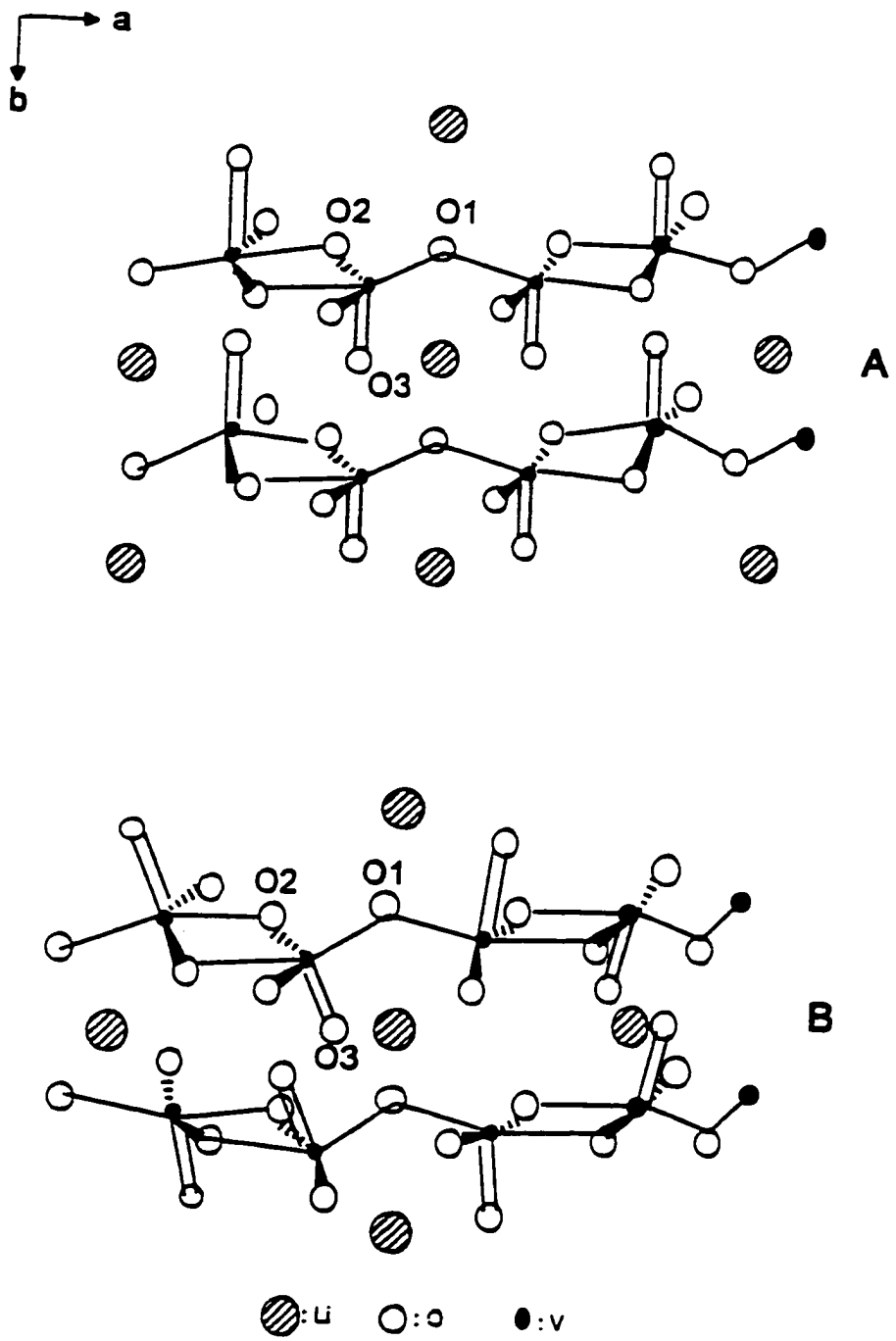

Fig. II-2 Schematic representation of the $Li_xV_2O_5$ structures,

A) δ-$Li_xV_2O_5$ B) γ-$Li_xV_2O_5$

According to Murphy *et al*, the enthalpy of the δ to ε phase transition at 135 °C is about 5 kJ/mol. This small enthalpy change may result, not from significant displacements of the V-O layers, but rather from the slightly shifted local arrangements of the pyramids, thereby offering an explanation as to why the phase transition cannot be detected using X-ray diffraction methods. In systems such as this, infrared (IR) and Raman spectroscopy can be important complementary tools to provide structural information about materials. Steger [7-8] noticed that IR spectra of V_2O_5 host structures were very sensitive to insertion of lithium ions and reported the spectra of several high temperature $Li_xV_2O_5$ phases. Cazzanelli *et al.* [9] pointed out that Raman scattering spectroscopy is a useful tool to study lithium intercalation processes in cathode materials. Recently, Porotnikov [10] reported that high temperature lithium vanadium oxides, e.g. α, β, and γ $Li_xV_2O_5$ can be distinguished using IR and Raman spectroscopy. Huang and Frech [11] also reported that the low temperature (LT) and high temperature (HT) forms of lithium cobalt oxide, $LiCoO_2$, can be unambiguously distinguished using Raman spectroscopy. This paper will describe the IR and Raman spectra of LT $Li_xV_2O_5$, e.g. the δ, ε and γ phases. Factor group analysis of the normal modes will be employed to interpret the spectra.

2.2 Experimental

2.2.1 Sample Preparation

The δ-$Li_xV_2O_5$ was the starting material and it was synthesized through the chemical intercalation reaction described by Murphy *et al.* [4]. 5 g of freshly prepared V_2O_5 powder (decomposed at 400 °C from NH_4VO_3, Johnson Matthey) was added to 50 ml of 2.5 M LiI (Alfa Aesar) acetonitrile solution. The resulting suspension was stirred at room temperature for 24 hours. The product was then separated using supercentrifugation, thoroughly washed with acetonitrile, and dried at 105 °C under vacuum for six hours. The amount of lithium ion (x) in Li_xV2O5 was determined by titrating iodine (I_2) with a standard Na_2SO_3 solution. The dried δ-$Li_xV_2O_5$ sample was a fine, dark blue powder. The iodine titration data showed the δ-$Li_xV_2O_5$ with a stoichiometric composition of $Li_{0.95}V_2O_5$. This composition was further confirmed from coulomb titration experiments on a lithium battery based on the γ-$Li_xV_2O_5$ cathode. The ε and γ-$Li_{0.95}V_2O_5$ phases were obtained by heating the δ phase to 135 and 365 °C, respectively, under nitrogen atmosphere.

2.2.2 Powder X-Ray Diffraction Measurements

Powder X-ray diffraction measurements were carried out using a Rigaku DMAX diffractometer with Cu K_α radiation (λ=1.5424 Å) monochromated by a graphite crystal. The sample was ground to a fine powder with particle sizes around 5 -10

microns and pressed onto a glass sample holder. The diffraction experiment was performed between 5 and 70 degrees (2θ) with a step size of 0.05 degree.

2.2.3 Differential Scanning Calorimetry

Differential scanning calorimetry (DSC) data were collected using a Metler-Toledo DSC-820 calorimeter. A ca. 6-10 mg sample was sealed in a specially designed 40 mL aluminum pan and heated from 20 °C to 500 °C under a constant nitrogen flow (flowing rate of 87 ml/min) The heating rate was 10 °C/min.

2.2.4 Infrared Spectroscopy

IR spectra were recorded using a Bruker IFS66V infrared system in the range 400 to 4000 cm^{-1}. The samples were prepared as KBr pellets and the sample chamber in the spectrometer was evacuated to about 100 Pa.

2.2.5 Raman Spectroscopy

Raman spectra were collected using a Jobin-Yvon T64000 Raman spectrometer. An argon ion laser (514.5 nm) and a krypton ion laser (647.1 nm) were used as the excitation sources. Holographic notch filters (Kaiser Optics) centered at 514.5 and 647.1 nm were used with the Raman system in the single monochrometer mode. A thermoelectrically-controlled CCD detector measured the scattering intensity. All Raman spectra were collected in a backscattering geometry through an 80x microscope which reduced the laser beam to a 2μ diameter spot. Most spectra were measured with

the 647.1 nm laser line, while the spectra at low frequency (100 to 400 cm^{-1}) were measured with the 514.5 nm laser line due to the poor resolution of krypton laser line in this range. The three lithium vanadium oxides were prepared as powders and varied from dark blue to black in color. Because prolonged illumination with the laser beam resulted in decomposition of the original compounds, all Raman spectra were collected with a laser intensity below 10 mW, and the samples were visually checked with the microscope for damage after measurement. An additional concern is the optical anisotropy of the compounds. To see if this effect was significant, several Raman spectra from different areas across the sample surface were measured and compared. These Raman spectra appeared to be identical.

2.3 Results and Discussion

2.3.1 Thermal Analysis

DSC measurements showed that $Li_{0.95}V_2O_5$ undergoes two phase transitions between 20 and 600 °C (Fig. II-3). The phase transition at 135 °C is a reversible transformation with an enthalpy of 5.8 kJ/mol and is associated with the structural change from the δ to the ε phase. The second phase transition at 365 °C is an irreversible transformation from the ε phase to the γ phase with an enthalpy change of 19.9 kJ/mol. These observations are in good agreement with data reported by Murphy *et al.* [4].

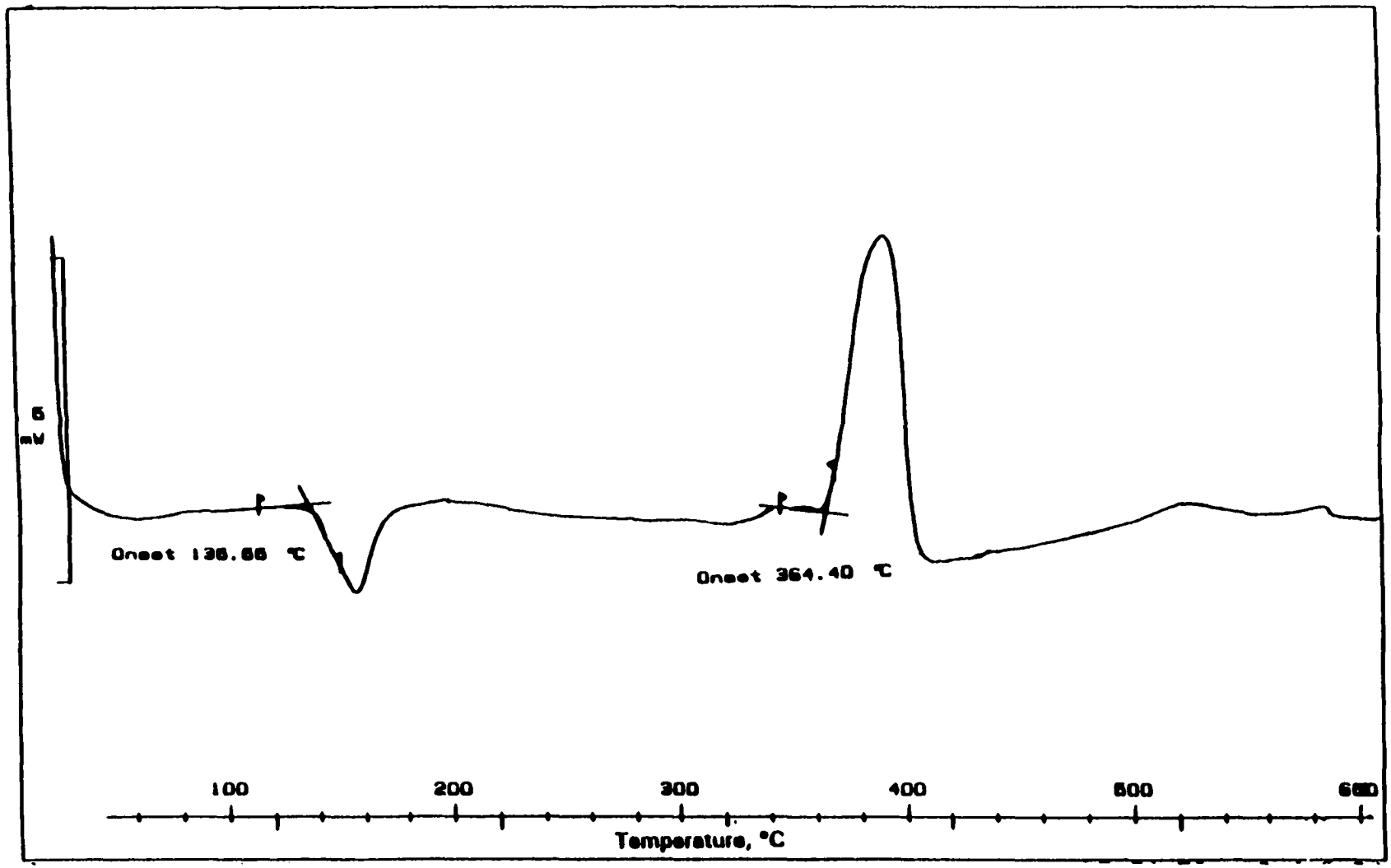

Fig. II-3 DSC spectrum of d-Li0.95V2O5. The phase transition temperatures are marked on the curve

2.3.2 X-Ray Diffraction

The powder X-ray diffraction results are shown in Figs. II-4 through II-6 and diffraction peaks are listed in Table II-1. The diffraction patterns for the δ and ε phases appear to be

Table II-1 X-ray diffraction data of $Li_{0.95}V_2O_5$

δ-$Li_{0.95}V_2O_5$	δ-$Li_{0.95}V_2O_5$	ε-$Li_{0.95}V_2O_5$	ε-$Li_{0.95}V_2O_5$	γ-$Li_{0.95}V_2O_5$	γ-$Li_{0.95}V_2O_5$
d (obsd, Å)	d (calcd, Å)[a]	d (obsd, Å)	d (calcd, Å)[a]	d (obsd, Å)	d (calcd, Å)[b]
5.622 w	5.636 w	5.658 w	5.667 w	5.304 vs	5.33 s
4.951 vs	4.971 vs	4.871 vs	4.883 vs	4.818 m	4.84 m
4.537 m	4.548 m	4.523 m		4.655 w	4.67 w
				4.392 w	4.42 w
3.712 w	3.728 w	3.667 w	3.610 w	3.330 w	3.32 w
3.386 m	3.389 m	3.348 m	3.342 m		
3.246 s	3.245 s	3.206 s		3.212 s	3.22 s
2.991 m	2.997 m	2.957 m	2.941 s	3.082 m	3.09 m
				2.847 m	2.85 m
2.811 m	2.818 m	2.786 m	2.763 m	2.782 w	2.78 w
			2.602 w	2.757 m	2.76 m
2.512 w	2.517 w	2.493 w	2.545 vw		
2.476 w	2.485 w	2.456 w			
2.171 w	2.167 w	2.147 vw	2.193 w	2.199 w	2.20 w
2.101 w	2.103 w	2.054 w	2.029 w	2.081 w	2.08 w
1.975 w	1.973 w		1.990 w	1.980 w	1.98 w
			1.961 w	1.959 m	1.96 m
1.870 w	1.879 m	1.868 w	1.869 w		
				1.801m	1.79 m
1.757 m	1.757 m	1.745 m	1.752 m	1.758 w	1.74 w
1.692 w	1.694 w	1.682 w	1.672 w	1.658 w	1.67 w

a: cited from reference #4

Fig. II-4 Powder X-ray diffraction pattern of δ-$Li_xV_2O_5$

Fig. II-5 Powder X-ray diffraction pattern of ε-$Li_xV_2O_5$

Fig. II-6 Powder X-ray diffraction pattern of γ-$Li_xV_2O_5$

almost identical, with the only difference being a shift of the characteristic diffraction of the ε phase to higher angles, implying a shrinkage of the unit cell. This observation was also reported by Cava *et al* [5]. The γ phase shows a number of additional peaks compared to the δ and ε phases, indicating a major structural change in the oxygen-vanadium layers. It is worthwhile to employ other tools to understand the structural transformation occurring at 135 °C.

2.3.3 Vibrational Spectroscopic Study

A. Symmetry-Based Normal Mode Analysis

Factor group analyses of normal vibrational modes are employed to evaluate the vibrational spectra in the different phases. The δ-$Li_{0.95}V_2O_5$ compound belongs to space group C_{mcm} (D_{2h}^{17}) with Z equal to 4 [5]. Li and O_3 atoms occupy 4c positions with site symmetry C_{2v}. The correlation between the site group C_{2v} and the factor group D_{2h} is illustrated in Table II-2

The irreducible representations for Li and O_3 atomic motion can be derived using standard factor group correlation methods [12]:

$$\Gamma(Li)=\Gamma(O_3)=A_g+B_{1g}+B_{3g}+B_{1u}+B_{2u}+B_{3u}$$

Table II-2 Correlation between site group C_{2v} and factor group D_{2h}

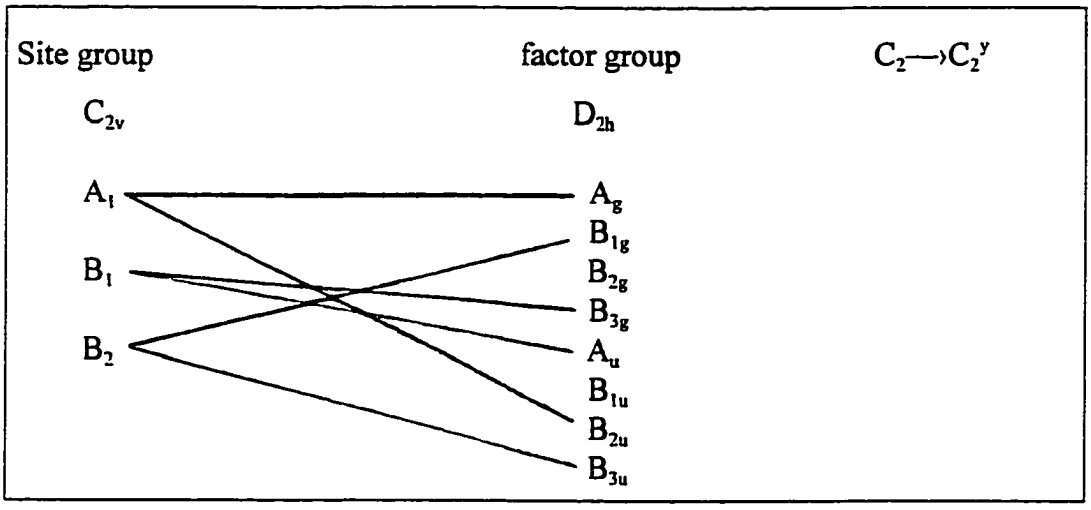

On the other hand, the V, O_1 and O_2 atoms sit in the 8f positions with site symmetry C_s. The correlation between the site group C_s and the factor group D_{2h} is shown in Table II-3. Therefore the irreducible representations for the motions of these atoms can be expressed as:

$$\Gamma(V)=\Gamma(O_1)=\Gamma(O_2)=2A_g+2B_{1g}+2B_{2u}+2B_{3u}+B_{2g}+B_{3g}+A_u+B_{1u}$$

Table II-3 Correlation between site group C_s and factor group D_{2h}

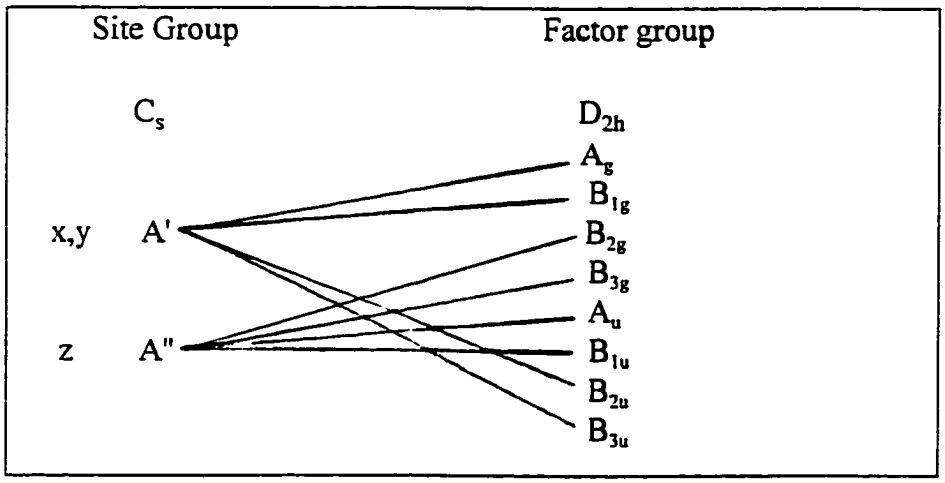

The irreducible representation structure of the vibrational modes are obtained from the contributions of each atom (Li, V, O_1, O_2 and O_3).

$$\Gamma_{vib}=\Sigma_i\ \Gamma(i)=8A_g+8B_{1g}+3B_{2g}+5B_{3g}+3A_u+5B_{1u}+8B_{2u}+8B_{3u}$$

$$\Gamma_{acoustic}=B_{1u}+B_{2u}+B_{3u}$$

Thus the optical vibrational modes can be obtained from $\Gamma_{vib.optic}=\Gamma_{vib}-\Gamma_{acoustic}$:

$$\Gamma_{vib.optic}=8A_g+8B_{1g}+3B_{2g}+5B_{3g}+3A_u+4B_{1u}+7B_{2u}+7B_{3u}$$

According to the selection rules for the D_{2h} group, all the *g* modes are Raman active and all the *u* modes but B_u modes are IR active. Therefore 24 Raman active modes and 17 IR active modes are expected.

The compound γ-LiV_2O_5 belongs to space group $P_{na2_1}(C_{2v}^9)$ with Z=4 [6]. All atoms occupy 4a positions with site symmetry C_1. The irreducible representation structure of vibrational modes can be obtained using a similar procedure as above:

$$\Gamma(Li)=\Gamma(V)=\Gamma(O)=A_1+A_2+B_1+B_2$$

$$\Gamma_{vib.optical}=23A_1+24A_2+23B_1+23B_2$$

All the vibrational modes are Raman active, while all the modes but A_2 are IR active. Therefore as many as 93 Raman bands and 69 IR absorption bands are expected in the vibrational spectrum.

B. Spectra and Analysis

Figure II-7 shows the IR spectra of the δ, ε and γ phases, along with that of pure V_2O_5 in the high frequency region, 800-1100 cm^{-1}. Modes in this region are believed to originate in the vanadium-oxygen stretching vibrations [7,10]. The spectra show interesting differences between the various phases. First, the strong broad band at 825 cm^{-1} in V_2O_5 disappears in the three lithiated phases. The general intensity of the strong, sharp peak at 1021 cm^{-1} in V_2O_5 remains relatively unchanged in the lithiated phases, but the peak position shifts to 1024 cm^{-1} in the δ phase, 1007 cm^{-1} in the ε phase and further splits into two bands, at 1006 and 1000 cm^{-1} in the γ phase. The weak shoulder at 982 cm^{-1} in V_2O_5 develops into a sharp band at 974 cm^{-1} in the δ phase and appears as a weak sharp band at 972 cm^{-1} in the ε and γ phases. A very weak feature is seen at 946 cm^{-1} in the δ phase. This weak band appears as a strong sharp band at 955 cm^{-1} in the ε and γ phases. The ε and γ phases present very similar profiles in this region, with the exception of some fine structure around 900 cm^{-1} in the ε phase and the more distinct splitting around 1000 cm^{-1} in the γ phase.

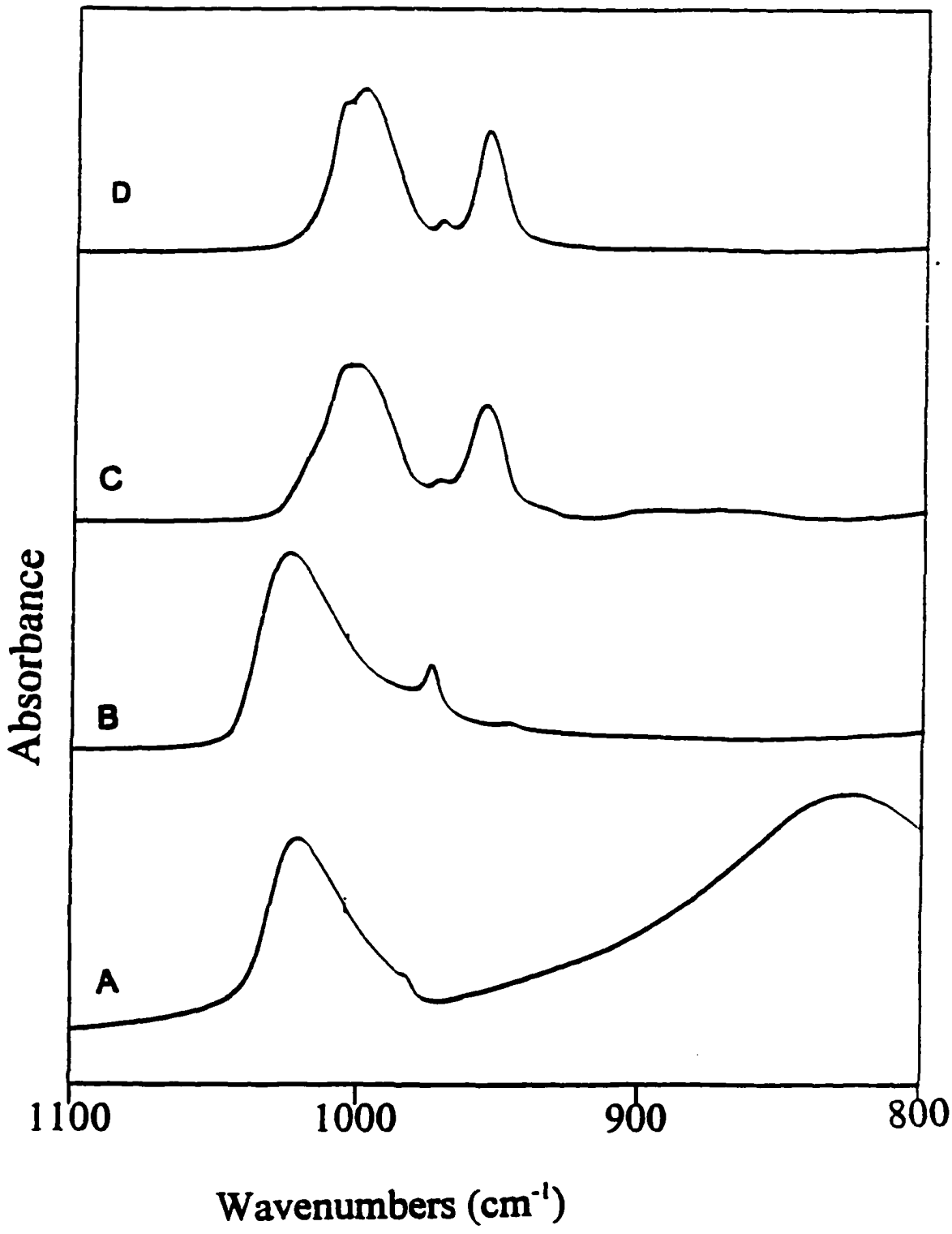

Fig. II-7 IR spectra of A) V_2O_5, B) δ-$Li_xV_2O_5$, C) ε-$Li_xV_2O_5$ and D) γ-$Li_xV_2O_5$ from 800 to 1100 cm^{-1}.

The vanadium-oxygen framework is very similar in V_2O_5 and the δ, ε and γ phases of $Li_xV_2O_5$ [5,6], as shown in Fig. II-8. Consequently, interpretation of the spectroscopic data is facilitated by viewing V_2O_5 as the parent compound of the three lithiated phases

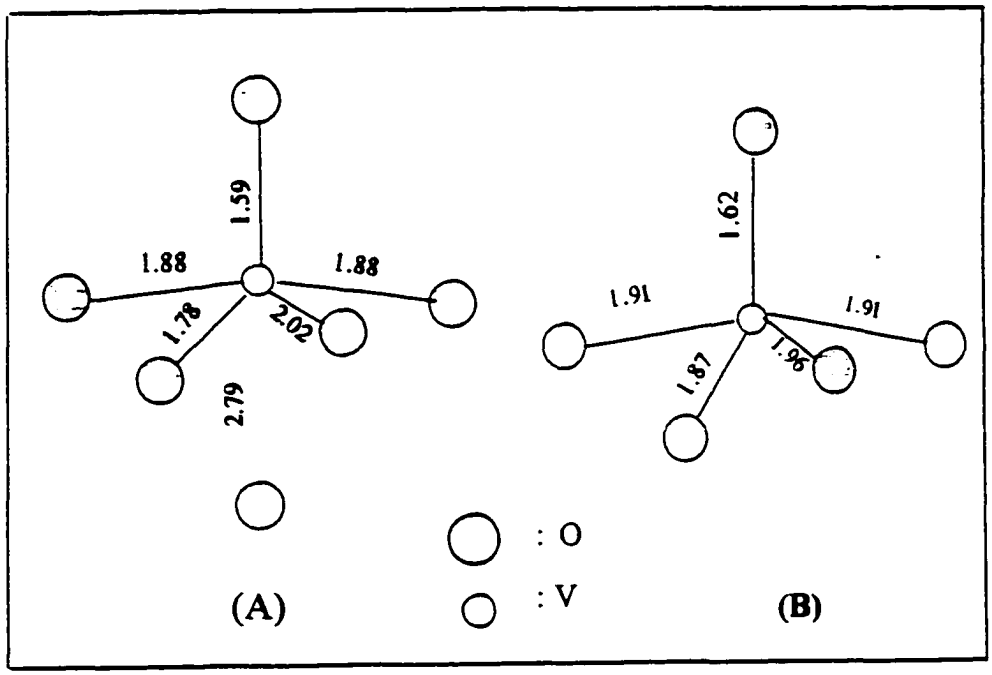

Fig. II-8 Pyramid structural units of (A) V_2O_5 and (B) δ-$Li_xV_2O_5$

and utilizing the vibrational assignments of V_2O_5 which were reported by Lucazeau et al [13] in an important study of this material. These assignments are based on both experimental measurements and theoretical calculations; several of the these assignments are repeated in Tables II-4 and 5. The vibrational bands of V_2O_5 can be described in terms of vanadium-oxygen stretching modes, vanadium-oxygen-vanadium bending vibrations and translational modes.

Table II-4 Infrared frequencies (cm^{-1}) of V_2O_5 and the δ, ε, and γ phases of $Li_{0.95}V_2O_5$

Vibrational modes and assignments of V_2O_5 [12]	V_2O_5 (this work)	δ-$Li_{0.95}V_2O_5$	ε-$Li_{0.95}V_2O_5$	γ-$Li_{0.95}V_2O_5$
1020 (B_{2u})	1021s	1024s	1019sh	
			1007sh	1006sh
			1000s	1000s
985 (B_{3u})[a]	982sh	974m	972w	972w
		946sh	955s	955s
820 (B_{3u})	825s			
	673w		730sh	734sh
600 (B_{2u})	602s	619s	624s	630s
				596s
510 (B_{3u})	517sh	554s	565s	564s
		493sh		
475 (B_{2u})	473s			
	465sh	463w	447w	447w
378 (B_{3u})	382m	397w	408w	410w

a: calculated frequency [13].
s = strong
sh = shoulder
m = medium
w = weak

Table II-5. Raman Frequencies (cm^{-1}) of Various Phases

Vibrational modes	V_2O_5 [12]	δ-$Li_{0.95}V_2O_5$	ε–$Li_{0.95}V_2O_5$	γ–$Li_{0.95}V_2O_5$
A_g	994s	984s	984s	984s
B_{1g}	976		972sh	972m
		960s	960s	960s
		942m	942s	942s
B_{1g}	848[a]		876s	876s
B_{2g}, B_{3g}	701s	730s	730s	730s
		643m	646w	652w
A_g	527s	522m	539w	543w
B_{1g}	502w			
A_g	480s	419w		434s
A_g	404s	380w	380w	380w
B_{1g}	350w	331m	331m	331m
B_{1g}	310w			296s
A_g	304sh	274s	276s	276s
B_{3g}	280s	222w	222w	222m
B_{1g}	200w			
A_g	198w	171s	171s	171s
B_{2g}, B_{3g}	145s			154s

a: calculated frequency [13]
s = strong
sh = shoulder
m = medium
w = weak

The δ-$Li_xV_2O_5$ compound belongs to space group C_{mcm} (D_{2h}^{17}) and closely resembles V_2O_5 (space group P_{mnm}, D_{2h}^{13}), except that there is a shifting of atomic positions by 1/2 c for alternate layers. The strong band at 1021 cm^{-1} in the IR spectrum of V_2O_5 is attributed to the B_{2u} symmetric stretching vibration of the $V{=}O_3$ double bond. Therefore the band at 1024 cm^{-1} in the δ compound and the very weak shoulder at 1019 cm^{-1} in the ε compound can also be assigned to the symmetric stretching of the $V{=}O_3$ bond. The corresponding region in the γ phase contains two bands at 1006 and 1000 cm^{-1}. According to Cocciantelli *et al* [14], the structural change from the δ phase to the γ phase is related to the consecutive rearrangement of the V_2O_5 pyramids along the corner-sharing oxygen atoms (O_1), see Figure II-2.

The rather poorly defined bands of the ε phase in this region were curve-fit using a commercial program (GRAMS/386) from Galactic Industries Corporation. A straight base line and one mixed Gaussian-Lorenzian function were used to fit each band in this region with a non-linear least squares method. This procedure yielded bands at 1019 (previously noted as a very weak shoulder), 1007, 1000, 972 and 955 cm^{-1}. These latter four peaks have very similar frequencies as bands observed in the γ phase which belongs to space group P_{na21} (C_{2v}^{9}) and has a lower local symmetry than the δ phase. Although there is no definitive structural data available for the ε phase, it appears to have a local structure similar to that of the γ phase.

The 985 cm^{-1} band was not observed in V_2O_5 by Lucazeau et al, but was assigned to the B_{3u} asymmetric stretching vibration of the V=O double bond based on calculations. However this mode was seen as a weak shoulder in V_2O_5 in this study, with a corresponding weak feature between 974 and 972 cm^{-1} in the lithiated phases. The most significant change in this region is the disappearance of the 820 cm^{-1} V_2O_5 band in the lithiated phases. The vanadium-oxygen framework in the δ phase is similar to that in the V_2O_5 structure except that the insertion of lithium ions shifts the V_2O_5 pyramids by 1/2 c unit; consequently the longest V-O bond (2.79 Å) in the V_2O_5 structure no longer exists in the δ phase. Primet *et al* [15] also reported that the disappearance of the 820 cm^{-1} band was related to the partial reduction of vanadium atoms in the V=O bond. In other words the insertion of lithium ions reduces the interaction between vanadium and oxygen atoms (O_1 and O_3) (see Fig. II-2).

Raman spectra of the δ, ε and γ phases for the high frequency region are shown in Figure II-9. The spectra of the three lithium vanadium oxide phases are quite distinctive in this region. The δ phase has three medium intensity bands at 984, 960 and 942 cm^{-1}. The ε and γ phases each have a strong band at 876 cm^{-1} which is absent in the δ phase. The scattering intensity of the 942 cm^{-1} band in the ε and γ phases is markedly increased compared to this band in the δ phase. The 942 cm^{-1} feature also splits into two bands in the ε phase. There is a weak shoulder at 972 cm^{-1} in the ε phase which becomes a distinct peak in the γ phase. The ε and γ phases appear to be similar in this region although several distinctive differences are noted.

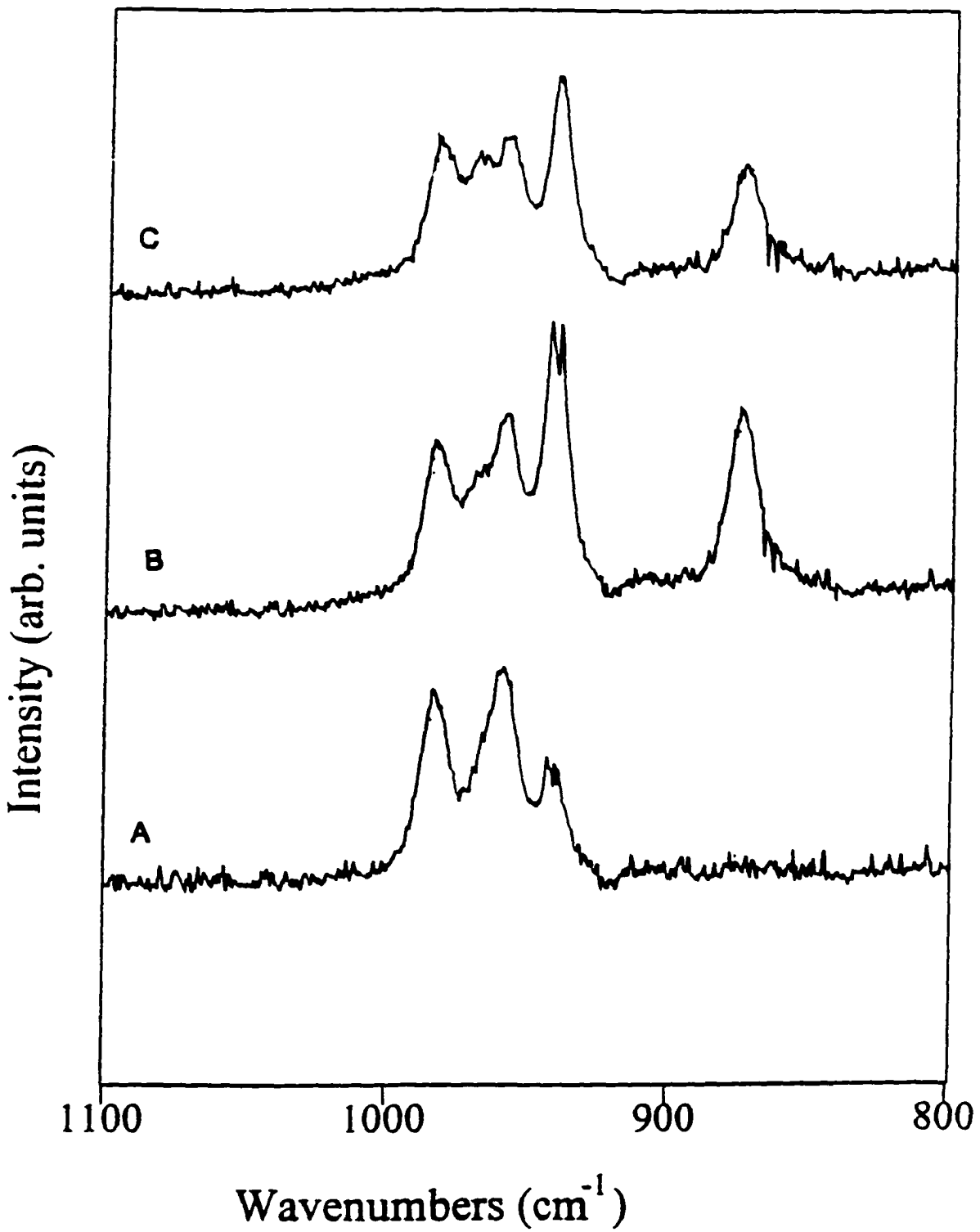

Fig. II-9 Raman spectra of A) δ-$Li_xV_2O_5$, B) ε-$Li_xV_2O_5$ and C) γ-$Li_xV_2O_5$ from 800 to 1100 cm^{-1}.

The Raman spectra provide additional insight into the nature of the structural changes from the δ phase through the γ phase. The Raman spectra of the three phases are more complex than that of V_2O_5 in the high frequency region. As shown in Table II-5, there is only one strong peak in the Raman spectrum of V_2O_5 in this region. The insertion of lithium atoms may break down some of the coupling between pyramid chains and increase occupancy of the unit cell in the δ phase. As a result, more vibrational modes become active in the Raman spectra. Abello *et al.* assigned the 994 cm^{-1} band in V_2O_5 to the A_g symmetric vibrations of the $V=O_3$ double bond. Due to the close crystallographic relationship between the δ phase and V_2O_5 (D_{2h}^{17} vs D_{2h}^{13}), the 984 cm^{-1} band in the δ phase can be assigned to the A_g symmetric stretching of the double bond. A similar assignment can be made for the 984 cm^{-1} bands in the ε and γ phases. The decrease of vibrational frequency of this band from V_2O_5 to the intercalated phases indicates that insertion of lithium ions has weakened the double bond. As can be seen in Figure II-2, the corner-sharing oxygen atoms (O_1) and the double bond oxygen atoms (O_3) undergo the greatest position shift during the transition process. Therefore the two bands at 972 and 942 cm^{-1} likely contain contributions from the motion of these two types of oxygen atoms since they show relatively large changes upon lithium substitution. Comparing the Raman spectrum of V_2O_5 with that of the ε and γ phases, the new bands at 876 cm^{-1} in the ε and γ phases may be analogous to the $V\text{-}O_1\text{-}V$ B_{1g} bending mode in the V_2O_5 structure which occurs at 848 cm^{-1}. The 960 cm^{-1} bands in the three lithiated phases may originate in the 976 cm^{-1} band in V_2O_5, which is also attributed to the vanadium-oxygen stretching vibrations.

There were some striking changes in the IR spectra from V_2O_5 through the γ phase in the intermediate frequency region (800-400 cm^{-1}, Fig. II-10). The insertion of lithium ions into the layers causes rearrangements of the V-O polyhedra which are reflected in the vibrational spectrum. Thus the spectrum of V_2O_5 has a very different profile from spectra of the three lithium intercalation phases and it is difficult to relate many bands in the latter spectra to bands in the parent V_2O_5 compound . At present time, no successful efforts have been made to assign the spectral changes. A single exception is the strong band at 602 cm^{-1} in V_2O_5 which is probably related to the strong bands at 619 cm^{-1} in the δ phase, 624 cm^{-1} in the ε phase and 630 cm^{-1} in the γ phase. The strong band at 554 cm^{-1} in the δ phase may originate in the weak shoulder at 517 cm^{-1} or even the strong peak at 473 cm^{-1} in V_2O_5. The IR spectra of the δ, ε and γ phases appear to be similar, except that the 619 cm^{-1} band in the δ phase shifts to 624 and 630 cm^{-1} in the ε and γ phases, respectively. Meanwhile a strong band appears at 596 cm^{-1} in the γ phase and exists only as a shoulder in the ε and δ phases. The 554 cm^{-1} band in the δ phase shifts to 565 and 564 cm^{-1} in the ε and γ phases, respectively. The weak band at 463 cm^{-1} in the δ phase shifts to 447 cm^{-1} in the ε and γ phases with a corresponding decrease in intensity. The weakly observed shoulder at 397 cm^{-1} in the δ phase becomes an obvious band in the ε and γ phases, centered at 408 and 410 cm^{-1}, respectively. These frequency data are summarized in Table II-5.

The IR spectra of the three lithiated phases in this spectral region also illustrate that the ε phase is structurally closer to the γ phase than to the δ phase. The IR spectra of the ε and

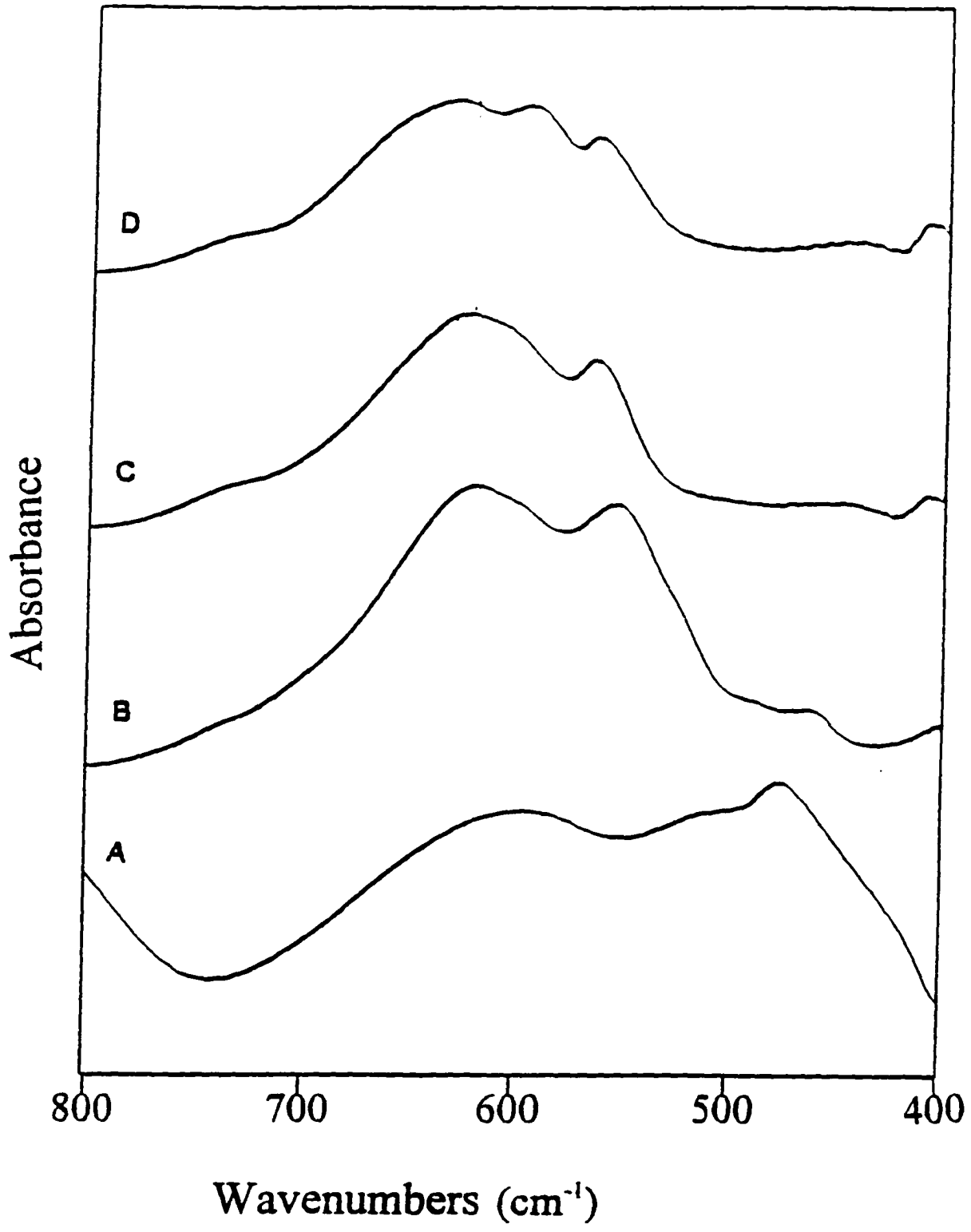

Fig. II-10 IR spectra of A) V_2O_5, B) δ-$Li_xV_2O_5$, C) ε-$Li_xV_2O_5$ and D) γ-$Li_xV_2O_5$ from 400 to 800 cm^{-1}.

the γ phases appear to be similar, except that the 624 cm^{-1} band in the ε phase splits into two peaks, 630 and 596 cm^{-1}, in the γ phase. The shifting of the 554 cm^{-1} band in the δ phase to higher frequency in the ε and γ phases originates in the rearrangement of the pyramids from the δ to ε phase. However the exact assignments of bands in this region are not clear at this time. These modes may be related to the V-O-V bending vibrations and the lithium-oxygen vibrations. Far IR measurements and isotope substitution experiments will be extremely helpful to complete the band assignments. Porotnikov [10] reported the IR spectra of α, β and γ-$Li_xV_2O_5$ in the range of 33 to 4000 cm^{-1} and the vibrational mode analysis. Although the irreducible representations of the modes in the β phase are listed, no space group is given.

The Raman spectra of the three lithiated phases are similar in the intermediate frequency region (800-400 cm^{-1}, Fig. II-11). The strong peak at 730 cm^{-1} remains unchanged throughout the three phases. According to Abello *et al.* [13], a strong band at 700 cm^{-1} in V_2O_5 is attributed to either the B_{2g} asymmetric stretching or the B_{3g} symmetric stretching motion involving the edge-sharing oxygen atoms (O_2). The 730 cm^{-1} band in the spectra of the $Li_{0.95}V_2O_5$ compounds are likely related to the 700 cm^{-1} band of V_2O_5. As shown in Fig. II-2, the structural change from the δ phase to the γ phase involves the rotation of the V_2O_5 pyramids along the corner-sharing oxygen atoms (O_1) with the consequence that the edge-sharing oxygen atoms (O_2) undergo the least shift in position. Therefore it is not surprising that the 730 cm^{-1} band appears quite similar in the δ, ε and γ phases. The band at 643 cm^{-1} in the δ phase shifts to 646 cm^{-1} in the ε phase and 652 cm^{-1}

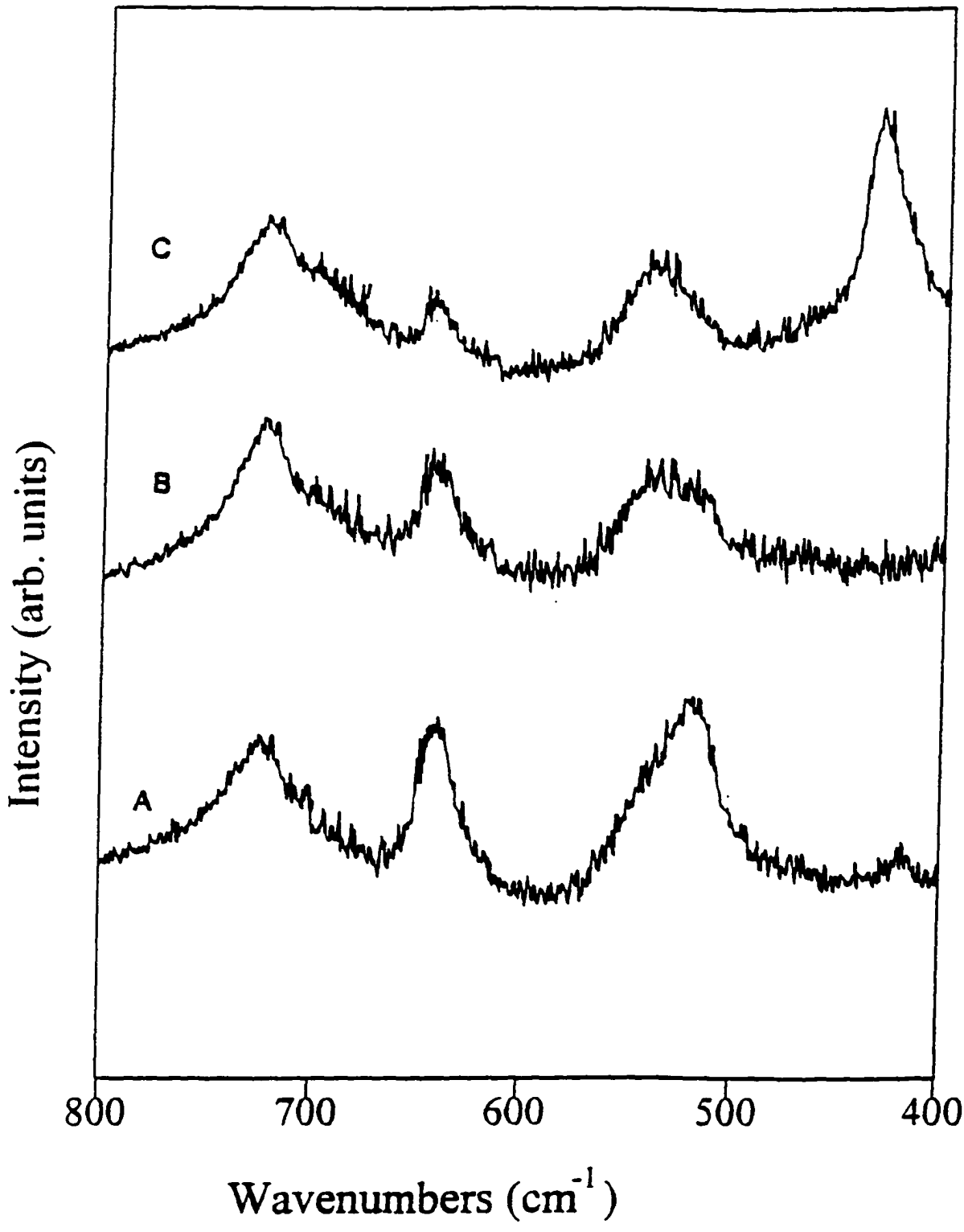

Fig. II-11 Raman spectra of A) δ-$Li_xV_2O_5$, B) ε-$Li_xV_2O_5$ and C) γ-$Li_xV_2O_5$ from 400 to 800 cm^{-1}.

in the γ phase. The latter feature was not observed in the Raman spectra of V_2O_5 and may originate in the insertion of lithium ions. The peak centered at 522 cm^{-1} in the δ-phase is very asymmetric, with a high frequency wing. This high frequency feature becomes a band at 539 cm^{-1} in the ε-phase and at 543 cm^{-1} in the γ-phase. The 527 cm^{-1} band in V_2O_5 was assigned by Lucazeau to the bending vibration of the $V\text{-}O_1\text{-}V$ bond (normal mode A_g). The 522 cm^{-1} band in the δ phase may be attributed to a similar bending mode. This mode is very sensitive to the phase transition process. There is also a very weak band at 419 cm^{-1} in the δ phase and a strong peak at 434 cm^{-1} in the γ phase.

The most striking differences in the Raman spectra of the three phases appear in the low frequency region (400-100 cm^{-1}, Fig. II-12). The peaks at 380 and 331 cm^{-1} remain relatively unchanged in the three phases. These two bands may correspond to the A_g mode (404 cm^{-1}) and the B_{1g} mode (350 cm^{-1}), respectively, in the Raman spectrum of V_2O_5. The intensity of the band at 222 cm^{-1} seems to increase from the δ through the ε into the γ-phase. The γ phase has a much different profile than the δ and ε phases in this region, with two additional strong peaks at 296 and 150 cm^{-1}, which do not appear in the ε or δ phases. The bands at 274 and 171 cm^{-1} in the δ phase also remain relatively unchanged throughout the three phases. A reasonable guess is that these two bands originate in the vibrations related to the edge-sharing oxygen atoms. According to Lucazeau, the 198 cm^{-1} band in V_2O_5 is due to the wagging vibration of the $O_1\text{-}V\text{-}O_3$ unit. Consequently, the bands at 171 cm^{-1} in the three lithium intercalation phases may also contain a significant contribution from this wagging motion. The additional bands at 296 cm^{-1}

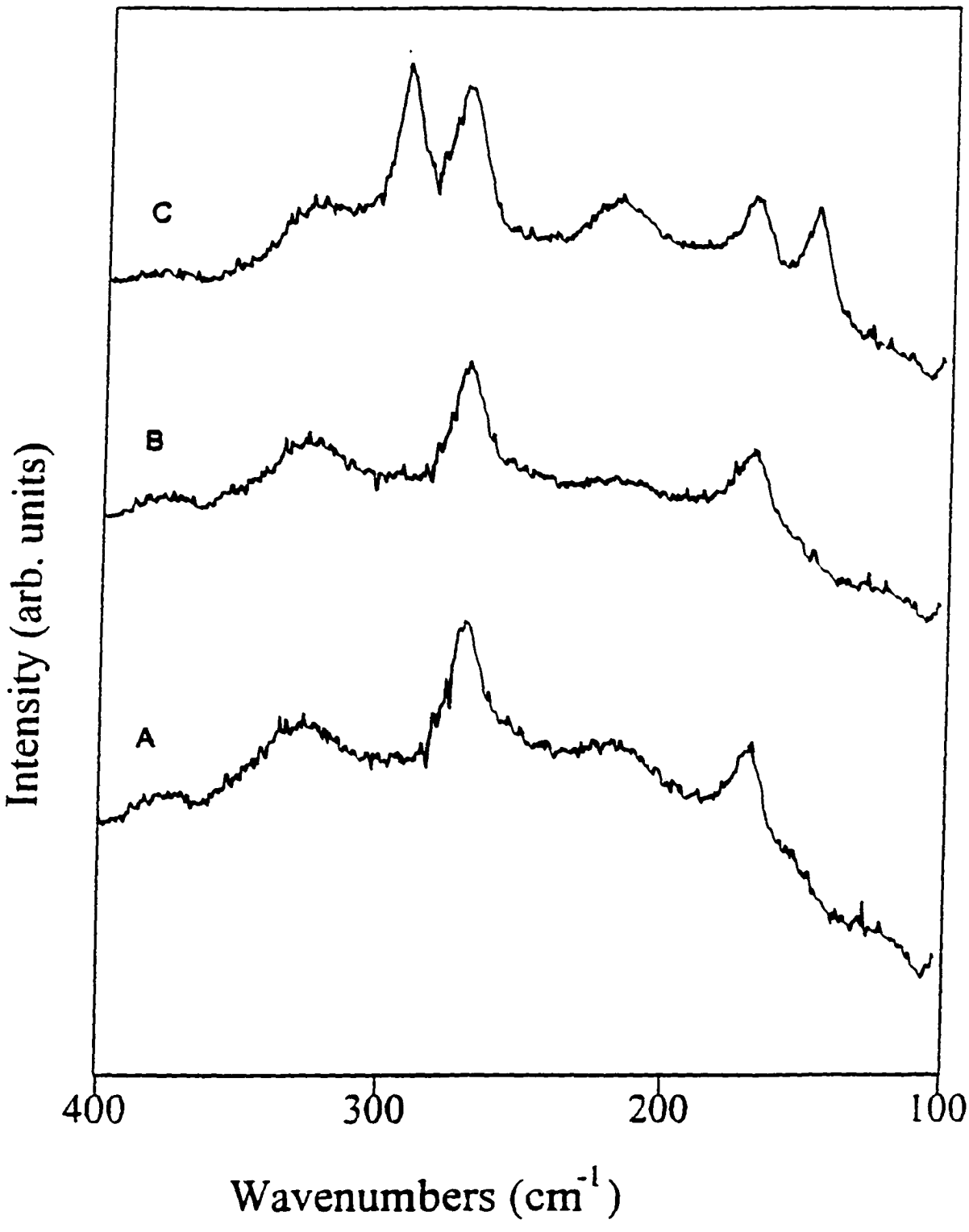

Fig. II-12 Raman spectra of A) δ-$Li_xV_2O_5$, B) ε-$Li_xV_2O_5$ and C) γ-$Li_xV_2O_5$ from 100 to 400 cm^{-1}

and 150 cm^{-1} in the γ phase may be due to the higher occupancy of the unit cell in the γ phase. Further studies utilizing isotopic substitution will be very helpful to identify constituent atomic motion in the low frequency region.

2.4 Summary

For the first time, the Raman spectra of lithium vanadium oxides are reported in the spectral range 50 to 1100 cm^{-1}. The δ, ε, and γ phases of $Li_{0.95}V_2O_5$ can be clearly identified from their IR and Raman spectra. The inserted lithium atoms mainly interact with the corner-sharing oxygen atoms (O_1) and the double-bonded oxygen atoms ($V{=}O_3$). Therefore the vibrational modes originating in the motion of these atoms are very sensitive to structural differences in the three lithiated phases. Although the δ and ε phases show similar X-ray diffraction patterns, the vibrational spectra reveal that these two phases possess considerably different local symmetries. The frequency changes of the A_{1g} modes at 643 and 522 cm^{-1} in the δ phase are indicative of different arrangements of the pyramids in the three phases. The structural modifications of cathode materials after cycling is a major concern for the development of rechargeable lithium batteries. At the present time X-ray diffraction is the primary technique to detect the structural changes. But insertion of lithium atoms into a host material usually causes only minor structural modification, which can be very difficult to detect by X-ray diffraction methods. Neutron diffraction is as important in structure determination of alkali metal intercalated materials. However, the vibrational spectra are often extraordinarily

sensitive to subtle structural changes. Therefore vibrational spectroscopic measurements provide another experimental dimension for structural study of cathode materials. Further studies such as far IR (400 cm^{-1} and below) and isotope substitution are necessary for more complete vibrational assignments of the lithium-inserted vanadium oxide phases described in this study. Results from this work establish that Raman spectroscopy is a very useful tool in investigating the phase transitions among the low temperature lithium vanadium oxides. The results also suggest that Raman spectroscopy may be a useful tool for the *in situ* study of intercalation and deintercalation processes of these kinds of cathode materials during battery cycling processes.

References:

1) West, K. Zachau-Christiansen, B., Jacobsen, T. andSkaarup, S. *Solid State Ionics* **76**.15 (1995).

2) Cocciantelli, J. M., Menetrier, M., Delmas, C. Doumerc, J. P., Pouchard, M. and Hagenmuller, M. *Solid State Ionics* **50** 99 (1992).

3) Cartier, C., Chanchant, A., Vaedaguer, M., Messina, R. and Dexpert, H. *Electrochimica Acta* **35** 889 (1990).

4) Murphy, D. W., Christian, P. A., Disalvo, F. J., and Waszczak, J. V., *Inorganic Chemistry* **18** 2800 (1979).

5) Cava, R. J., Santoro, A., Murphy, D. W., Zahurak, S. M., Fleming, R. M., Marsh, F. and Roth, R. S., *Journal of Solid State Chemistry* **65** 63 (1986).

6) Galy, P. J., and Hardy, A., *Acta Cryst.* **19** (1965), 432; Bystrom, A., Wilhelmi, K. and Brotzen, O., *Acta Chemica Scan.* **4** 1119 (1950).

7) Steger, W. E., *Progress in Molecular Spectroscopy*, Teubner-Texte zur Phisik, Band **20**, edited by Salzer, R., Kriegsmann, H and Werner, G. 165 (1988).

8) Pigorsch, E. andSteger, W. E., *Phys. Stat. Sol. (A)* **117** K189 (1990).

9) Cazzanelli, C., Mariotto, G., Passerini, S. and Decker, F., *Solid State Ionics* **70/71** 412 (1994).

10) Porotnikov, N. V., *Russian Journal of Inorganic Chemistry* **39** 1470 (1994).

11) Huang, W. and Frech, R., *Solid State Ionics*, **86-88**, 395 (1996).

12) Fateley, W. G., Dollish, F. R., McDevitt, N. T. an Bentley, F. F., "Infrared and

Raman Selection Rules for Molecular and Lattice Vibrations: The Correlation Method", John Wiley & Sons, Inc., New York, (1972)

13) Abello, L., Husson, E., Repelin, Y. and Lucazeau, G., *Spectrochimca Acta*, **39A** 641 (1983).

14) Cocciantelli, J. M., Menetrier, M., Delmas, C., Doumerc, J. P., Pouchard, M., Brousely, M. and Labat, J. *Solid State Ionics* **78** 143 (1995).

15) Primet, M., Fouilloux, P. and Imelik, B. *Surface Science*, **85** 457 (1979).

Chapter III Spectroscopic Investigation of $Li_{1+x}V_3O_8$

3.1 Background

Lithium trivanadate, $Li_{1+x}V_3O_8$, has been investigated as an intercalation cathode for rechargeable lithium batteries for the past twenty years. Since Besenhard and Schöllhorn first reported the intercalation reactions within this material in 1979 [1], intensive research has been focused on its structural characterization and electrochemical performance [2-7]. The crystal structure of $Li_{1+x}V_3O_8$ was first reported by Wadsley [8] using powder X-ray diffraction method and recently confirmed by Picciotto *et al.* [9] using single crystal diffraction refinements. Lithium ions can chemically or electrochemically intercalate/deintercalate within the tunnels of the $Li_{1+x}V_3O_8$ host according to the following reaction:

$$x\,Li^+ + x\,e^- + LiV_3O_8 \rightarrow Li_{1+x}V_3O_8$$

Each $Li_{1+x}V_3O_8$ structural unit can accommodate up to three moles of lithium ions to form a highly lithiated phase, $Li_4V_3O_8$. Therefore a lithium rechargeable battery based on the $Li_{1+x}V_3O_8$ cathode and the lithium anode can provide a theoretical capacity up to 690 mAh/g, with an operating voltage between 2.0 to 3.5 V [10].

The $Li_{1.1}V_3O_8$ has a monoclinic structure with the space group $P2_1/m$. There are two different V-O structural units, VO_6 octahedra and VO_5 distorted trigonal bipyramids. The VO_6 octahedra form a zigzag double ribbon extending along the (010) direction and the VO_5 bipyramids form another zigzag ribbon parallel to the VO_6 double ribbons. The two ribbons are connected through apical oxygen atoms to form a V-O layer. The V-O layers are held together through the interactions of the lithium ions. There are two different sites for lithium ions, octahedral and tetrahedral. At low concentration ($x < 1$), lithium ions occupy the octahedral sites, Li(1). If x value exceeds one, lithium ions can take up the tetrahedral sites, Li(2). Fig. III-1 schematically shows the V-O ribbon arrangements and the lithium ion locations.

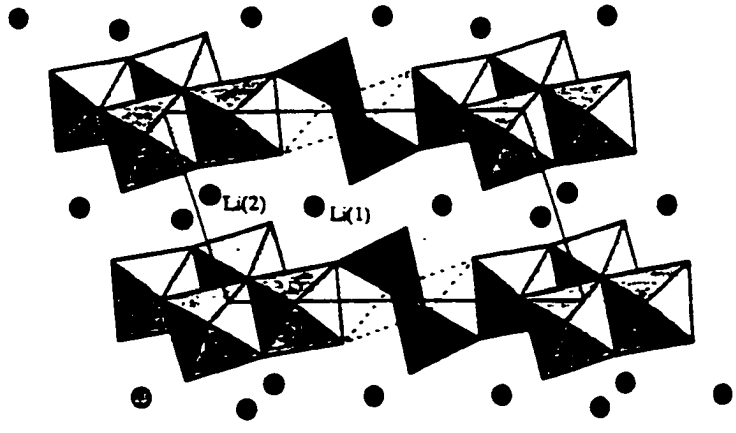

Fig III-1 Schematical representation of the VO_6 and VO_5 ribbons, Li(1) and Li(2) locate at octahedral and tetrahedral sites, respectively [9].

Continuous structural changes were observed during the lithium intercalation process. The unit cell parameter **a** decreases and parameters **b** and **c** expand when x increases from 0 to 3. However, no obvious phase transitions were identified from the X-ray diffraction data. Picciotto *et al.* [9] concluded the insertion of lithium ions into $Li_{1.1}V_3O_8$ host caused only a layer expansion and a slight structural rearrangements of the VO_6 and VO_5 polyhedra. In addition to X-ray structural analysis, techniques such as electron paramagnetic resonance (EPR), extended x-ray absorption fine structure (EXAFS), ^7Li nuclear magnetic resonance (NMR) and Fourier transform infrared spectroscopy (FTIR) [11, 12] have been used to study the local structural modifications accompanying the intercalation reaction. Raman spectroscopy is very sensitive to local structural changes and has been recently used to provide structural information about intercalation compounds and cathode materials [13-15]. This part of the dissertation presents the IR and Raman spectra of $Li_{1.1}V_3O_8$ and $Li_4V_3O_8$. The factor group analysis method is used to interpret the spectral changes. These spectroscopic results will provide insight into the structural modifications occurring during the intercalation/deintercalation processes.

3.2 Experimental

3.2.1 Preparation of single crystals

Single crystals of $Li_{1.1}V_3O_8$ and $^6Li_{1.1}V_3O_8$ were prepared using solid state synthesis methods [8, 9]. The $Li_{1.1}V_3O_8$ crystal was prepared by heating a 1:2 molar mixture of Li_2CO_3 and V_2O_5 at 680 °C in a tube furnace for four hours, keeping the temperature at 650 °C for five days, and then letting the furnace cool down to room temperature in the air. The $^6Li_{1.1}V_3O_8$ crystal was prepared starting from $^6LiOH{\cdot}H_2O$ and V_2O_5 under similar reaction conditions as for the $Li_{1.1}V_3O_8$. The $^6LiOH{\cdot}H_2O$ was obtained from Oak Ridge National Laboratory at 95% ^6Li enrichment. The lithiated product, $Li_4V_3O_8$, was prepared using a chemical intercalation method. The $Li_{1.1}V_3O_8$ single crystal was treated with a 0.46 M solution of n-butyllithium in hexane at 20 °C for seven days [9]. The amount of lithium ions in the lithiated phase was determined by atomic absorption spectroscopy.

3.2.2 X-ray diffraction measurements

X-ray powder diffraction was used to verify the formation of the $Li_{1.1}V_3O_8$. The experimental procedures were described in Section 2.2.2. The single crystal diffraction data were collected at -40 °C on a Siemens 94 diffractometer using monochromated Mo K_α radiation (λ=0.71073 Å) and data were corrected for Lorenz and polarization effects.

Structures were refined with the computer program SHELXL-93 using the least square method.

3.2.3 Infrared spectroscopy

IR spectra were recorded using a Bruker IFS66V infrared system in the range 400 to 4000 cm^{-1} with a resolution ± 1 cm^{-1}. The $Li_{1.1}V_3O_8$ and $^6Li_{1.1}V_3O_8$ crystals were ground into fine powders to make KBr pellets. The experimental details are described in Section 2.2.4.

3.2.4 Raman spectroscopy

Raman spectra were collected as described in Section 2.2.5 at ± 1 cm^{-1} resolution with a Jobin-Yvon T64000 Raman System. The 514.5 nm argon excitation line was used as the laser source. A holographic notch filter (Kaiser Optics) centered at 514.5 nm was used with the Raman system in the single monochromator mode. A thermoelectrically cooled CCD detector measured the scattering intensity. All Raman spectra were collected in a backscattering geometry through an 80x microscope which reduced the laser beam to a 2μm diameter spot. The laser power was kept below 10 mW to avoid thermal damage to the samples. A Kaiser polarized analyzer was used to collect polarized Raman spectra. The polarization orientation of the scattering geometries was confirmed by measuring the well-known vibrational modes of a Na_2SO_4 single crystal [16].

3.3 **Results and discussion**

3.3.1 X-ray diffraction results

Since the crystal structure of $Li_{1.1}V_3O_8$ was solved by Wadsley [8] and Picciotto *et al.* [9], only powder X-ray diffraction was employed to identify its structure. Fig. III-2 shows the powder x-ray diffraction pattern of $Li_{1.1}V_3O_8$ and Table III-1 lists the d-spacing data of the major diffraction peaks along with that from the standard JCPDS Card 55-437.

Table III-1 d-spacing data of $Li_{1.1}V_3O_8$

d-spacing (Å)	Relative intensity (%)	d-spacing (Å) from JCPDS	Relative intensity JCPDS
6.343	100	6.360	100
5.730	8	5.727	7
3.815	16	3.818	20
3.430	4	3.425	6
3.223	25	3.221	12
3.145	48	3.146	45
2.905	28	2.904	25
2.288	6	2.286	5
2.200	15	2.200	12
2.139	20	2.136	10
1.799	9	1.800	11
1.536	5	1.534	6
1.520	8	1.520	8

Fig. III-2 Powder X-ray diffraction pattern of $Li_{1.1}V_3O_8$

The $^6Li_{1.1}V_3O_8$, has a very similar crystal structure to the $Li_{1.1}V_3O_8$. Table III-2 summarizes the crystal data and structure refinement parameters for $^6Li_{1.1}V_3O_8$. The ^6Li ions occupy both Li(1) and Li(2) sites. Fig. III-3 schematically shows the VO_6 and VO_5 polyhedral, and the $Li(1)O_6$ and $Li(2)O_4$ structural units. Table III-3 lists the bond lengths related to the polyhedra. The crystallographic axes of the single crystals which are required for polarized Raman spectral measurements can be easily determined from the single crystal x-ray diffraction analysis.

Table III-2 Crystal Data and Structure Refinement for $^6Li_{1.1}V_3O_8$

Empirical formula	$^6Li_{1.1}V_3O_8$
Wavelength	0.71073 Å
Crystal system	Monoclinic
Space group	$P2_1/m$
Unit cell dimensions	a = 6.6980(10) Å α = 90 deg. b = 3.5950(10) Å β = 104.83(3) deg. c = 11.816(2) Å γ = 90 deg.
volume	275.04(10) Å^3
Z	2.000
Density (calculated)	3.475 g/cm^3
Absorption coefficient	4.990 mm^-1
F(000)	272
Crystal size	0.8x0.25x0.1 mm
Theta range for data collection	3.15 to 27.48 deg.
Index ranges	-8<=h<=8, -4<=k<=0, -15<=l<=15
Reflections collected	1,442
Independent reflections	724 [R(int) = 0.0338]
Refinement method	Full-matrix least-squares on F^2
Data/ restraints/ parameters	719 / 0 / 80
Goodnes-of-fit on F^2	1.100
Final R indices [I>2sigma (I)]	R1 = 0.0282, wr2 = 0.0715
Final R indices (all data)	R1 = 0.0305, wr2 = 0.0789
Extinction coefficient	0.019(4)
Largest diff. peak and hole	1.006 and -0.576 e.A^-3

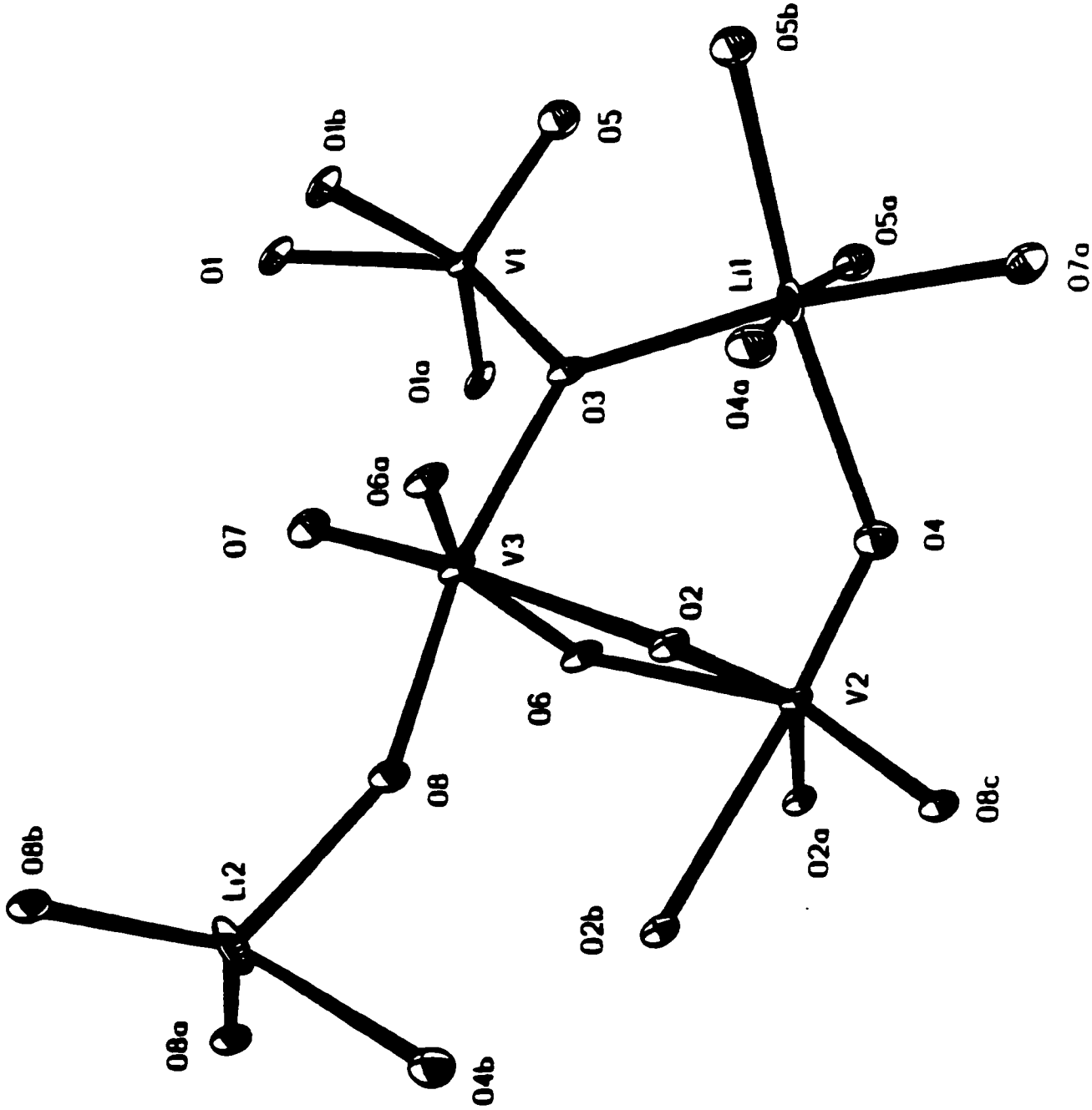

Fig. III-3 Schematic representation of V-O and Li-O polyhedra

Table III-3 Bond lengths (Å) of the V-O and Li-O structural units

$V_{(1)}O_5$		$V_{(2)}O_6$		$V_{(3)}O_6$	
Bonds	Lengths (Å)	Bonds	Lengths (Å)	Bonds	Lengths (Å)
V_1-O_5	1.614	V_2-O_4	1.613	V_3-O_7	1.611
V_1-O_3	1.730	V_2-O_6	1.732	V_3-O_6	1.867
V_1-O_1	1.990	V_2-O_2	1.883	V_3-O_{6a}	1.867
V_1-O_{1a}	1.888	V_2-O_{2a}	1.883	V_3-O_8	1.948
V_1-O_{1b}	1.888	V_2-O_{8c}	2.126	V_3-O_3	2.005
		V_2-O_{8c}	2.328	V_3-O_2	2.219
$Li_{(2)}O_4$		$Li_{(1)}O_6$			
Bonds	Lengths (Å)	Bonds	Lengths (Å)	Bonds	Lengths (Å)
$Li_{(2)}$-O_8	2.019	$Li_{(1)}$-O_7	2.079		
$Li_{(2)}$-O_{8a}	2.019	$Li_{(1)}$-O_{5a}	2.295		
$Li_{(2)}$-O_{8b}	2.192	$Li_{(1)}$-O_{5b}	2.295		
$Li_{(2)}$-O_{4b}	2.260	$Li_{(1)}$-O_4	2.342		
		$Li_{(1)}$-O_3	2.042		
		$Li_{(1)}$-O_{4a}	2.342		

3.3.2. Vibrational Spectroscopic Study

A. Symmetry-Based Normal Mode Analysis

As shown from single crystal X-ray structural analysis, $Li_{1.1}V_3O_8$ and $^6Li_{1.1}V_3O_8$ belong to the space group $P2_1/m$ (C_{2h}^5) with Z=2. Using standard factor group correlation methods [17], the irreducible representations to which the normal modes belong can be expressed as:

$$\Gamma_{optical}=24A_g + 12B_g + 11A_u + 22B_u$$

According to the spectroscopic selection rules for C_{2h}, A_g and B_g modes are Raman active, while A_u and B_u modes are IR active. Therefore 36 Raman bands and 33 IR bands are expected in the spectroscopic experiments. In this study, as in many spectroscopic studies of solids, the number of modes experimentally observed is significantly less than that predicted by group theory methods. This situation occurs because of small polarizability derivatives for many Raman active modes, small dipole moment derivatives for many infrared active modes, and small frequency shift separations of different factor group components, e.g. B_g modes almost coincident with A_g mode.

The standard designation of an experimental scattering geometry, e.g. $X(YZ)\overline{X}$, refers to laboratory fixed axes. Fig. III-4 shows a polarization experiment, $X(YZ)\overline{X}$. In a monoclinic crystal such as $Li_{1.1}V_3O_8$, it is not possible to orient the crystal so that all axes

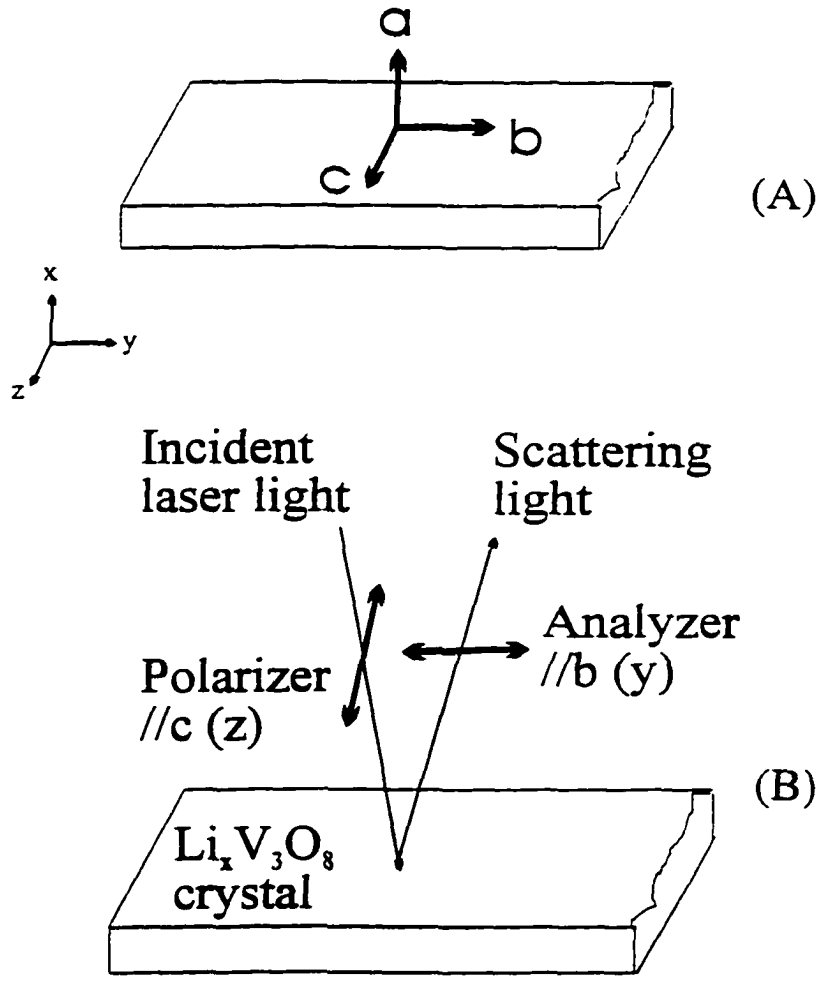

Fig. III-4 A polarization Raman experiment: (A) Crystal axes of $Li_xV_3O_8$, (B) A σ_{YZ} geometry polarized Raman experiment.

of the scattering experiment coincide with the crystallographic axes. Therefore in these measurements the scattering intensities are described in terms of the laboratory fixed axes. In the example above the $X(YZ)\overline{X}$ experimental geometry is refered as an α_{YZ} measurement, that is, a measurement which samples the YZ susceptibility derivative (with respect to the normal coordinates of interest) in laboratory fixed axes. The orientations of the crystal were chosed such that one crystallographic axis corresponds to the polarization direction of the incident (excitation) beam. In the example above the crystallographic a axis is parallel to the X direction.

In the C_{2h}^5 space group there are A_g and B_g modes which are Raman active. In the various measurements which are reported in this study, a significant level of spillover of the relatively more intense A_g modes into scattering geometries favoring B_g modes is expected. It is also possible that B_g modes can appear in scattering geometries favoring A_g modes, although this effect should be considerably weaker than the A_g into B_g spillover.

B. IR Spectra

Fig. III-5 shows the IR spectra of $Li_{1.1}V_3O_8$ and $^6Li_{1.1}V_3O_8$ in the region 400 to 1100 cm^{-1}. The two bronze phases show very similar spectra. The IR frequencies are summarized in Table III-4. No significant band shift is detected in the region around 950 cm^{-1}.

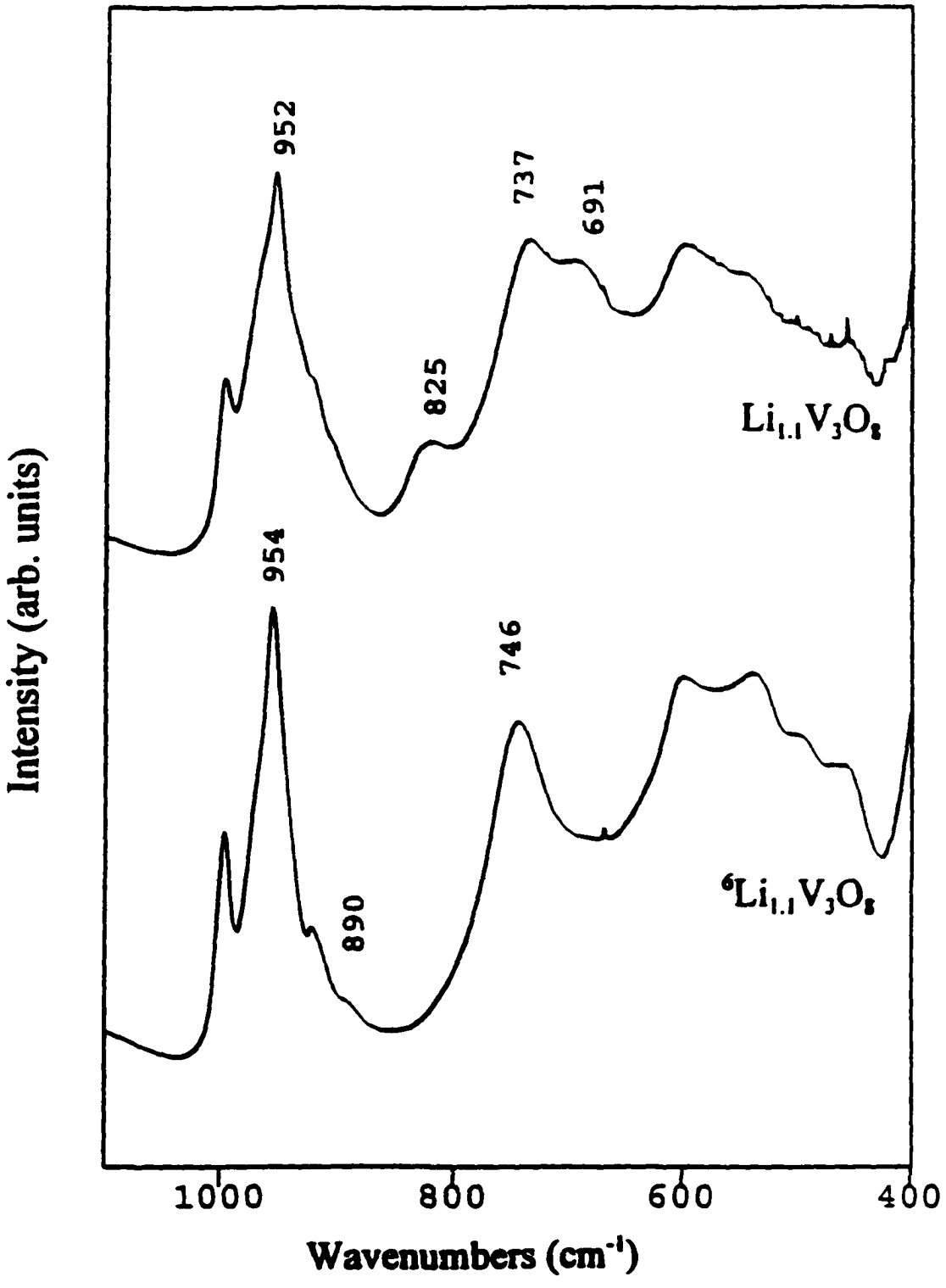

Fig. III-5 IR spectra of $Li_{1.1}V_3O_8$ and $^6Li_{1.1}V_3O_8$

However, the band at 691 cm^{-1} in $Li_{1.1}V_3O_8$ disappears while in $^6Li_{1.1}V_3O_8$ a new band appears at 746 cm^{-1}. In addition the band at 825 cm^{-1} in the $Li_{1.1}V_3O_8$ phase disappears in the ^{6}Li-substituted phase while a very weak band appears at 890 cm^{-1}. Both of these

Table III-4 IR frequencies (cm^{-1}) of $Li_{1.1}V_3O_8$ and $^6Li_{1.1}V_3O_8$

$Li_{1.1}V_3O_8$	$^6Li_{1.1}V_3O_8$
996m	996s
952vs	954vs
920sh	920m
	890sh
825m	
737s	746s
691sh	
601s	601s
538sh	538s
491sh	497sh
457m	457sh

frequency shifts are in very close agreement with those calculated from the isotopic masses, although the intensity of the 890 cm^{-1} band in $^6Li_{1.1}V_3O_8$ is significantly reduced compared to the intensity of the band at 825 cm^{-1} in the naturally abundant crystal. The IR measurements were repeated on several different samples and the 825 cm^{-1} band, although always weak, appeared in each measurement of the $Li_{1.1}V_3O_8$ phase, but was not seen in the $^6Li_{1.1}V_3O_8$ phase. This picture is complicated by the presence of the band at 737 cm^{-1} in $Li_{1.1}V_3O_8$. This feature is not seen in $^6Li_{1.1}V_3O_8$ although it may be only slightly shifted by isotopic substitution and lies under the intense and somewhat broad

feature at 746 cm^{-1} in the ^{6}Li-substituted crystal. According to Lucazeau *et al.* [18], the 737 cm^{-1} in band V_2O_5 originates primarily in the motion of the corner-sharing oxygen atom O(3) between the VO_6 double ribbons and VO_5 ribbons. Consequently this band would show only a slight frequency shift on lithium isotopic substitution. to the degree that the lithium ions interact with the oxygen atom in the V-O polyhedra.

C. Raman spectra.

Polarized Raman spectra were measured on a single crystal of $Li_{1.1}V_3O_8$ with dimensions 0.8x0.25x0.1 mm. Fig. III-6 shows the Raman spectra from the $X(YY)\bar{X}$, $X(YZ)\bar{X}$, $X(ZZ)\bar{X}$ and $Z(XY)\bar{Z}$ experimental scattering geometries in the region 830 to 1100 cm^{-1}. The polarized Raman spectra of $Li_{1.1}V_3O_8$ recorded in the region 150 to 800 cm^{-1} are shown in Fig. III-7. The corresponding frequencies are summarized in Table III-5 along with the frequency data of V_2O_5. Because the single crystal is elongated along the b axis, it is very difficult to obtain satisfactory spectra in α_{XX} and α_{XZ} scattering geometries.

The VO_5 distorted bipyramids present in $Li_{1+x}V_3O_8$ also exist in the structure of V_2O_5. Although $Li_{1.1}V_3O_8$ belongs to a different space group (C_{2h}^5) than does V_2O_5 (D_{2h}^{13}), many of the internal optic mode frequencies are determined by the vanadium-oxygen covalent bonds and the basic structure of the V-O polyhedra, both of which are similar in the

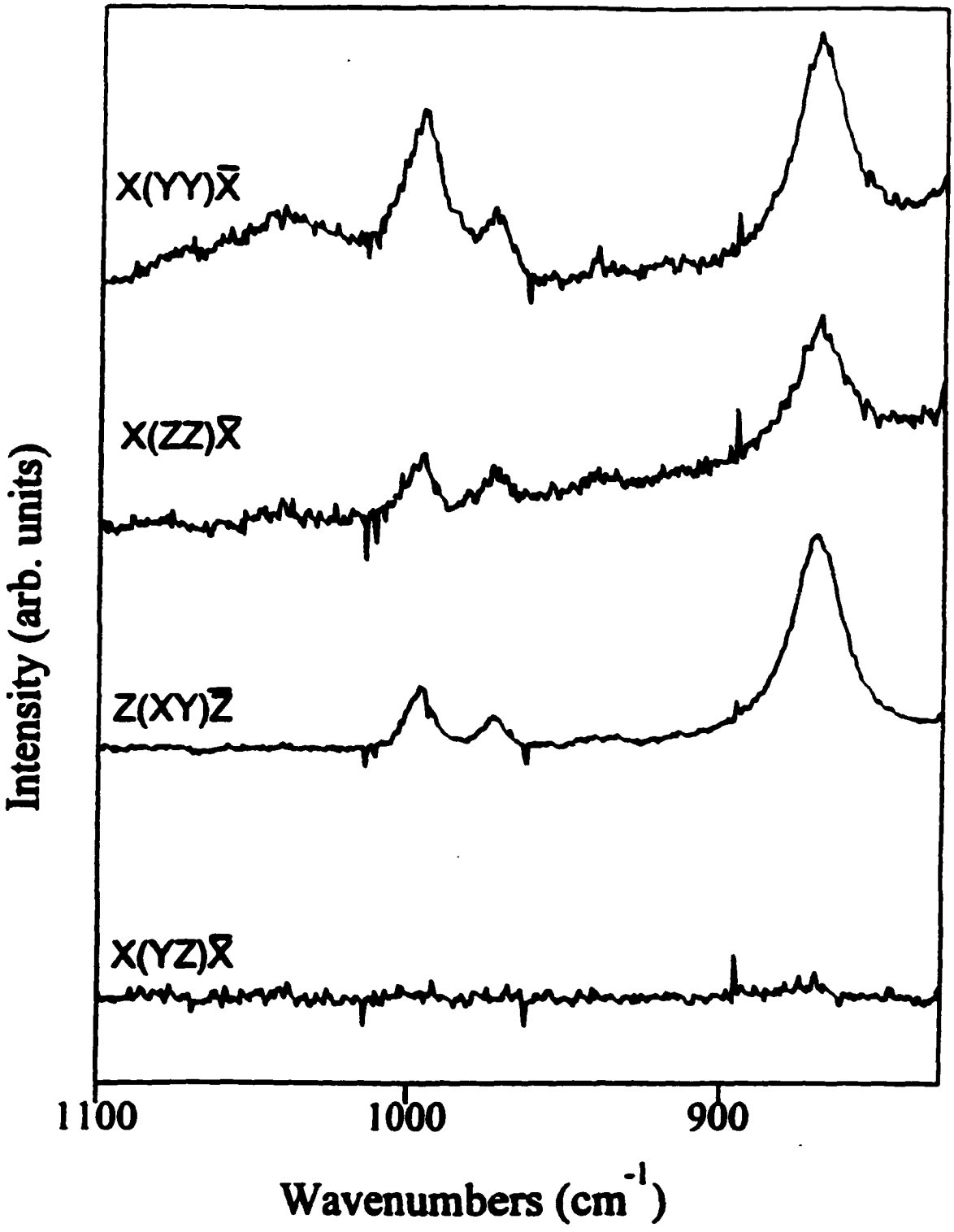

Fig. III-6 Polarized Raman spectra of $Li_{1.1}V_3O_8$ along σ_{YY}, σ_{ZZ} and σ_{YZ} geometry in the range 800 to 1100 cm^{-1}

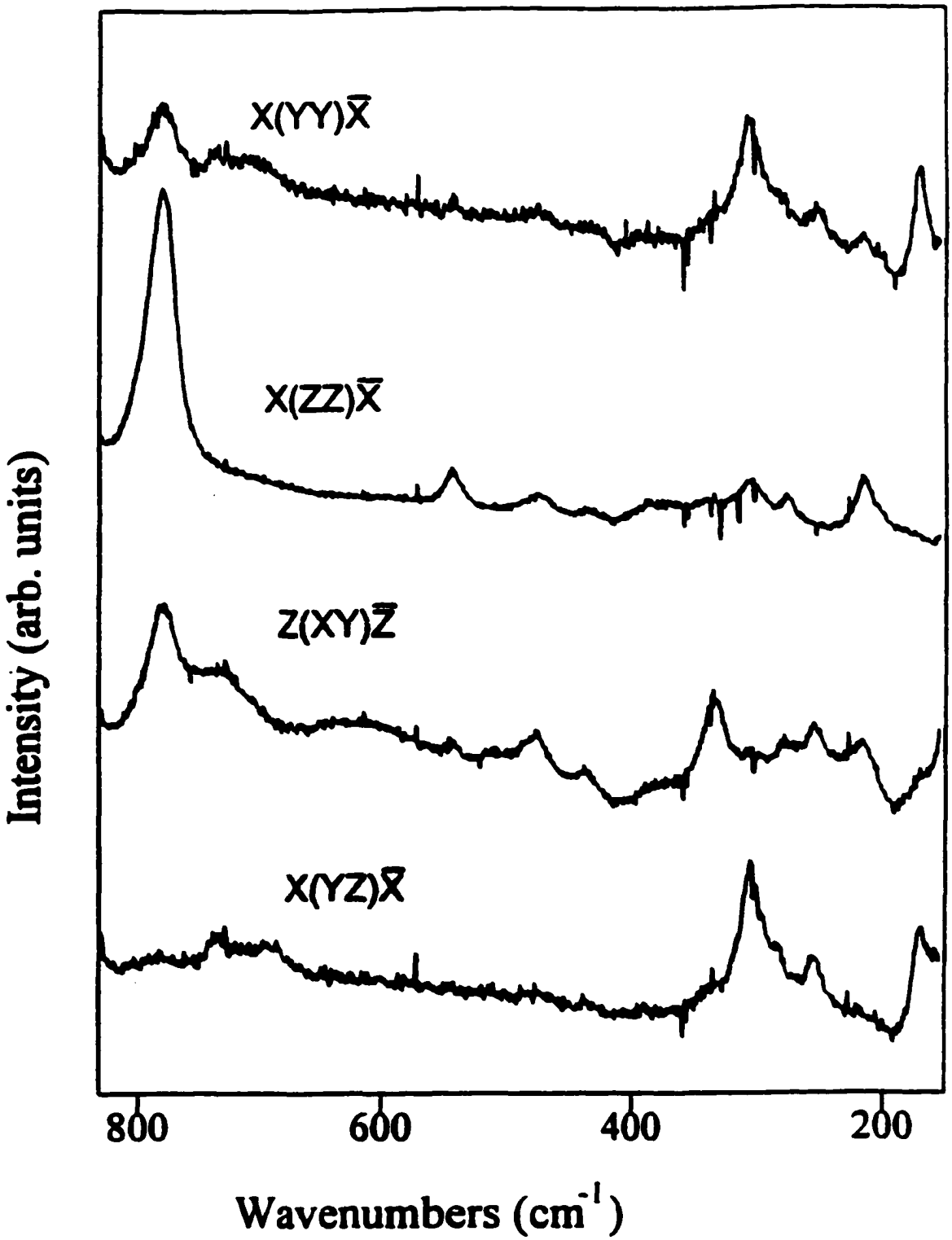

Fig. III-7 Polarized Raman spectra of $Li_{1.1}V_3O_8$ along σ_{YY}, σ_{ZZ} and σ_{YZ} geometry in the range 150 to 800 cm^{-1}

crystals. Therefore interpretation of the Raman spectra is facilitated by comparison with the spectrum of V_2O_5. Although it is difficult to unambiguously determine symmetry-based vibrational assignments from polarized Raman scattering experiments for monoclinic $Li_{1.1}V_3O_8$, several vibrational bands can be assigned with some degree of confidence. The two high frequency bands at 993 and 972 cm^{-1} can only be seen in the

Table III-5 Raman frequencies (cm^{-1}) of $Li_{1.1}V_3O_8$ and V_2O_5

Vibrational modes	V_2O_5 [18]	σ_{yy}	σ_{zz}	σ_{xy}	σ_{yz}
A_g	994s	993m	993w	993m	
B_{1g}	976	972w	972w	972w	
B_{1g}	848[a]	869s	869s	869s	869vw
B_{2g}, B_{3g}	701s	773w	773vs	773s	
		732sh		732sh	732w
A_g	527s			604w	693w
B_{1g}	502w	545w	545m	545w	
A_g	480s		478w	478m	
A_g	404s		438sh	438sh	438w
B_{1g}	350w		383w		
B_{1g}	310w		332w	332s	332w
A_g	304sh	304m	304m		304s
B_{3g}	280s		276w	278w	283sh
B_{1g}	200w	254sh		254m	254m
A_g	198w	212w	212s	212m	
B_{2g}, B_{3g}	145s	171s			168m

a: calculated frequency [18]

polarization experiments α_{YY}, α_{ZZ} and α_{XY}, suggesting that these vibrational modes belong to the A_g symmetry species. The 993 cm^{-1} band can be assigned to the V-O stretching vibrations of the VO_5 pyramids [18, 19]. The medium intensity band at 972 cm^{-1} may be correlated with the weak feature at 976 cm^{-1} in the spectrum of V_2O_5. The 869 cm^{-1} band was not found in the spectrum of V_2O_5, and may be attributed to the stretching vibrations of the VO_6 octahedra (the calculations of Lucazeau *et al.* indicated a band at 848 cm^{-1} in V_2O_5 based on the VO_6 model [16]). Although this band appears in all four scattering geometries and, in principle, may belong to either the A_g or B_g mode, the scattering intensity in α_{YZ} is very weak compared to the other three geometries. Therefore this band may be also assigned to the A_g mode. Other bands that can be assigned to the A_g symmetry species are at 773, 545, 478, 383, and 212 cm^{-1}. The bands at 693 and 283 cm^{-1} can be uniquely attributed to the B_g mode. Other bands at 732, 438, 332, 304 and 254 cm^{-1} can be assigned to either A_g or B_g modes. Further studies are necessary to completely assign these bands.

An important part of this study is to determine which bands contain significant contributions from lithium ion motion. The inserted lithium ions can occupy the second octahedral and tetrahedral sites and cause local structural modifications which may be observed spectroscopically. Figs. III-8 and III-9 show the polarized Raman spectra of the $Li_{1.1}V_3O_8$ and $^6Li_{1.1}V_3O_8$ compounds in the α_{ZZ} measurement. Fig. III-8 illustrates that the shift of the strong band at 773 cm^{-1} in $Li_{1.1}V_3O_8$ to 779 cm^{-1} in $^6Li_{1.1}V_3O_8$. The band at 212 cm^{-1} in $Li_{1.1}V_3O_8$ shifts to 216 cm^{-1}, as shown in Fig. III-9. The Raman spectrum of

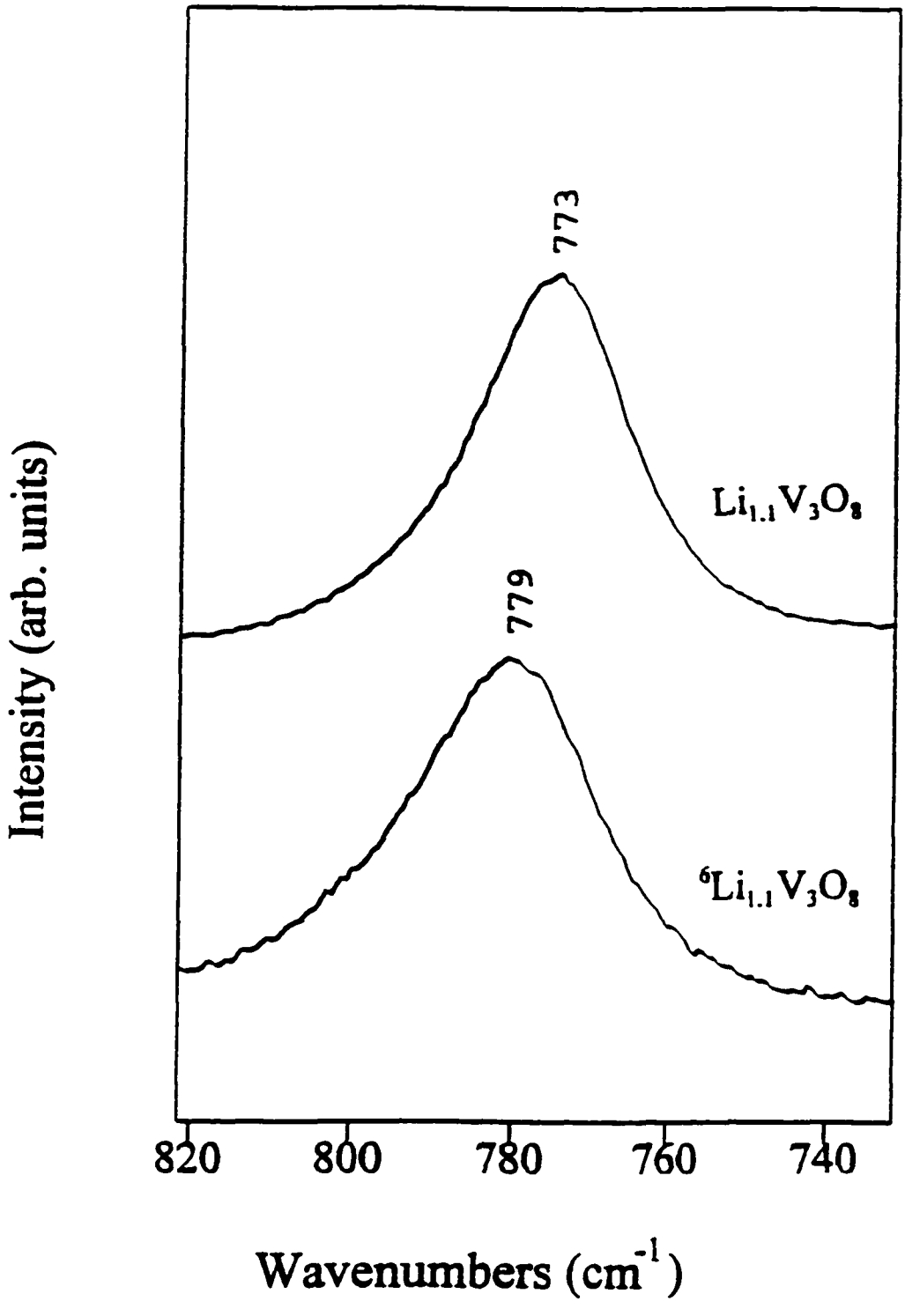

Fig. III-8 Polarized σ_{zz} Raman spectra of $Li_{1.1}V_3O_8$ and $^6Li_{1.1}V_3O_8$ from 700 to 820 cm^{-1}

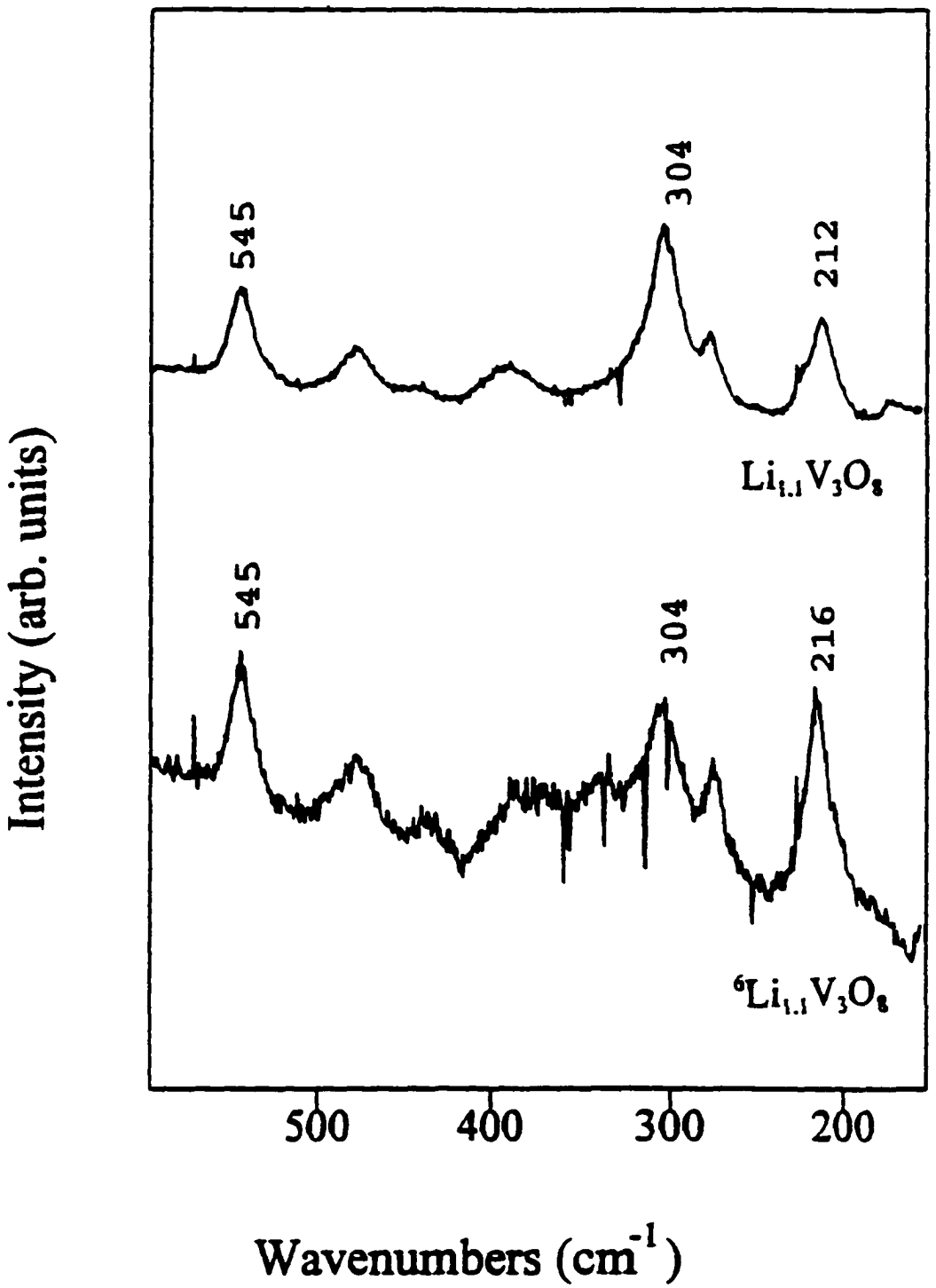

Fig. III-9 Polarized σ_{zz} Raman spectra of $Li_{1.1}V_3O_8$ and $^6Li_{1.1}V_3O_8$ (150-700 cm^{-1})

$Li_{1.1}V_3O_8$ between 900 and 1000 cm^{-1} is very similar to that of $^6Li_{1.1}V_3O_8$ (the spectrum is not shown), which indicates that isotopic substitution does not significantly affect the higher frequency V-O stretching vibrations. Additional spectral changes are observed in the α_{XY} measurement (Fig. III-10) upon isotopic substitution. In addition to the shifts in the 212 and 773 cm^{-1} bands, the 254 cm^{-1} band in $Li_{1.1}V_3O_8$ shifts to 257 cm^{-1} in $^6Li_{1.1}V_3O_8$, and the weak band at 604 cm^{-1} shifts to 609 cm^{-1}. The intensity of the 773 cm^{-1} band significantly increases, but the intensity of the 732 cm^{-1} band is remarkably reduced. These bands may originate in vibrational modes containing some component of lithium ion motion. From the data of Abello *et al.*[18], the 773 cm^{-1} band is likely to be related to the corner-sharing oxygen atomic motions. From the frequency shifts observed upon ^6Li substitution, it is reasonable to assume that the 212 and 254 cm^{-1} bands arise from the motion of lithium-oxygen polyhedra. However, the isotopic shifts do not simply scale according to the square root of the inverse mass ratio, because of the complicated nature of the normal modes. The lithium atoms are part of a chain structure of Li-O polyhedra which are structurally and dynamically coupled with each other. Because the corner-sharing oxygen O(3) is in common with VO_6, VO_5 and LiO_6 polyhedra, the isotopic replacement in LiO_6 may affect the motion of the VO_6 and VO_5 units, which results in a frequency shift at 773 cm^{-1}.

Fig. III-11 shows the Z(XY)Z polarized spectra of $Li_{1.1}V_3O_8$ and $Li_4V_3O_8$ in the α_{XY} measurement. The weak band at 732 cm^{-1} in $Li_{1.1}V_3O_8$ becomes a sharp strong band in the $Li_4V_3O_8$ phase and the 773 cm^{-1} band shifts to 768 cm^{-1}. The most marked change

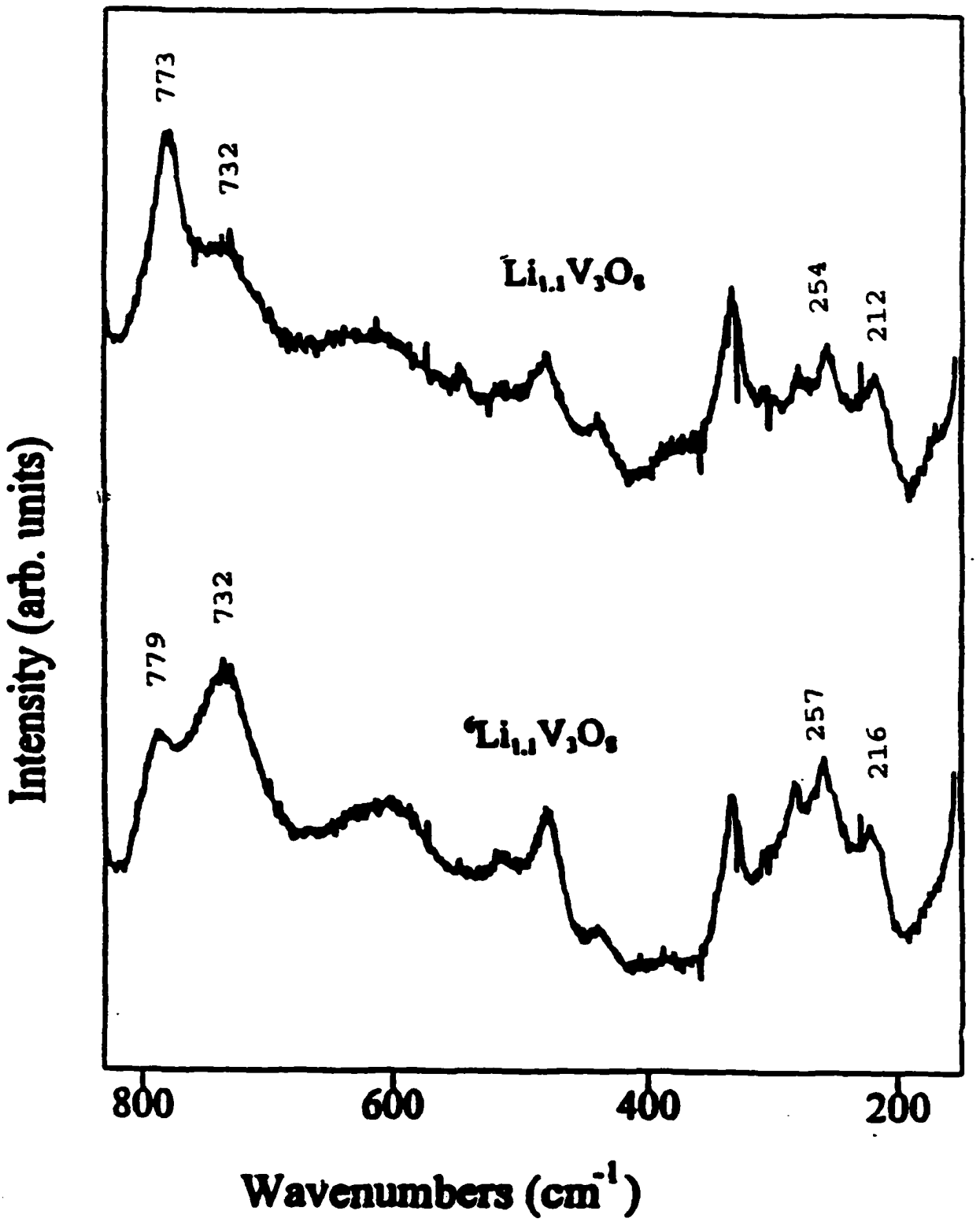

Fig. III-10 Polarized σ_{xy} Raman spectra of $Li_{1.1}V_3O_8$ and $'Li_{1.1}V_3O_8$ (150-830 cm^{-1})

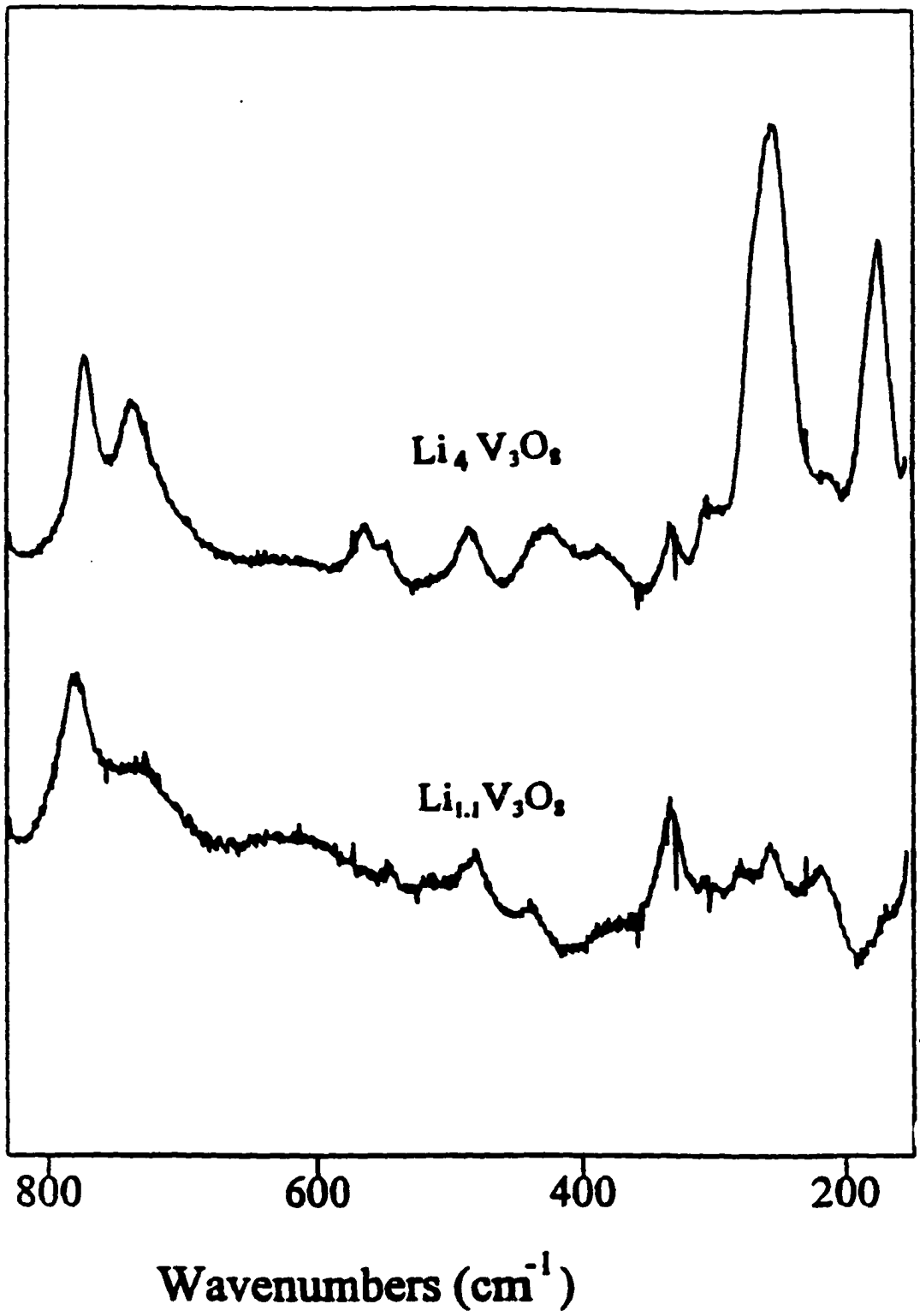

Fig. III-11 Polarized σ_{XY} Raman spectra of $Li_{1.1}V_3O_8$ and $Li_4V_3O_8$ (150-830 cm^{-1})

occurs in the low frequency region. The 254 and 171 cm^{-1} bands are very strong in the lithiated $Li_4V_3O_8$ phase. There are also other frequency shifts, as summarized in Table III-6. The weak feature at 604 cm^{-1} in $Li_{1.1}V_3O_8$ is not seen in the lithiated phase. The two weak features at 478 and 545 cm^{-1} shift to 483 and 562 cm^{-1}, respectively, and the scattering intensities significantly increase in the more highly lithiated phase. The weak sharp band at 438 cm^{-1} in the $Li_{1.1}V_3O_8$ phase becomes a broad band, and a new band at

Table III-6. Polarized Raman frequencies (cm^{-1}) of various lithium trivanadate phases

$Li_{1.1}V_3O_8$ (α_{zz})	$^6Li_{1.1}V_3O_8$ (α_{zz})	$Li_{1.1}V_3O_8$ (α_{xy})	$^6Li_{1.1}V_3O_8$ (α_{xy})	$Li_4V_3O_8$ (α_{xy})
993w		993m		
972w		972w		
869s		869s		
773vs	779vs	773s	779m	768s
		732sh	732s	732m
		604w	609w	
545m	545m	545w	545w	562m
478w	479w	478w	480w	483w
438sh	438sh	438w	438w	438w
383w	383w			387w
332w	334w	332s	332s	332m
304m	304m			304w
276w	276w	278w	279m	
		254m	256m	252vs
212s	216s	212m	216m	213w
				171vs

387 cm^{-1} appears in $Li_4V_3O_8$ phase. The scattering intensity of the 332 cm^{-1} band is markedly reduced in the lithiated phase and the 254 cm^{-1} band is barely seen in $Li_4V_3O_8$ phase.

The differences in the Raman spectra of $Li_{1.1}V_3O_8$ and $Li_4V_3O_8$ are due to the different coordination environments of lithium ions in the host structures. As the insertion of lithium ions proceeds, the lithium ions first take up the octahedral sites, then the tetrahedral sites causing a partial puckering of the V-O layers. Because lithium ions are coordinated to the corner-sharing oxygen atom O(3), it is no surprise that the atomic motions of the O(3) atoms are strongly affected by the insertion of lithium ions. In the $Li_4V_3O_8$ structure, all the tetrahedral sites are occupied by lithium ions, which may account for the extraordinary scattering intensities at 254 and 175 cm^{-1} as well as the other spectral changes observed upon lithiation of the $Li_{1+x}V_3O_8$ system. These spectroscopic features may serve as indication of the degree of intercalation during the cycling process of lithium rechargeable batteries.

3.4 Summary

The frequency shifts of the bands at 737, 825 cm^{-1} in the IR spectrum and 773 cm^{-1} in the Raman spectrum upon lithium-6 isotopic substitution establish that the corresponding vibrational modes, although primarily consisting of V-O stretching motion, also involve some lithium ion motion. Additionally, the lower frequency Raman bands at 212 and 254 cm^{-1} can be assigned to the motion of Li-O polyhedra, based on the isotopic shifts.

A factor group analysis allows the symmetry-based assignment of bands observed in the single crystal Raman spectra of $Li_{1.1}V_3O_8$. A number of bands in both the infrared and Raman spectrum have been described in terms of their constituent atomic or ionic motion by analogy with a published study of the V_2O_5 system. In particular, the strong band at 773 cm^{-1} is related to the corner-sharing oxygen atom O(3) between the two different VO_5 and VO_6 ribbons, and reflects, to some degree, the presence of the lithium ions due to the interaction between the lithium ions and the oxygen atoms of the polyhedra.

A comparison of the spectra of $Li_{1.1}V_3O_8$ and $Li_4V_3O_8$ shows that the intensities of the two bands at 254 and 173 cm^{-1} increase upon insertion of lithium ions. These spectroscopic changes may be employed to follow the structural evolution of $Li_{1.1}V_3O_8$ during lithium intercalation.

References:

1) J. B. Besenhard and R. Schöllhorn, *J. Power Sources*, **1**, 267 (1976/77).

2) S. Panero, M. Pasquali, and G. Pistoia, *J. Electrochem. Soc.*, **130**, 1225, (1983).

3) Y. Geronov, B. Puresheva, R. V. Moshtev, P. Zlatilova, T. Kosev, Z. Stoyvov, G. Pistoia and M. Pasquali, *J. Electrochem. Soc.*, **137**, 3338 (1990).

4) G. Pistoia, M. Pasquali, V. Manev and R. V. Moshtev, *Journal of Power Sources*, **15** 13 (1985).

5) K. West, B. Zachou-Christiansen, S. Skaarup, Y. Saidi, J. Barker, I. I. Olsen, R. Pynenberg and R. Kokshang, *J. Electrochem. Soc.*, **143**, 820 (1996)

6) B. Scrosati, *Brit. Poly. J.*, **20**, 219 (1988).

7) F. Bonino, M. Ottaviani, B. Scrosati and G. Pistoia, *J. Electrochem. Soc.*, **135**, 12 (1988).

8) A. D. Wadsley, *Acta Cryst.*, **10**, 261 (1957).

9) L. A. de Picciotto, K. T. Adendorff, D. C. Liles and M. M. Thackeray, *Solid State Ionics*, **62** 297 (1993).

10) G. Pistoia, ed. *Lithium Batteries: New Materials, Developments and Perspectives*, Elservier, Amsterdam, (1994)

11) G. Wang, J.Roos, D. Brinkmann, M. Pasquali and G. Pistoia, *J. Phys. Chem. Solids*, **54**, 851 (1993).

12) R. Tossici, R. Marassi, M. Berretoni, S. Stizza and G.Pistoia, *Solid State Ionics*, **57**, 227 (1992).

13) W. E. Steger, *Progress in Molecular Spectroscopy*, Teubner-Texte zur Physik, Band **20**, edited by R. Salzer, H. Kriegsmann and G. Werner 165 (1988).

14) C. Cazanelli, G. Mariotto, S. Passerini and F. Decker, *Solid State Ionics* **70/71** 412 (1994).

15) W. Huang and R. Frech, *Solid State Ionics*, **86-88**, 395 (1995).

16) Gamini Dharmasena, Ph. D dissertation, University of Oklahoma, 1994.

17) W. G. Fateley, F. R. Dollish, N. T. McDevitt and F. F. Bentley, "Infrared and Raman Selection Rules for Molecular and Lattice Vibrations: Correlation Method", John Wiley & Sons, Inc., New York (1072).

18) L. Abello, E. Husson, Y. Repelin and G. Lucazeau, *Spectrochim. Acta*, **39A**, 641 (1983).

19) L. D. Feridericson Jr., D. M. Hausen, *Anal. Chem.*, **35**, 818 (1963).

Chapter IV *In Situ* Raman Spectroscopy of $Li_xV_2O_5$ in a lithium Rechargeable Battery

4.1 Introduction

The lithium rechargeable battery represents one of the most promising energy sources for consumer, industrial, and military applications. This battery offers many advantages over conventional batteries, such as higher energy density, benign environmental impact, and long cycling life. The overall performance of a lithium rechargeable battery depends on the choice of cathode, anode, electrolyte, and the electrode-electrolyte interfacial properties. The capacity loss with repeated cycling is one of the technical difficulties which defer its commercialization. The capacity loss has been partly attributed to the irreversible structural changes in the cathode materials.

Lithium vanadium pentoxides ($Li_xV_2O_5$) have been explored as cathode materials in lithium rechargeable batteries. $Li_xV_2O_5$ can exist in different stable or metastable phases. Murphy *et al.*[1] reported the phase diagram of the Li_2O-V_2O_5 system, as shown in Fig. II-1. Three high temperature stable phases, α, β and γ, can be synthesized from solid state reactions around 650 °C. The low temperature phases, α, ε and δ can be obtained from chemical or electrochemical intercalation reactions. These low temperature phases can be transformed to high temperature phases through thermal reactions under certain reaction conditions. The structural and electrochemical behavior of these phases has

been extensively studied over the past two decades [2-6]. Lithium batteries with $Li_xV_2O_5$ as a cathode can be cycled between 3.8 and 2.0 V, with the corresponding x values from 0.01 to 2.0. Gourier *et al.* [5] and West *et al.* [6] reported the structural evolution of $Li_xV_2O_5$ accompanying the lithium intercalation process. During the charge/discharge processes, a series of phases were observed in the $Li_xV_2O_5$ host structure. These phases and the values of x for which the phases are reported to exist include α ($x < 0.1$), ε ($x = 0.35$-0.65), δ ($x = 0.9$ to 1.0), γ ($x = 1.0$ to 1.4), and ζ ($x > 1.4$). Due to the irreversible structural transition from the δ to the γ phase, the deintercalation of γ-$Li_xV_2O_5$ will not bring back the δ, ε, and α phases, but rather a new phase γ', which is structurally similar to the γ phase. The partial capacity fading of $Li_xV_2O_5$ observed upon repeated cycling has been attributed to irreversible structural changes in the host material [5].

Cartier *et al.*[2] reported the results of *in situ* X-ray diffraction and X-ray absorption spectroscopy of lithium ion intercalation into the $Li_xV_2O_5$ structure with the x values between 0.2 to 0.4. Although *in situ* X-ray and neutron diffraction measurements are presently the most powerful tools for identifying the structural changes of cathode materials [7, 8], certain structural modifications occurring during the cycling are not easily detectable by diffraction methods due to the following: 1) x-ray diffraction methods are most sensitive to phase transitions with a domain size larger than 200 Å; 2) the intercalation-related structural changes are caused by quite small rearrangements of

the MO_x polyhedra layers; 3) the highly discharged cathode materials, e.g. $x > 1.4$ in $Li_xV_2O_5$, exist in disordered states.

Raman and IR spectroscopy are very sensitive to local structural changes and have recently been used to characterize cathode materials [9-14]. These techniques therefore can be used as a complementary tool to the diffraction measurements. Recently, *in situ* vibrational spectroscopy has been used to study the lithium intercalation in carbon anodes [15, 16], interfacial behavior in fuel cells [17, 18] and the polymerization of conducting polymers [19]. In this study, *in situ* Raman spectroscopy was used to investigate the structural modifications of γ-$Li_{0.95}V_2O_5$ in an operating rechargeable cell during the deintercalation process.

4.2 Experimental

The electrochemical *in situ* Raman cell is schematically shown in Fig. IV-1. Initial efforts to study lithium intercalation in cathodes with *in situ* Raman spectroscopy used an experimental geometry in which the laser beam was incident on the side of a layered cell. This proved to be unsatisfactory because it is very difficult to obtain a clean surface from the side direction of the anode-electrolyte-cathode sandwich

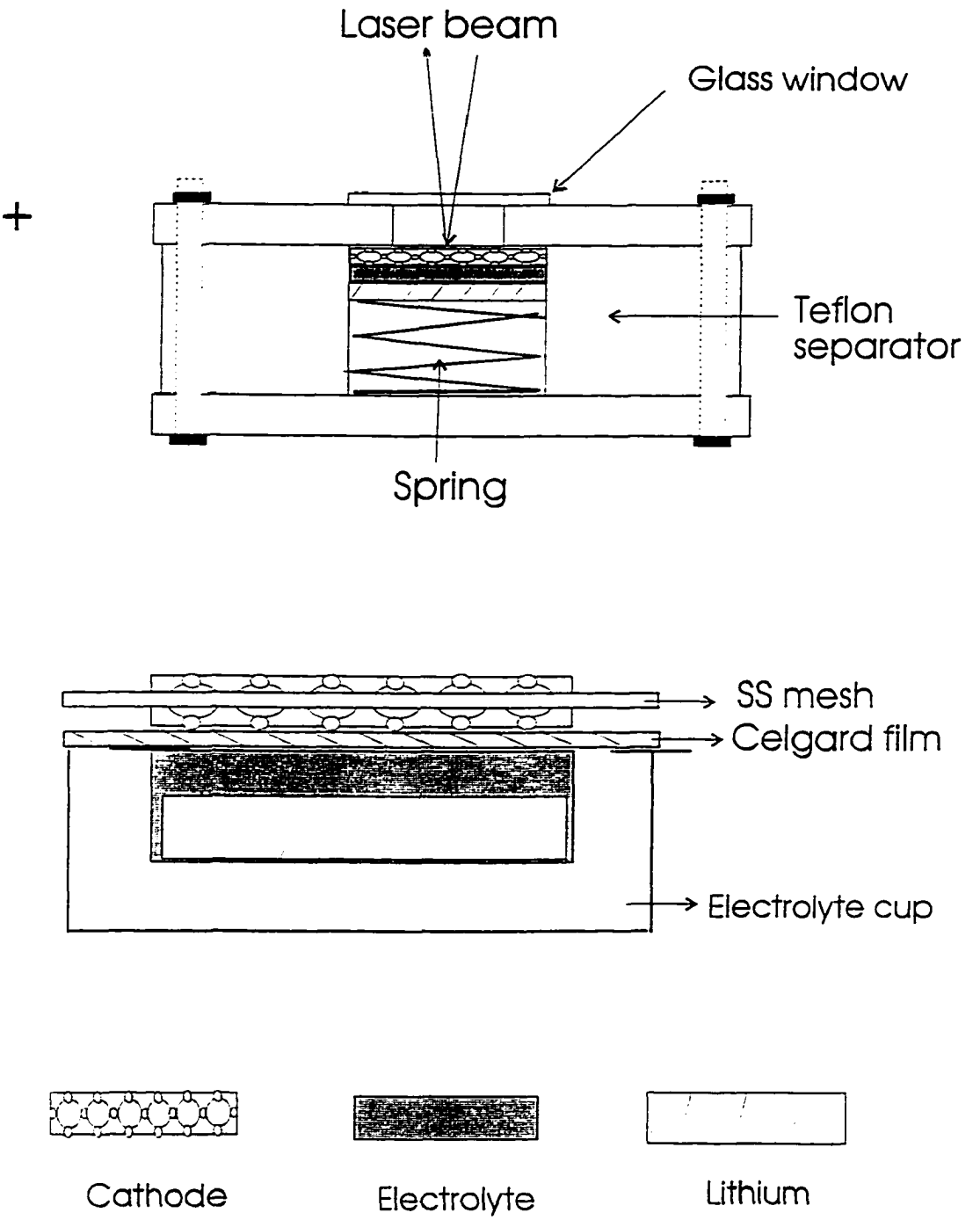

Fig. IV-1 *In situ* Raman cell

structure, and the Raman scattering intensities are very weak because of the roughness of the exposed surfaces. Therefore a backscattering geometry is used in which the laser beam was incident on the cathode from the end of the cell in a direction perpendicular to the sandwich layers. Backscattering cells have been used for *in situ* X-ray diffraction measurements [2, 8]. The *in situ* Raman cell was made of teflon and equipped with an optical window on the top. A stainless steel mesh was used as both current collector and cathode surpport. A detailed stretch can be found in Reference [15].

Low temperature (LT) γ-$Li_{0.95}V_2O_5$ was used as the starting cathode material. The γ-$Li_{0.95}V_2O_5$ was prepared following the procedures described by Murphy *et al.* [1] and characterized as described in Chapter 2. The cathode was made by mixing 85% (weight %) of γ-$Li_{0.95}V_2O_5$, 12% of Katjen carbon black and 3% of polyvinylidene fluoride (PVDF) in an ethanol solution. The slurry was then pasted on a stainless steel mesh and dried at 120 °C under vacuum for four hours. A 1M $LiClO_4$ propylene carbonate (PC)-dimethyl carbonate (DMC) solution (1:1 in volume) was used as the electrolyte and metallic lithium foil as the anode. A microporous polypropylene thin film (Celgard 2400™) was used as the separator. The cell was assembled in a dry box under an argon atmosphere and galvanostatically cycled between 2.0 and 3.7 volts with a current density of 0.15 mA/cm^2.

Raman spectra were measured at various potentials during the second discharge process with a Jobin-Yvon T64000 Raman system using an argon ion laser (514.5 nm) as the

excitation source. The experimental details are similar to that described in Chapters 2 and 3. A super holographic notch filter (Kaiser Optics) centered at 514.5 nm was used with the Raman system in the single monochromator mode. A thermoelectrically-cooled CCD detector measured the scattering intensity. All Raman spectra were collected at a spectral resolution of 2 cm^{-1} in a backscattering geometry through an 80x microscope which reduced the laser beam to a 2μ diameter spot focused on the cathode mixture. Because prolonged illumination with a relatively intense laser beam resulted in visible thermal damage to the cathode materials, all Raman spectra were collected with a laser intensity below 10 mW within 300 seconds, and the samples were visually checked with the microscope for damage after measurements.

4.3 Results and Discussion

Electrochemical intercalation/deintercalation reactions of lithium ions with γ-$Li_{0.95}V_2O_5$ cause topotactic structural modifications. Cocciantelli *et al.* [3, 20] studied the formation of different metastable phases during the electrochemical and chemical deintercalation processes. The γ-$Li_{0.95}V_2O_5$ structure consists of distorted $(VO_5)_n$ bipyramids as the basic structural units. The bipyramids share two edges and form double ribbons. These double ribbons are then connected through the apex oxygen atom to form puckered layers in the (010) plane. Lithium atoms occupy the 4c octahedral sites (space group C_{2v}^9) between the layers. The extraction of lithium atoms

from γ-$Li_{0.95}V_2O_5$ structure result in an unfolding of the puckered $(VO_5)_n$ layers to form a more relaxed structure. The γ-phase persists in the range $0.40<x<0.95$, but a new phase, γ', appears when x becomes smaller than 0.4. The γ' phase consists of similar puckered $(VO_5)_n$ layers as in γ-$Li_{0.95}V_2O_5$. X-ray diffraction results showed slight changes of the a- and c- parameters accompanying extraction of lithium ions and the rearrangements of the $(VO_5)_n$ structural layers to accommodate the electronic changes.

Upon lithium insertion, the γ-phase retains its topotactic structure until x reaches 1.4, where a new phase, ζ, appears. X-ray diffraction data [3] showed that the ζ phase also contains double VO_5 ribbons, and its unit cell parameters are close to those of γ-$Li_{0.95}V_2O_5$. Several new features appear in the diffraction spectrum for the composition x = 1.8. However, the attempt to index the diffraction pattrern with an orthorhombic cell was not fully satisfactory. In the ζ phase, some of the inserted lithium ions are located at tetrahedral positions and may cause only local structural modifications of the V-O layers which are not easily detectable by x-ray diffraction methods.

The discharge behavior of a γ-$Li_{0.95}V_2O_5$-based cell is shown in Fig. IV-2. The curve was recorded during the second cycle with a potential between 3.7 and 2.0 V. Two plateaus, at 3.5 V and 2.4 V, were observed during the discharge process. The electrochemical behavior of γ–$Li_xV_2O_5$ during the second cycle will generally reflect the cathode behavior of a $Li_xV_2O_5$-based lithium battery. The *in situ* Raman spectra were recorded during the discharge process at different potentials: 3.6 V (x = 0.1), 3.3 V (x =

0.93), 2.40 V (x = 1.15), and 2.15 V (x = 2.05). The first composition corresponds to the γ' phase, the next two compositions to the γ phase, and the last composition to the ζ phase, as described by Cocciantelli *et al.* [3].

The *in situ* Raman spectra recorded at the four potentials are shown in Figs. IV-3 and 4 and their frequencies are summarized in Table IV-1. These spectra can be conveniently divided into a high frequency region (800 to 1100 cm^{-1}) and a low frequency region (200 to 800 cm^{-1}). The γ'-$Li_{0.1}V_2O_5$ spectrum has four bands at 986, 960, 940, and 873 cm^{-1} in the high frequency region. The γ-$Li_{0.93}V_2O_5$ spectrum shows five peaks at 983, 968, 960, 940 and 875 cm^{-1} and the γ-$Li_{1.15}V_2O_5$ spectrum has peaks at 983, 960, 940, and 875 cm^{-1}. Although the three spectra are similar in terms of the band positions, there are differences in spectral intensities. The intensities of bands at 986 and 940 cm^{-1} in the γ'-$Li_{0.1}V_2O_5$ phase are significantly decreased compared to the other two phases. The spectrum measured at x = 2.05 in the ζ phase appears quite different with respect to the γ and γ' phases. Although these strong bands at 984 and 943 cm^{-1} are similar to the other phases, the 960 cm^{-1} band present in the other three compositions appears to split into two weak bands at 970 and 957 cm^{-1}. In addition, the strong band around 875 cm^{-1} disappears in the ζ-phase.

The spectral differences in the low frequency region (200 to 800 cm^{-1}) are equally striking for the four compositions. The γ'-$Li_{0.1}V_2O_5$ spectrum shows several medium

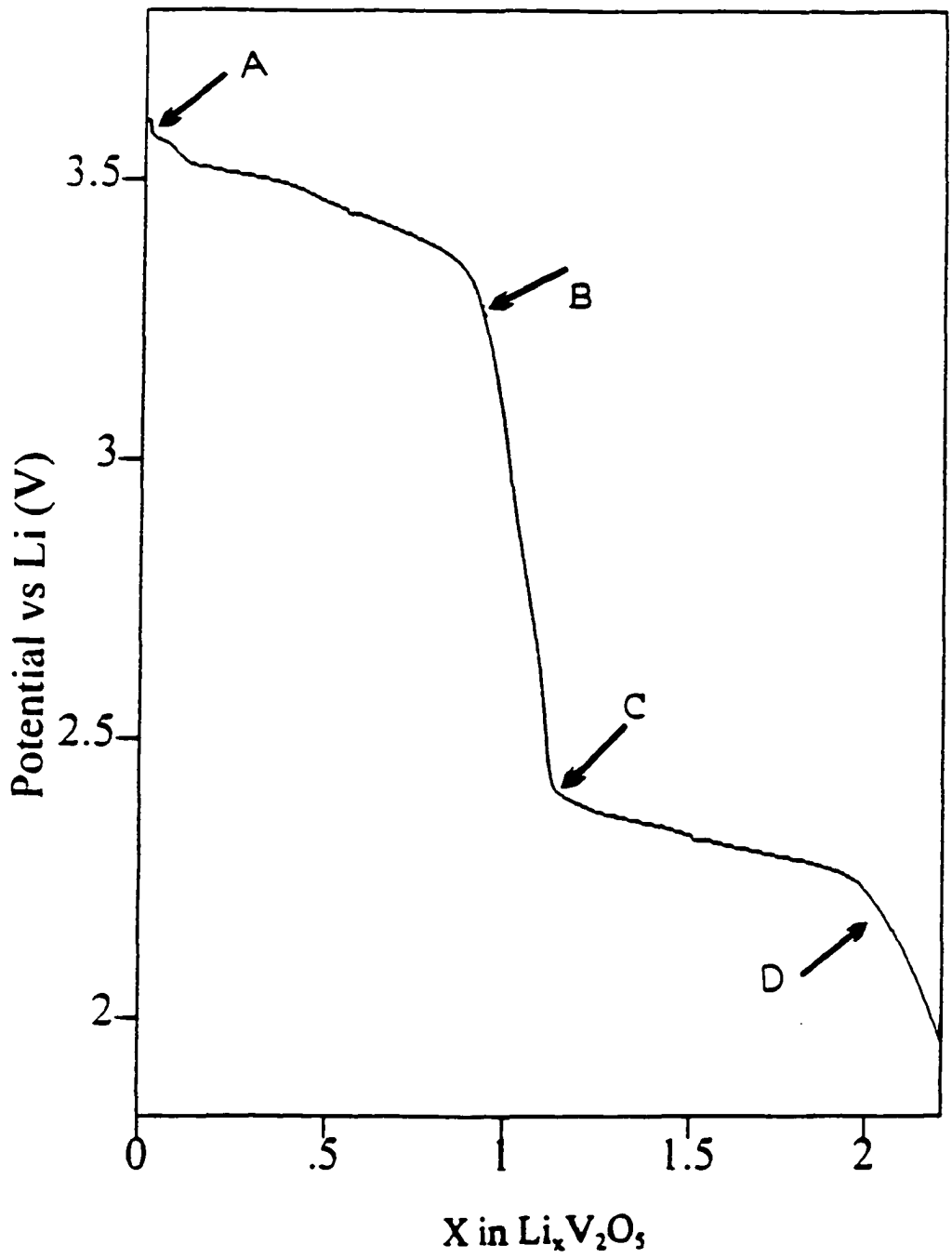

Fig. IV-2 Discharge curve of the second cycle with a current density of 0.15 mA/cm^2, A (x=0.1), B (x=0.93), C (x=1.15), and D (x=2.05)

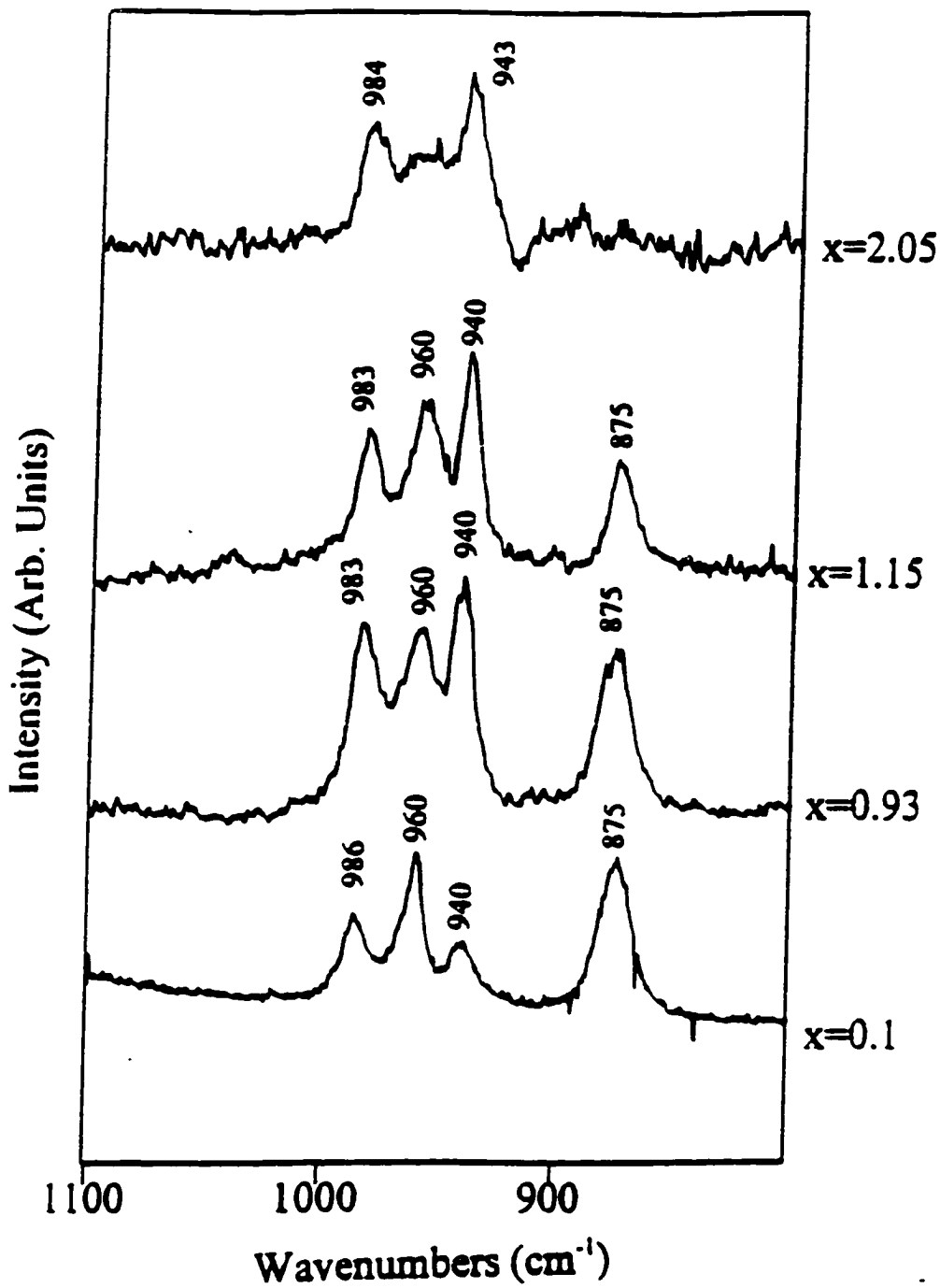

Fig. IV-3 Raman spectra of $Li_xV_2O_5$ from 800 to 1100 cm^{-1} for different intercalation degrees: x=0.1 (A), 0.93 (B), 1.15 (C), and 2.05 (D). The major frequencies are labeled on the spectra.

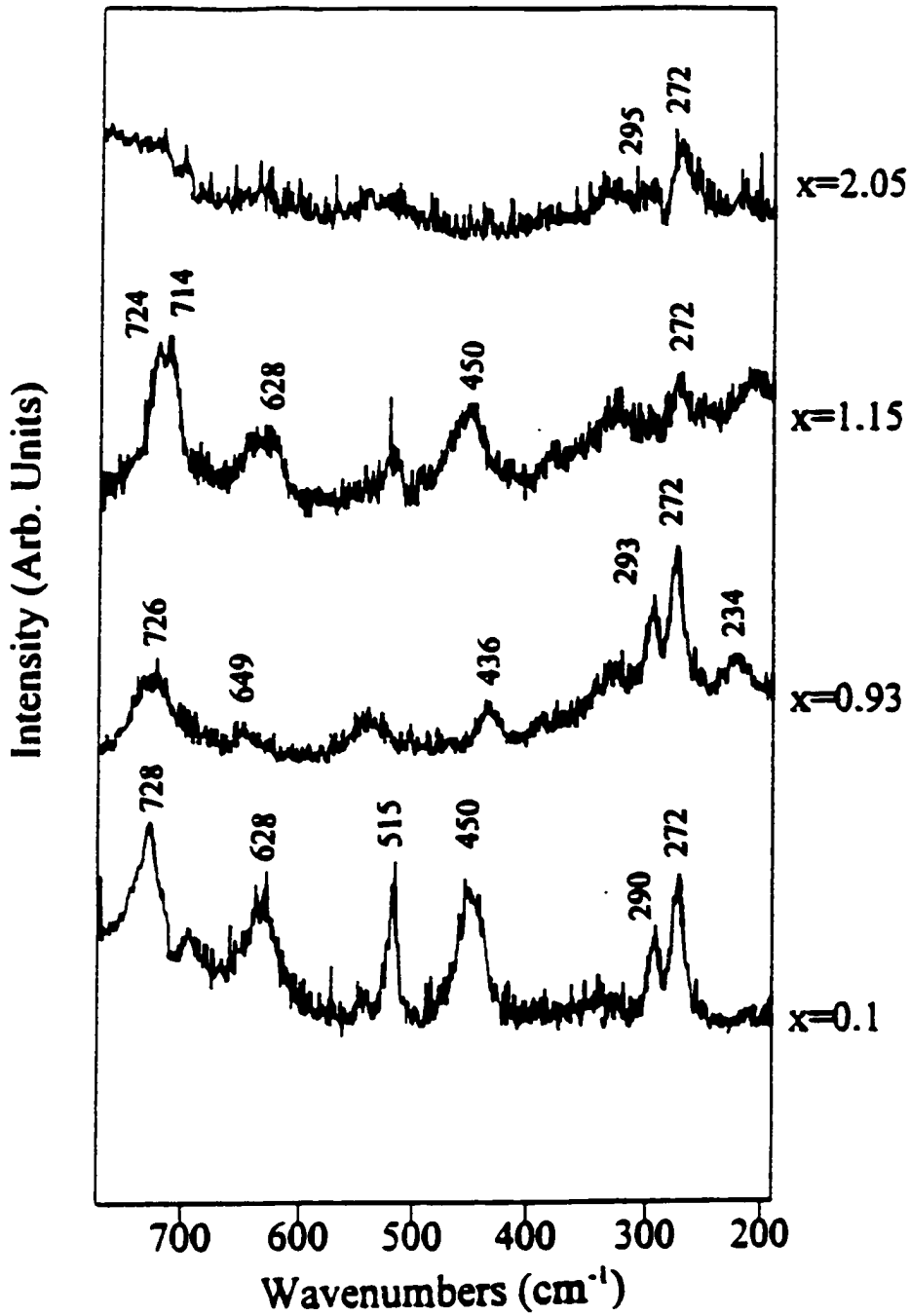

Fig. IV-4 Raman spectra of $Li_xV_2O_5$ from 200 to 800 cm^{-1} for different intercalation degrees: x=0.1 (A), 0.93 (B), 1.15 (C), and 2.05 (D). The major frequencies are labeled on the spectra with a unit cm^{-1}.

intensity bands at 728, 697, 628, 515, 450, 290 and 272 cm^{-1}. There are also several weak features at 697, 543, and 437 cm^{-1}. The three sharp peaks at 450, 515 and 628 cm^{-1} in the γ'-$Li_{0.1}V_2O_5$ spectrum disappear in the spectrum of the γ-$Li_{0.93}V_2O_5$ phase. In the latter spectrum, there are several weak bands at 649, 436, 328, and 234 cm^{-1}; in addition the strong peak at 728 cm^{-1} becomes broadened and its peak position shifts to 726 cm^{-1}. It is especially interesting that the spectrum of γ-$Li_{1.15}V_2O_5$ shows several distinctive changes relative to that of γ-$Li_{0.93}V_2O_5$. The 728 cm^{-1} band further shifts to lower frequency and splits into two bands at 724 and 714 cm^{-1}. The band at 293 cm^{-1} in γ-$Li_{0.93}V_2O_5$ and 290 cm^{-1} in γ'-$Li_{0.1}V_2O_5$ is not seen in the γ-$Li_{1.15}V_2O_5$ phase. The scattering intensity of the 272 cm^{-1} band was noticeably reduced in γ-$Li_{1.15}V_3O_8$. There is also a broad weak feature around 217 cm^{-1} which is also quite visible in the two γ phase compositions. The spectrum recorded at $x = 2.15$ has a very high noise level, but several weak peaks appear in the low frequency region, such as the bands at 326, 295, 272, and 217 cm^{-1}.

Several *ex situ* vibrational spectroscopic studies of $(VO_5)_n$-based structures have been reported [10, 13, 14, 21, 22]. The assignments of several lithium vanadium oxide materials were described in Chapter 2, as observed in both the transmission and the Raman spectra [12]. It should be noted that these assignments rely heavily on earlier

Table IV-1. Raman frequencies (cm^{-1}) of various phases

γ'-$Li_{0.1}V_2O_5$	γ-$Li_{0.93}V_2O_5$	γ-$Li_{1.15}V_2O_5$	ζ-$Li_{2.05}V_2O_5$
986 m	983 s	983 s	984 s
--	968 sh	--	970 sh
960 s	960 s	960 s	957 w
940 m	940 s	940 s	943 s
875 s	875 s	875 s	--
728 s	726 s	724 s	720 w
697 w	--	714 s	--
628 m	649 w	628 m	--
543 w	543 w	--	--
515 s	516 w	518 m	--
450 s	--	450 s	--
437 sh	436 m	--	--
--	328 w	328 w	326 w
290 m	293 m	--	295 w
272 s	272 s	272 m	272 w
	234 w	217 sh	217 sh

assignments for the V_2O_5 structure proposed by Granquivst *et al* [22]. and Lucazeau *et al* [13]. Hence the description of the modes given here must be regarded as tentative. The strong bands at 986 cm^{-1} in γ'-$Li_{0.1}V_2O_5$, 983 cm^{-1} in γ-$Li_{0.93}V_2O_5$ and γ-$Li_{1.15}V_2O_5$, and 984 cm^{-1} in the ζ-phase, are related to the A_g symmetric vibrations of the shortest vanadium oxygen bond, which is V=O. The vibrations in the range between 940 and 970 cm^{-1} contain contributions from the motion of the apex or base oxygen atoms in the pyramids. The vibration around 875 cm^{-1} originates in the bending modes of the corner-sharing oxygen atoms. The assignments of bands below 800 cm^{-1} are very complicated and even more ambiguous. The peaks at 730 cm^{-1} and 272 cm^{-1} are assigned to vibrations involving the edge-sharing oxygen atoms. It is clear that more research needs to be done in order to place the vibrational mode assignments of $Li_xV_2O_5$ on a firmer basis.

During the discharge process from 3.75 V to 2.0 V, the formation of the γ', γ, and ζ phases originates in the rearrangements of the V-O layers. X-ray diffraction data show that $Li_xV_2O_5$ has similar diffraction patterns for x = 0.1 to 1.4, but the lattice parameters changes with the degree of lithium intercalation [3]. The unit cell parameter along the (001) direction increases from 10.03 Å (x = 0.05, γ') to 10.70 Å (x = 1.4, γ), whereas along the (100) direction it decreases from 9.93 Å (γ') to 9.74 Å (γ).

The Raman spectra provide additional information about local structures in these phases. The spectrum of the highly deintercalated γ-$Li_xV_2O_5$ (x = 0.1) appears to be quite similar

to that of γ-$Li_{0.93}V_2O_5$. The extraction of lithium atoms does not return the structure of γ-$Li_{0.93}V_2O_5$ back to that of V_2O_5, but mantains the basic structure of the original intercalated phase (γ). The relative scattering intensity changes of the bands at 983, 960, and 940 cm^{-1} suggest that the $(VO_5)_n$ pyramids adopt different arrangements in γ-$Li_{0.93}V_2O_5$ and γ'-$Li_{0.1}V_2O_5$. The shift of the 983 cm^{-1} band in γ-$Li_{0.93}V_2O_5$ to 986 cm^{-1} in the γ'-phase may originate in the partial regeneration of the V=O double bond properties upon removal of lithium ions.

The Raman spectra recorded at x = 0.93 and 1.15 are quite interesting. The discharge curve (Fig. IV-2) shows a sudden potential drop from 3.3 V to 2.4 V for $0.9 < x < 1.2$. This drop originates in the reduction of V^{5+} to V^{4+} when lithium atoms take up the tetrahedral sites. However the x-ray diffraction data show only a slight unit cell change for this reduction process [3]. Although the *in situ* Raman spectra at x = 0.93 and 1.15 are similar in the high frequency region (800 to 1100 cm^{-1}), the two phases show quite distinctive spectral behavior below 800 cm^{-1}. The spectral changes in γ-$Li_{1.15}V_2O_5$ relative to γ-$Li_{0.93}V_2O_5$ include the splitting of the band at 724 cm^{-1}, the absence of the band at 293 cm^{-1} and the presence of bands at 628, 518 and 450 cm^{-1}. These data argue strongly that lithium ion occupancy of the tetrahedral sites leads to a significant local structural modification.

The Raman spectrum of the ζ-phase shows a very different profile compared with the other three phases. The strong peak at 875 cm^{-1} is not observed in this phase. In general the overall Raman scattering intensities are very weak, which may be attributed in part to

inhomogeneous broadening originating in the increased local disorder for values of x>1. In turn the increased local disorder may be responsible for the capacity decline of the cathode. On the other hand, $Li_xV_2O_5$ with x > 1 are highly colored materials , which may also reduce the Raman scattering intensities. At this high degree of intercalation, the fluorescence of the transition metal oxides also presents another experimental difficulty in recording the Raman spectra.

4.4 Conclusion

In situ Raman spectra of $Li_xV_2O_5$ have been recorded on an operating lithium rechargeable battery. The spectral changes during the lithium deintercalation process provide important structural information that is not obtainable via other structural analysis methods. Differences in the spectra of γ, γ' and ζ phases make it possible to identify the presence of these phases during lithium intercalation/deintercalation reactions. The frequencies and intensities which appear to be most sensitive to changes in the degree of lithium intercalation occur in bands between 200 and 750 cm^{-1}, although changes are also observed in the region from 800 to 1000 cm^{-1}. It is particularly noteworthy that significant differences are seen between the spectrum of γ-$Li_{0.93}V_2O_5$ and that of γ-$Li_{1.15}V_2O_5$. These two materials are ostensibly in the same phase, differing only in their lithium content.

This study demonstrates the potential of *in situ* Raman spectroscopy as a powerful technique for identifying phase changes as well as studying local structural changes upon insertion/removal of lithium ions of intercalation compounds during charge/discharge processes.

References:

1. D.W. Murphy, P.A. Christian, F.J. Disalvo, and J.V. Waszczak, *Inorg. Chem.*, **18** 2800 (1979).

2. C. Cartier, A. Tranchant, M. Verdaguer, M. Messina and H. Dexpert, *Elctrochimica Acta*, **35** 889 (1990).

3. J.M. Cocciantelli, M. Menetrier, D. Delmas, J.P. Doumerc, M. Pouchard, and P. Hagenmuller, *Solid State Ionics*, **50** 99 (1992).

4. J.M. Cocciantelli, M. Menetrier, C. Delmas, J.P. Doumerc, M. Pouchard, M. Broussely, *Solid State Ionics*, **78** 143 (1995).

5. D. Gourier, A. Tranchant, N. Baffier, and R. Messina, *Electrochim. Acta*, **37** 2755 (1992).

6. K. West, B. Zachau-Christiansen, T. Jacobson, and S. Skaarup, *Solid State Ionics*, **76** 15 (1995).

7. J.N. Reimers and J.R. Dahn, *J. Electrochem. Soc.*, **139** 2091 (1992).

8. M.N. Richard, I. Koetschau, and J.R. Dahn, *J. Electrochem. Soc.*, **144** 554 (1997).

9. C. Julien, I. Ivanov, and A. Gorenstein, *Materials Science and Engineering*, **B33** 168 (1995).

10. A. Talledo and C.G. Granqvist, *J. Phys. D: Appl. Phys.*, **27** 2445 (1994).

11. S.J. Wen, T.J. Richardson, L. Ma, K.A. Striebel, P.N. Ross, and E.J. Cains, *J. Electrochem. Soc.*, **143** L136 (1996).

12. X. Zhang and R. Frech, *Electrochimica Acta*, **42** 475 (1997).

13. L. Abello, E. Husson, Y. Repelinand, and G. Lucazeau, *Spectrochimica. Acta*, **39A** 641 (1983).

14. P. Clauws, J. Broeckx, and J. Vennik, *Phys. Stat. Sol.*, **131 B** 459 (1985).

15. W. Huang and R. Frech, *J. Electrochem. Soc*, **submitted** .

16. M. Inaba, H. Yoshida, and Z. Ogumi, *L. Electrochem. Soc.*, **143** 2572 (1996).

17. Q. Fan, C. Pu, K.L. Ley, and E.S. Smotkin, *J. Electrochem. Soc.*, **143** L21 (1996).

18. R. Kostecki and F. McLarnon, *J. Electrochem. Soc.*, **144** 485 (1997).

19. M. Mostefai, M.C. Pham, J.-P. Marsault, J. Aubard, and P.-C. Lacaze, *J. Electrochem. Soc.*, **143** 2116 (1996).

20. J.M. Cocciantelli, P. Gravereau, J.P. Doumerc, M. Pouchard, and P. Hagenmuller, *J. Solid State Chem.*, **93** 497 (1991).

21. E. Cazzanelli, G. Mariotto, S. Passerini, and F. Decker, *Solid State Ionics*, **70/71** 412 (1994).

22. A. Talledo and C.G. Granqvist, *J. Appl. Phys.*, **77** 4655 (1995).

Chapter V Mesostructural Materials as Electrodes in Lithium Rechargeable Batteries

5. 1 Introduction

Transition metal oxides which undergo intercalation reactions are particularly of interest in lithium rechargeable batteries. Chapter One has given a brief overview of different electrode materials. These intercalation compounds include layered structures, such as lithium vanadium pentoxide, lithium cobalt oxide, lithium nickel oxide and tunnel-like intercalation structures such as spinel $Li_{1+x}Mn_2O_4$. One of the most important properties of cathode materials is that lithium ions can be reversibly inserted/extracted from the host structures. To date, vanadium and manganese oxides have attracted the most interest for their potential applications in lithium batteries, due to their high energy density and relatively low costs [1].

Intensive research has been devoted to increasing capacities and improving reversibility of cathodes. For most transition metal oxide cathodes the lithium intercalation process is not completely reversible. After a deep discharge process and long cycling, a fraction of the lithium ions may remain inside the host structures, which causes a decrease in the cathode capacities. Repeated charge/discharge of a lithium battery may cause permanent structural modification in the cathode. Intercalation of lithium ions may also cause

phase transitions such as the Jahn-Teller distortion as found in spinel $Li_xMn_2O_4$ [2, 3]. Extensive research is currently underway in order to improve the existing cathode materials and find new candidates for better battery performance.

Low temperature solution synthesis techniques [4] such as the sol-gel process provide interesting cathode materials for use in lithium batteries. Amorphous materials from sol-gel processes have finer particle sizes and somewhat lower diffusion barriers for lithium ions compared to the crystalline phases. Thus cathode materials prepared from solution reactions have higher energy densities and longer cycling life [4-6].

There has been an intense research effort to find new cathode materials with more open structures. Although amorphous cathodes have better electrochemical performance when compared to the crystalline materials, their basic structural units are similar to those of the crystalline phases. However lithium ions must still overcome a relatively high diffusion barrier to transport through the interstitial tunnels or layers formed by OM_x polyhedra during the charge/discharge processes, and lithium ions may become stuck in the host structure after many repeated cycles.

The intercalation of poly(ethylene oxide) into a V_2O_5 xerogel was reported by Liu *et al.*[7] and Costa *et. al.* [8]. The PEO-modified V_2O_5 showed an improvement of the conductivity and diffusion coefficient for the lithium ions. Manev *et al.* [9] attempted to modify the $Li_xV_3O_8$ structure by introducing small amounts of inorganic compounds

into the V-O layers. The expanded $Li_xV_3O_8$ exhibited higher capacity and better reversibility compared to the regular $Li_xV_3O_8$. They pointed out that the expansion of the interlayer spacing leads to an increased mobility and enhanced distribution of the lithium ions in the $Li_xV_3O_8$ layers. Recently, Leroux *et al.* [10] inserted polyaniline into the interlayer spacing of V_2O_5 xerogel. The modified V_2O_5 also showed an improved capacity and reversibility. The authors attributed the improvement to the decrease of electrostatic and steric effects around lithium ions inside the enlarged layers. Nanjundaswamy *et al.* [11] prepared a series of three-dimensional framework structures such as $Li_xFe_2(SO_4)_3$ and $Li_xTi_2(PO_4)_3$. The interconnected open channels formed from the XO_4 (X=S or P) tetrahedra and MO_6 (M=Fe, Ti, Cr, or V) octahedra units allow fast transport of lithium ions. Electrochemical data showed that the $Li_xFe_2(SO_4)_3$ structure can be cycled between 2.0 and 3.9 V with a capacity above 100 mAh/g. The synthesis of three dimensional open structural materials provides a new direction for the preparation of cathode materials.

Three-dimensional open structural materials also exist in nature, such as zeolites. Zeolites are a group of silicate or aluminosilicate materials. Natural zeolites are formed in the crust of the earth through hydrothermal reactions and characteristically have a three-dimensional framework with open pore sizes up to 14 Å. The basic building blocks in zeolites are SiO_4 and AlO_4 tetrahedra. Synthetic zeolites are obtained from hydrothermal reactions under relatively mild conditions. Small organic molecules are often used as structure-directing agents or templates during the formation of zeolites. To

some degree, framework structure, pore size and distribution can be controlled by changing the structure-directing molecules or reaction conditions [12].

Hydrothermal synthesis has also been employed for the preparation of transition metal oxides [1, 9, 11, 13-15] for battery applications. Cathode materials resulting from hydrothermal reactions have more open structures compared to either the crystalline materials from high temperature solid state synthesis or amorphous cathode materials from solution reactions or sol-gel processes. The enlarged interlayers resulting from hydrothermal reactions facilitate transport of lithium ions during the cycling process.

An important class of materials with open structures are mesoporous materials, which have similar structures to zeolites, but with larger pore sizes (20 to 100 Å). Beck *et al.* [16] first reported the synthesis of inorganic mesoporous materials, designated as M41S, by using ionic surfactant template molecules. The M41S materials are characterized by: 1) an ordered channel system with cubic, lamellar or hexagonal pores; 2) large pore sizes in the range 20 to 100 Å; 3) high internal specific surface areas. Typically the mesosize channels are inter-connected throughout the three-dimensional framework. Mesoporous materials have been extensively studied as heterogeneous catalysts in selective cracking of petroleum products. Since the discovery of the M41S in 1992, a tremendous amount of research has been directed to understand the templating mechanism and formation kinetics [17-20]. Recently transition metal-substituted mesostructural materials were reported, such as vanadosilicates [21, 22], manganosilicates [23], titanosilicates [24] and

galloaluminosilicates [25], where the metal ions are incorporated into the silicate walls. Morey *et al.* [26] reported that vanadium oxide species can be impregnated into the mesoporous channels through solution reactions of previously calcined samples.

Mesostructural materials were initially prepared using cationic or anionic surfactants [17, 18, 20]. Bagshaw et al. [27] reported that mesostructural materials can also be prepared using PEO-based nonionic surfactants. The mesoporous silicates, as well as alumina-, titania-, and zirconia-subsituted silica, have been synthesized by hydrolysis reactions in the presence of polyethylene oxide (PEO) surfactants. Also pure alumina, tin oxide, and zirconia were prepared by hydrolysis of the corresponding alkoxides in the presence of a variety of nonionic PEO-based surfactants as the templating agents. The templating molecules can be removed by heat treatment around 500 °C.

The structural characteristics of the mesoporous M41S materials are highly desirable for electrode applications in rechargeable lithium batteries. The unique, well-defined mesosize channels provide a fast transport tunnel for lithium ions, thereby improving the reversibility and cycling properties. The mesostructural materials possess much higher specific surface areas (1000 cm^2/g) when compared to the crystalline, amorphous or the nanosize materials, which will increase their electrochemical capacities. The redox reactions around the incorporated transition metal ions provide the necessary potential for electrochemical processes. The mesostructural materials may accommodate large amounts of lithium ions without causing severe structural modification because of the

existence of the open channels. This property would be extremely important for cathode materials in lithium rechargeable batteries. This part of the research explores, for the first time, the preparation and application of mesostructural materials as electrodes for lithium rechargeable batteries, emphasizing manganese oxide-based mesostructural materials as cathodes and tin oxide-based mesostructural materials as anodes.

5.2 Manganese Oxide-Based Mesostructral Materials as Cathodes

Manganese-substituted mesoporous materials were first prepared by Zhao and Goldfarb [23] using as precursors $MnCl_2$ and tetraethyl orthosilicate (TEOS) in the presence of cetyltrimethylammonium bromide (CTAB). The manganese atoms substituted into the frameworks in Mn:Si molar ratios which ranged from 0.0004 to 0.1. For the electrochemical application of the mesoporous materials, high Mn:Si molar ratios are desirable in order to increase cathode capacities. In this work several Mn-substituted mesostructures and manganese oxide-based mesostructures have been prepared using different templating surfactants.

5.2.1 Preparation of manganese oxide-based mesostructural materials

Six manganese oxide-based mesostructural materials were synthesized following the compositions shown in Table V-1.

Table V-1. Compositions of the resultant gels

Sample #	SiO_2	Li_2O	MnO_2	Templates	H_2O	Synthesis
MFZ-1	1.00	0.25	0.20	0.45 CTAB	65.00	175 °C, 42 hrs
MFZ-2	--	0.50	1.00	0.15 PEO	80.00	170 °C, 72 hrs
MFZ-3	1.00	0.25	0.20	0.45 CTAB	80.00	170 °C, 36 hrs
MFZ-4	1.00	0.25	1.00	0.26 CTAB	180.00	165 °C, 37 hrs
MFZ-5	1.00	0.25	1.00	0.26 CTAB	180.00	167 °C, 40 hrs
MFZ-6	--	1.00	1.00	0.10 PEO	150.00	160 °C, 24 hrs

Sample MFZ-1

A 12.5 ml 2M LiOH solution was added under constant stirring to a CTAB solution (30 ml, 25% (weight), Aldrich). This solution was then mixed with 1.73 g of manganese acetate (Alfa Aesar) and 10.44 g of TEOS (Alfa Aesar) and the total volume was brought to 75 ml. The gel obtained using this method was stirred at 90 °C for four hours

and then treated in a Teflon-lined Parr pressure reactor at 175 °C for 42 hours. The solid product was recovered and calcined at 500 °C for four hours.

Sample MFZ-2

A 50 mL 2M LiOH solution was added under constant stirring to a PEO-surfactant (15 mL. 0.1 M $C_{16}(EO)_{10}$, TCI America). To the solution 12.6 g of $MnCl_2$ was added and the total volume was adjusted to 160 mL with distilled water. The resulting suspension was stirred at 90 °C for four hours and then hydrothemally reacted in a Teflon-lined Parr reactor at 170 °C for 72 hours. The solid product was recovered and calcined at 500 °C for four hours.

Sample MFZ-3

A 12.5 mL 2M LiOH solution was added under constant stirring to a CTAB solution (30 mL, 25% (weight), Aldrich). This solution was then combined with 6.12 g of sodium silicate (N brand, 27% silica, Aldrich) and 2.87 g of manganese nitrate (Alfa Aesar). The gel was stirred at 90 °C for four hours and then transferred to a Parr pressure reactor where it was treated at 170 °C for 36 hours. The solid product was recovered and calcined at 500 °C for four hours.

Sample MFZ-4

A 13.5 mL 2M LiOH solution was added under constant stirring to a CTAB solution (21 ml, 25% (weight), Aldrich). To this solution was added 10.58 g of TEOS solution and 14.29 g of $Mn(NO_3)_2 \cdot 4H_2O$ (Aldrich). The gel was then treated under hydrothermal conditions at 165 °C for 37 hours. The resulting product was recovered and calcined at 520 °C for eight hours.

Sample MFZ-5

A 13.5 mL 2M LiOH solution was added under constant stirring to a CTAB solution (21 ml, 25% (weight), Aldrich). To the solution was added 14.02 g of $Mn(NO_3)_2 \cdot 4H_2O$ (Aldrich), 10 mL of 37% HCl and 160 ml of distilled water. Hydrothermal treatment was carried out at 167 °C for 40 hours.

Sample MFZ-6

4.25 g of PEO-based surfactant (TCI America) was dissolved in 180 mL of distilled water at 70 °C. To the solution was added 5.20 g of $LiOH \cdot H_2O$ (Fluka). Manganese (II) chloride was used as the manganese source. 7.87 g of $MnCl_2$ reacted with 8.50 g of sodium ethoxide in 100 mL 50% (vol) ethanol according the following reaction:

$$MnCl_2 + 2Na(OCH_2CH_3) \rightarrow Mn(OCH_2CH_3)_2 + 2NaCl$$

The above suspension containing the $Mn(OCH_2CH_3)_2$ precursors was combined with the PEO surfactant solution. The resulting gel was hydrothermally treated at 160 °C for 24 hours. The final product was recovered and calcined at 500 °C for 4 hours.

5.2.2 **Structural characterization**

A) Transmission electron microscopy (TEM)

The TEM experiments were performed on a JEN-2000FX Electron Microscope at 200 kV. The sample was suspended in isopropyl alcohol with sonication and then cast onto Lacey™ carbon 200 to form a single layer. The TEM photographs provide direct evidence for the formation of mesosize channels.

B) Infrared spectroscopy

FTIR spectroscopy was recorded using a Bruker IFS66V infrared system in the range 400 to 4000 cm^{-1}. The samples were prepared as KBr pellets and the experimental details are described in Section 2.2.4.

5.2.3 **Cycling experiments**

Considering that the ultimate goal of this part of the research is to find cathode materials for use in lithium batteries, the electrochemical cycling performance of cathode materials is of critical importance. Electrochemical testing was carried out on a two electrode test cell with the mesophase-based composite as the cathode, Li metal foil as the anode, and a 1M solution of $LiClO_4$ in an equimolar of propylene carbonate (PC) and 1.2 dimethoxycarbonate (DMC) as the electrolyte. A Celgard 2400™ thin film was used as the separator. The composite cathode was prepared by mixing mesostructural materials (83 wt %) with 15 wt % Ketjan carbon black and 2 wt % PVDF polymer binder in ethanol solution. The dried mixture was pressed at 10 tons/inch^2 pressure into a 13 mm diameter pellet with which contains about 20 mg of the active mesophase. The cathode pellet was dried at 200 °C for two hours before the cell was assembled under an argon atmosphere in a dry box. The charge/discharge tests were performed with an EG&G Model 263 Potentiostat/Galvanostat at a constant current density. The specific experimental conditions for each sample are shown in Table V-2. The capacity was calculated from the weight of the cathode, the current, and the elapsed time of discharge.

Table V-2 Charge/discharge conditions of the mesophases

Sample #	Current density (mA/cm^2)	Potential range (V)	Active cathode (mg)	Open circuit voltage (V)
MFZ-1	0.13	2.5-3.5	6.81	2.79
MFZ-2	0.15	1.5-3.5	16.20	2.72
MFZ-3	0.13	2.5-3.5	8.17	2.68
MFZ-4	0.13	4.3-2.5	11.56	3.21
MFZ-5	0.13	3.3-2.5	12.60	2.78
MFZ-6	0.13	3.8-2.5	9.43	3.05

5.2.4 Results and Discussion

A) TEM photographs

TEM photographs of samples MFZ-1 and MFZ-2 are shown in Figs. V-1 and V-2 respectively. The manganese-substituted mesostructral silicates (MFZ-1) are characteristic of lamellar structures and the manganese oxide framework (MFZ-2) which possesses hexagonal channel arrangements. The channel dimensions are around 40 Å, which are in good agreement with the results reported by Huo *et al.* [17] and Beck *et al.* [16, 18, 20].

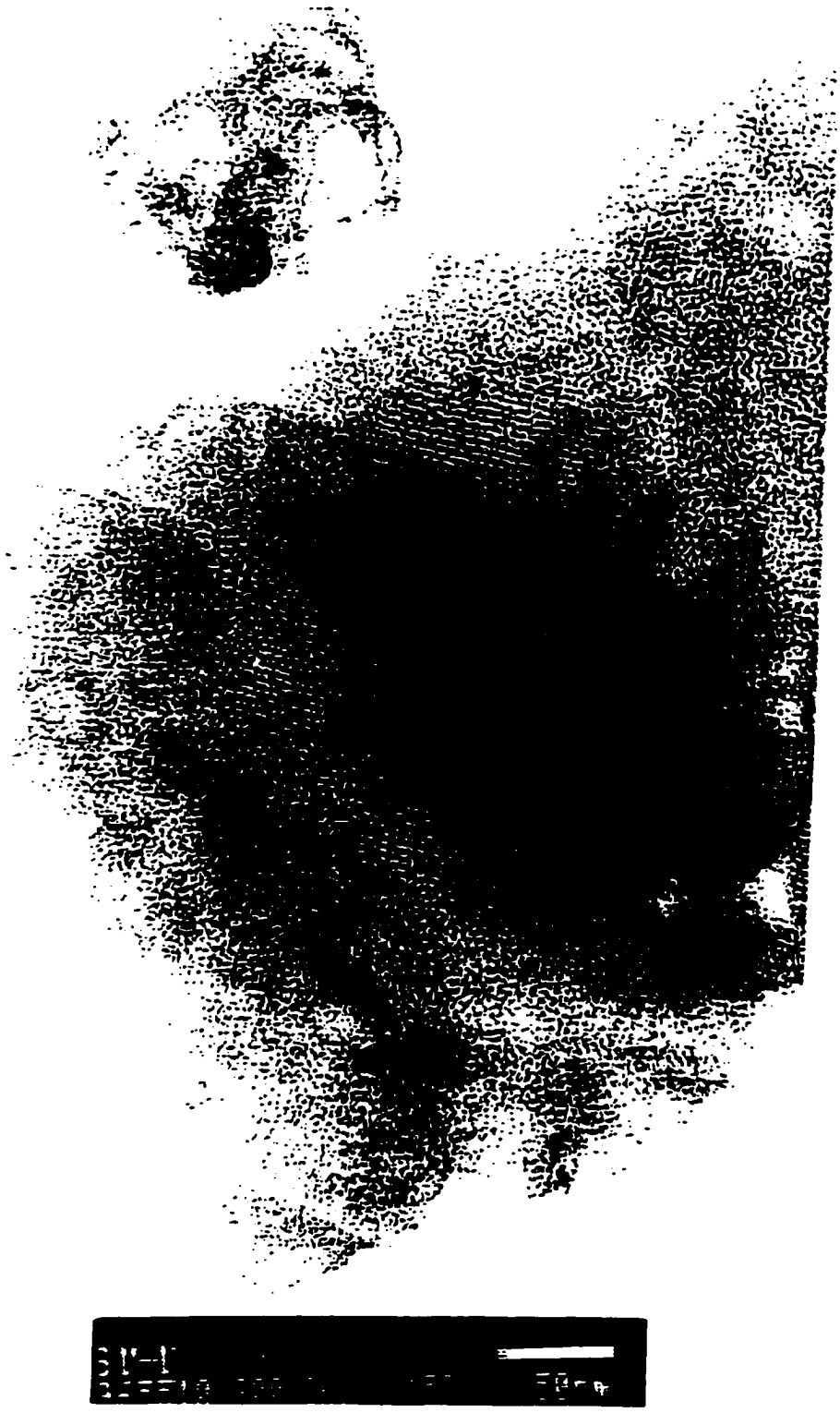

Fig. V-1A TEM image of Mn-substituted mesostructure MFZ-1. A lamellar arrangement can be seen with a pore size 4.1 nm.

Fig V-1B Another view of the lamellar arrangement.

Fig. V-2 TEM image of manganese oxide framework MFZ-2. A hexagonal pore structure can be seen with a dimension of 3.9 nm.

B) IR spectra

Fig. V-3 shows the IR spectra of the surfactant CTAB, MFZ-1, and calcined MFZ-1. The IR spectrum (curve A) of CTAB molecule shows three major absorption regions, 2850-3020 cm^{-1}, 1460-1490 cm^{-1}, and 800-1100 cm^{-1}. The vibrations around the 3000 cm^{-1} can be contributed to the N-H or C-H stretching vibrations. The bands in the range 1460-1490 cm^{-1} are assigned as HNH bending and the vibrations below 1100 cm^{-1} may be attributed to the long carbon chain of the surfactant.

The IR spectrum (curve B) of the as-synthesized MFZ-1 shows that the CTAB molecules are entrapped in the inorganic frameworks. The basic vibrational bands of CTAB appear in the spectrum of MFZ-1, with the exception of loss of some fine structure. The strong bands at 1009 and 441 cm^{-1} are attributed to Si-O stretching and O-Si-O bending, respectively. The weak bands between the 441 and 1009 cm^{-1} may be assigned to the vibrations of the silicate framework or the manganese species. The broad band at 3446 cm^{-1} originates in the OH groups from the hydrothermal reactions.

The curve C in Fig. V-3 is the spectrum of the calcined MFZ-1 sample. The bands of the CTAB molecule are hardly seen in the calcined form. The bands at 1009 and 441 cm^{-1} are shifted to higher positions, indicating that removal of the templating molecules leads to a morphological change in the wall upon calcination. The differences between

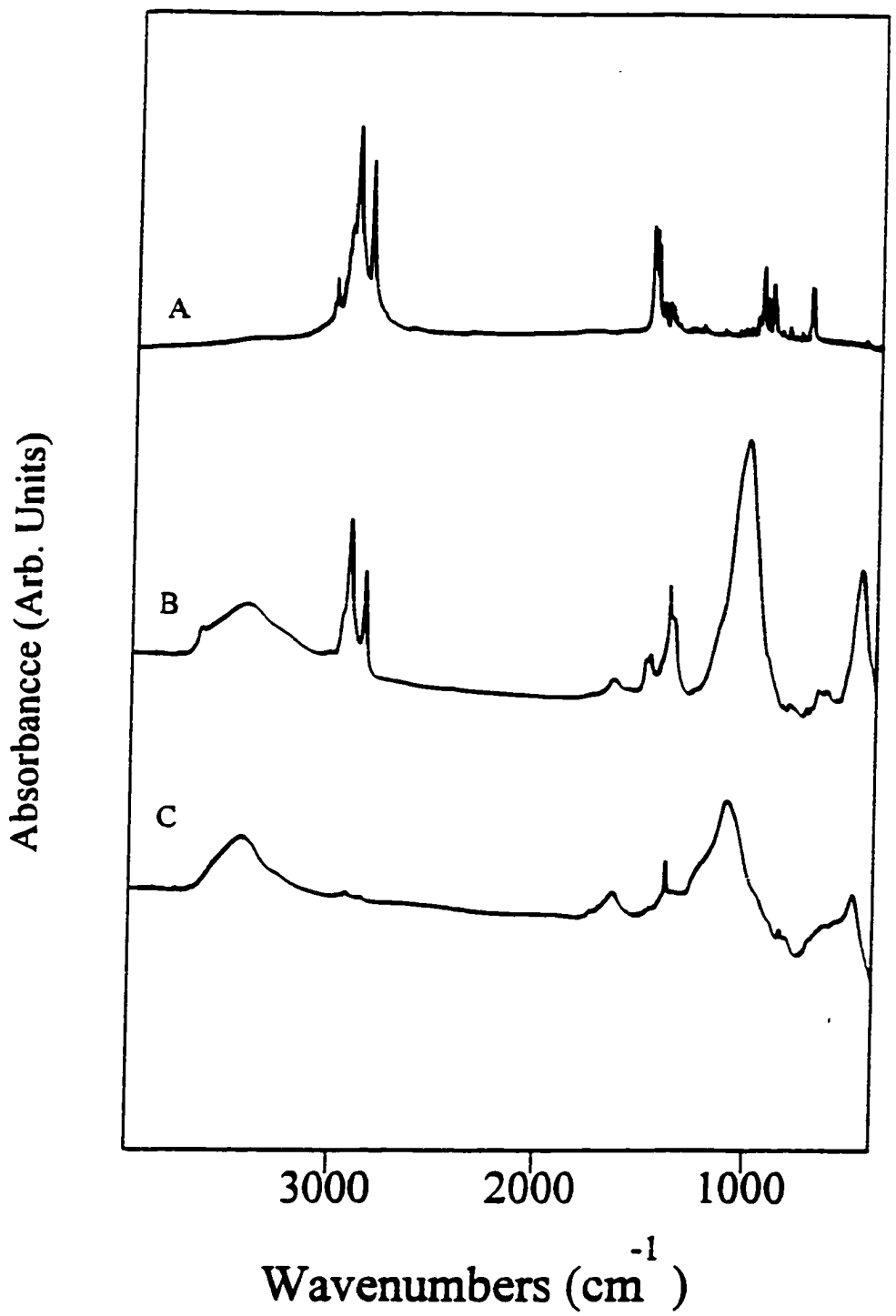

Fig. V-3 IR spectra of CTAB (A), MFZ-1 (B), and calcined MFZ-1 (C)

curve B and C are related to the structural changes of the wall induced by the calcination reaction. The vibrations of the OH groups remain notable even after heat treatment.

C) Discharge behavior

The discharge curves of the mesostructrual materials are reported in Fig. V-4 through Fig. V-9. The discharge experiments were carried out using the galvanostatic method with a constant current. The potential of the cell was recorded as a function of time. The cathode capacity was calculated as following:

Specific capacity (mAh/g)= (current (mA)* time (hour))/weight of active cathode (g)

Sample calculation for MFZ-1:

Potential range: 2.5<V<3.5

Current value: C=100 μA=0.1 mA

Time elapsed: t=30,265 seconds=8.4 hours

Capacity = C * t =0.1 mA * 8.4 hours = 0.84 mAh

Weight of the composite cathode: 8.2 mg

Active mesophase: 8.2 * 83% = 0.681 mg

Specific capacity of MFZ-1 = $0.84/0.681 \times 10^{-3}$ = 123.4 mAh/g

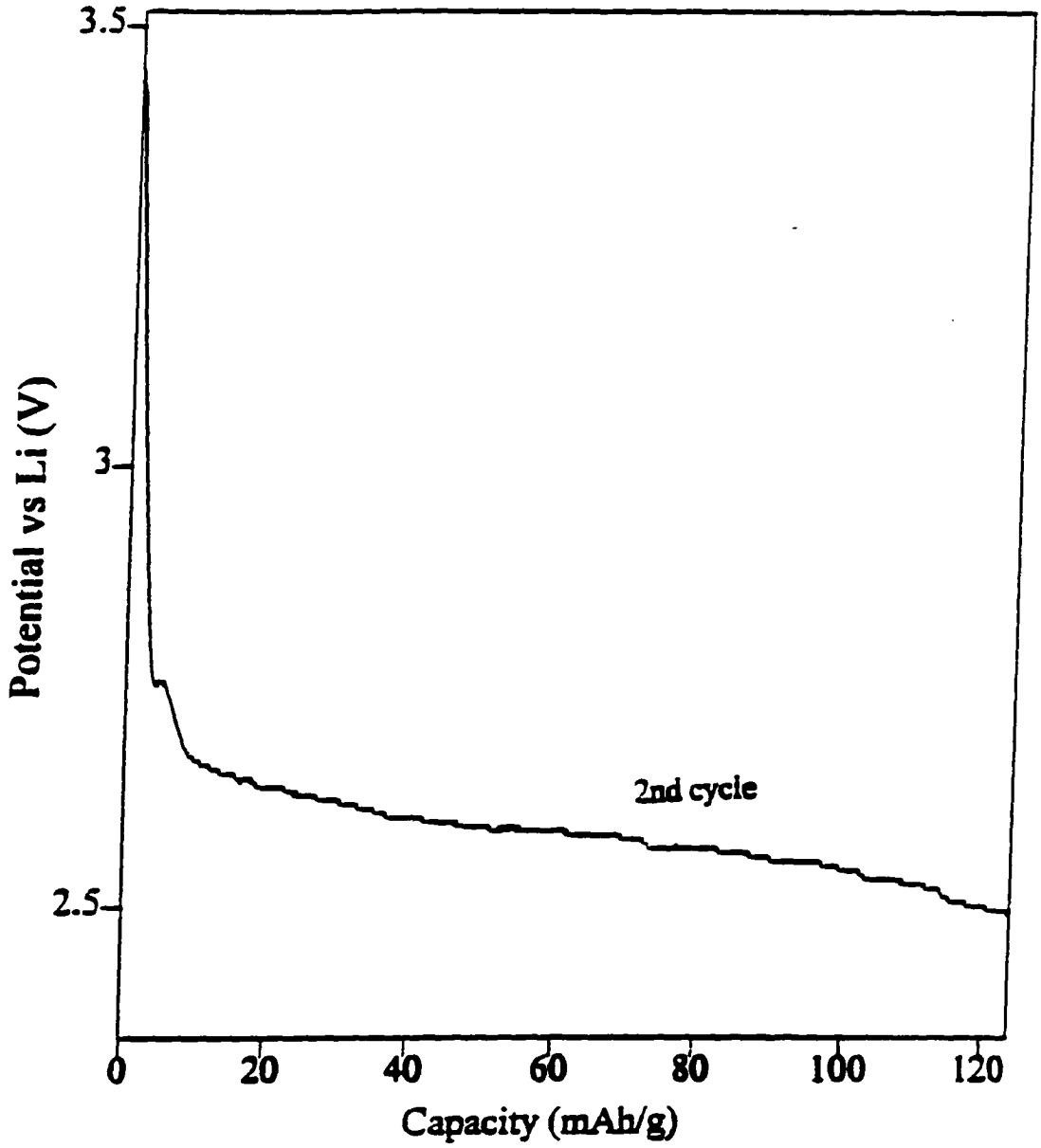

Fig. V-4 Discharge curve of MFZ-1 during the second cycle

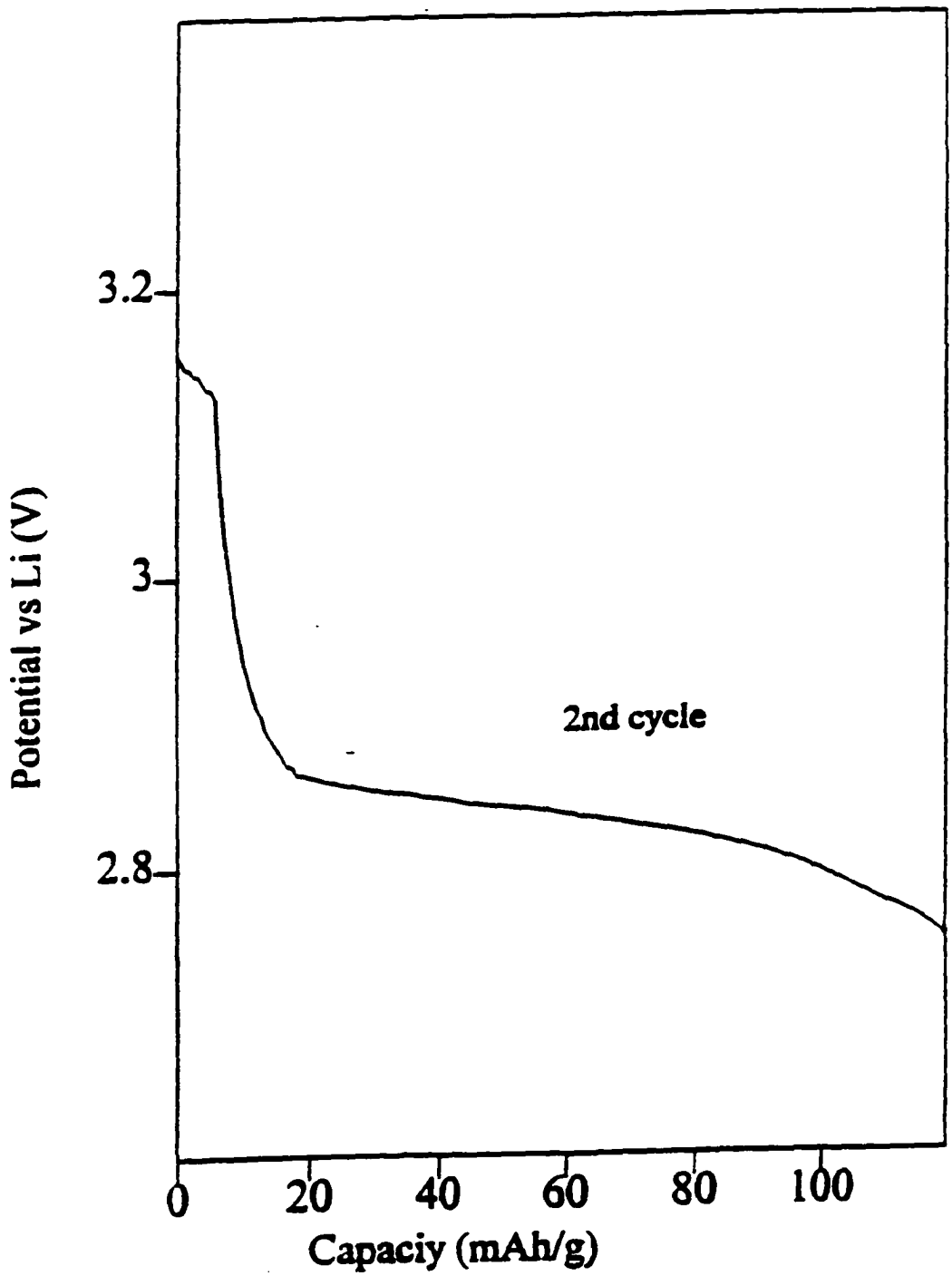

Fig. V-5 Discharge curve of MFZ-2 during the second cycle

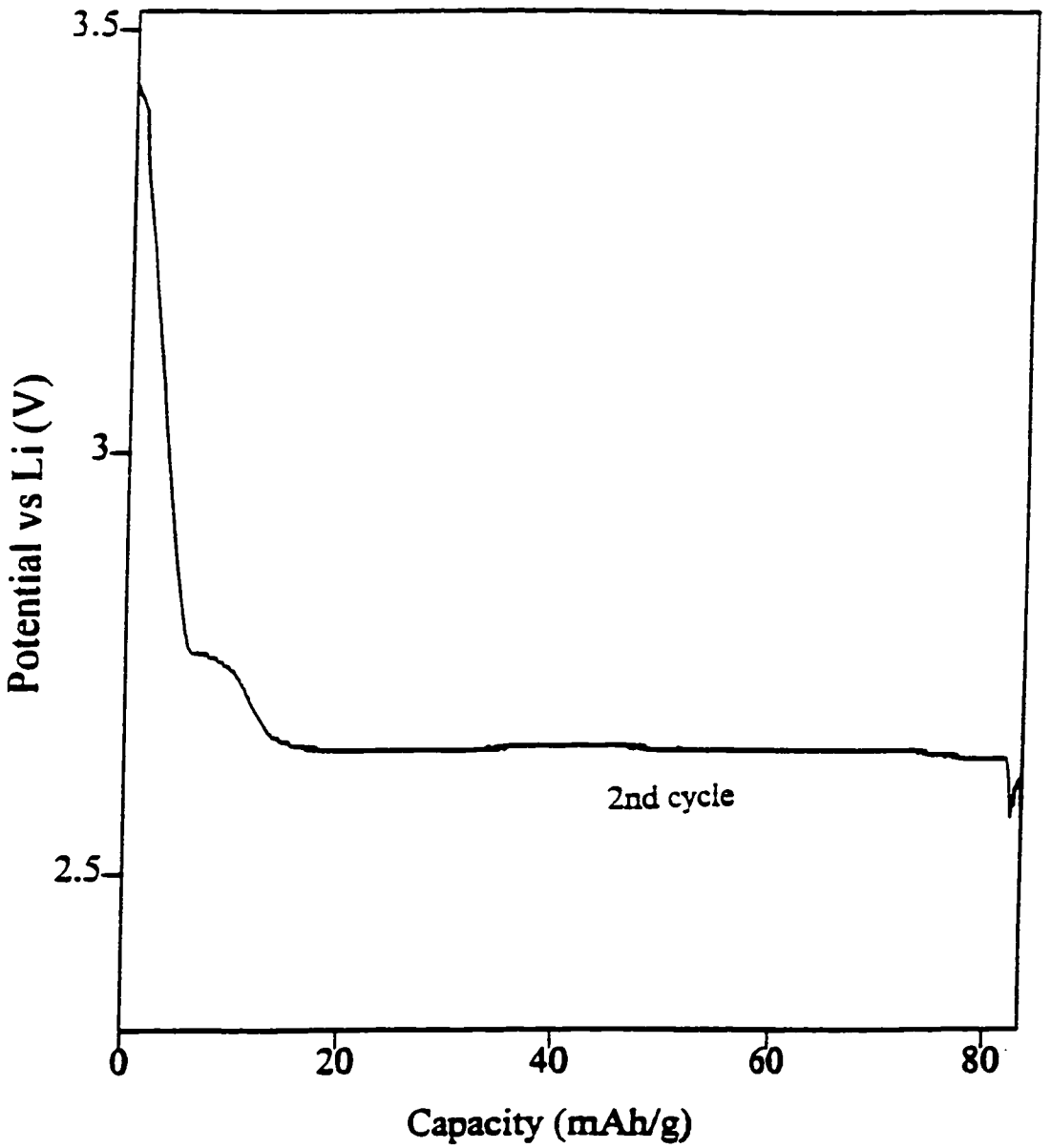

Fig. V-6 Discharge curve of MFZ-3 during the second cycle

The discharge curves were plotted with potential (E) versus cathode capacity. The capacities of the above mesostructrual materials are reported in Table V-3.

Table V-3 Capacities of the mesostructrual cathodes

Cathode #	Current (mA)	Time	Cathode wt. (mg)	Capacity
MFZ-1	0.10	8.40	6.81	124.0
MFZ-2	0.12	13.66	16.20	101.20
MFZ-3	0.10	6.80	8.17	83.14
MFZ-4	0.10	12.54	11.56	108.51
MFZ-5	0.10	12.50	12.60	99.56
MFZ-6	0.10	9.80	9.43	103.60

D) Discussion

The manganese oxide-based mesostructures have a potential plateau around 2.6 volts with a capacity from 83 to 124 mAh/g (Table V-3). Sample MFZ-1 provides a relatively high capacity of 124 mAh/g. What is more interesting is that the discharge curve of MFZ-1 has a single flat plateau between 2.5 to 2.7 V as shown in Fig. V-4. Conventional insertion materials such as $Li_{1-x}CoO_2$ and $Li_xMn_2O_4$ provide theoretical capacities 274 and 188 mAh/g, respectively. However the cathode materials undergo

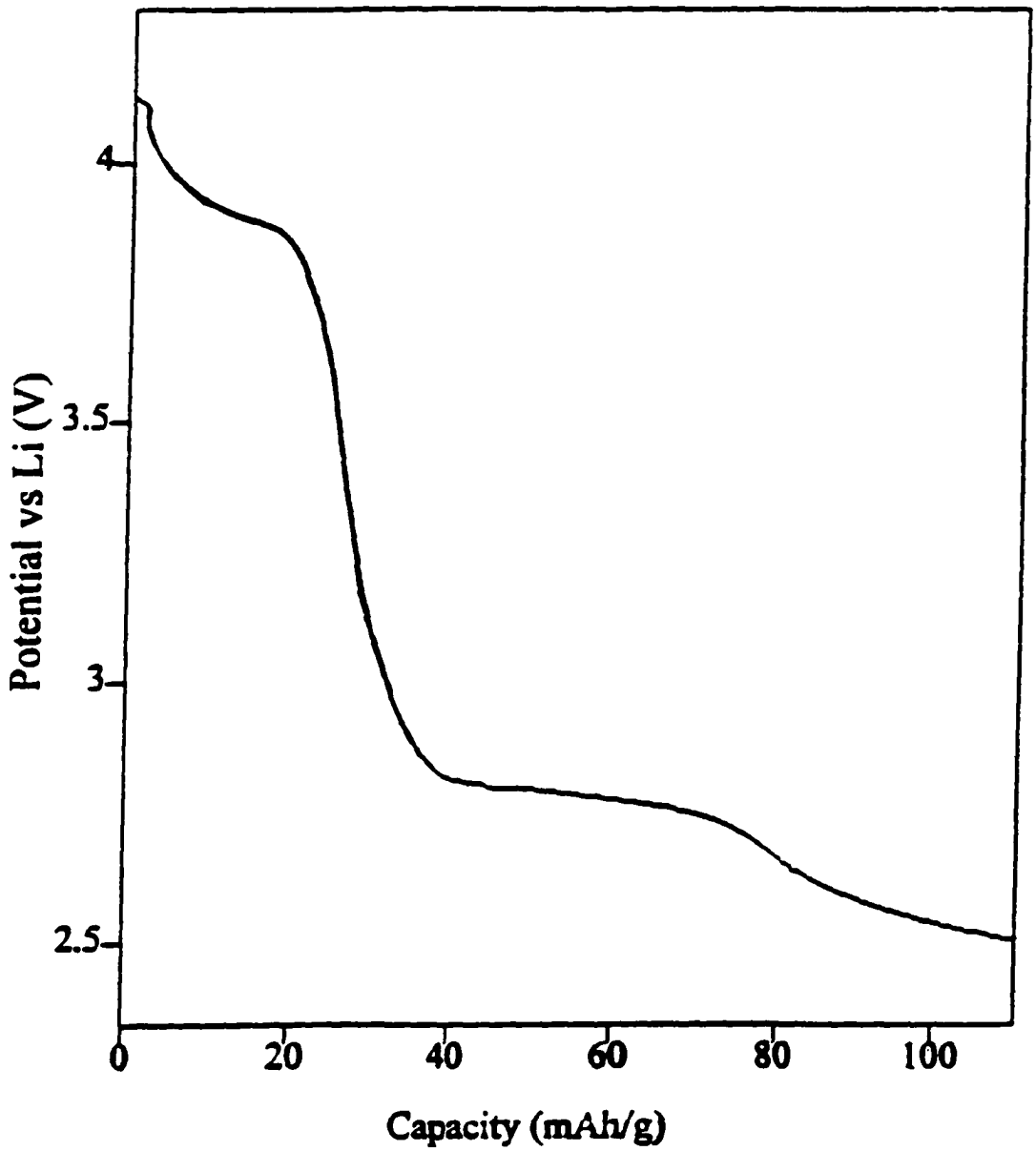

Fig. V-7 Discharge curve of MFZ-4 during the second cycle

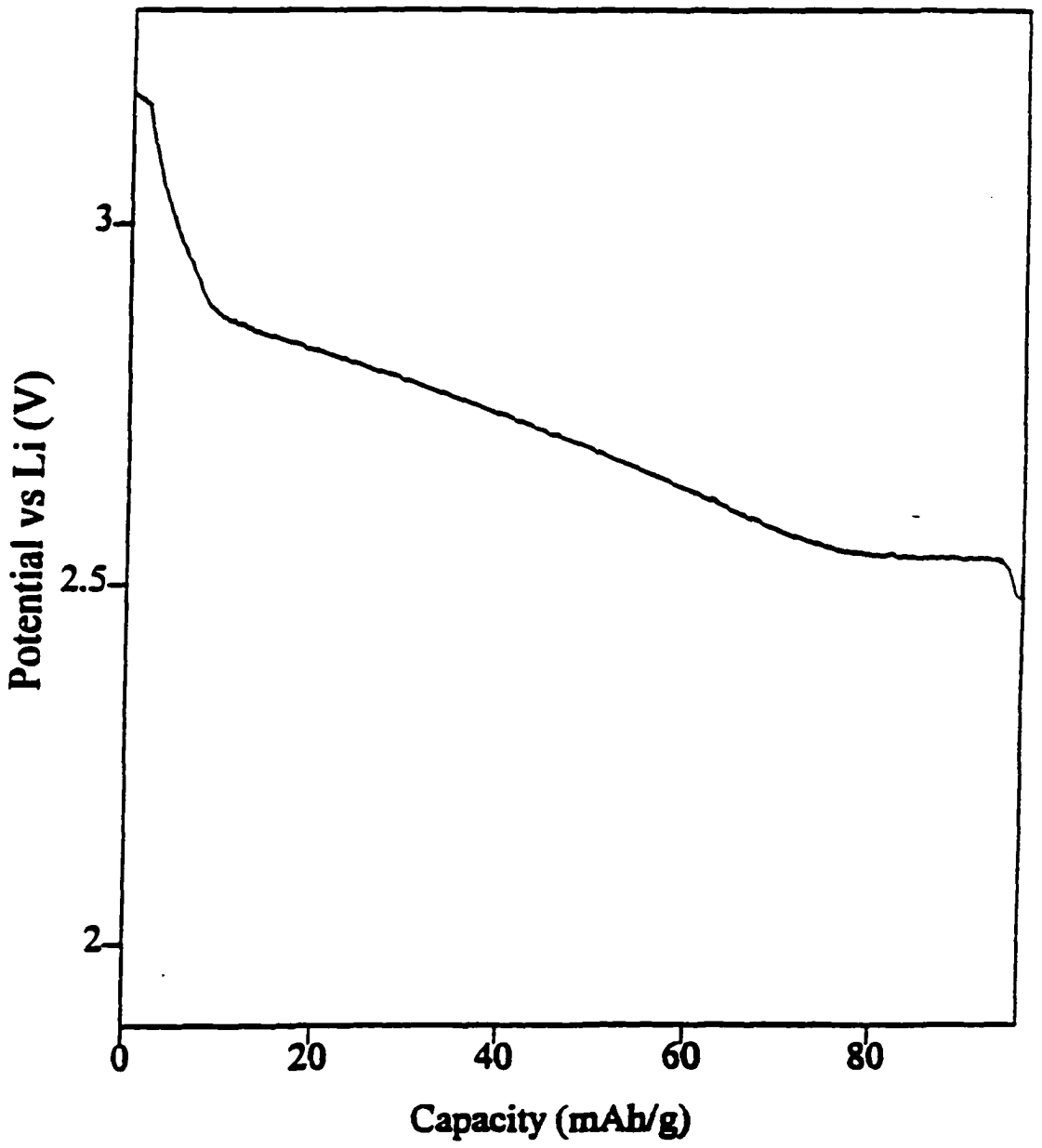

Fig. V-8 Discharge curve of MFZ-5 during the second cycle

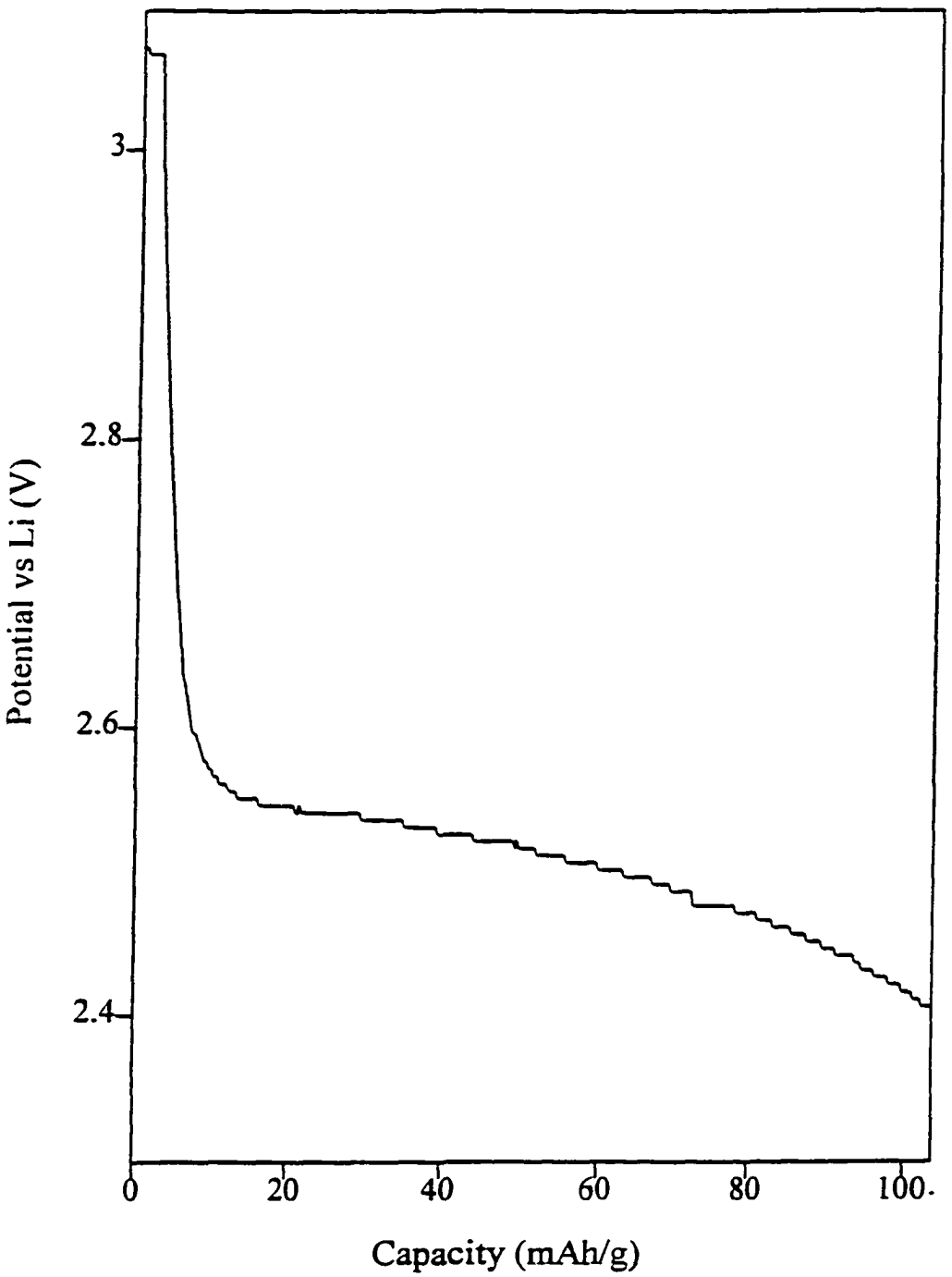

Fig. V-9 Discharge curve of MFZ-6 during the second cycle

phase transitions as indicated by several potential plateaus during a deep discharge process. For example, there is a sudden potential drop from 4 V to 3 V in spinel $Li_xMn_2O_4$ cathode at x = 1. Phase transitions were also observed for the $Li_{1-x}CoO_2$ cathode for x > 0.75 [28].

The sharp potential drops such as these must be avoided in an operating battery. Consequently the practical capacity of a cathode material is limited by a single plateau. For example, $Li_xMn_2O_4$ has a 4V plateau and a 3V plateau. The capacity of $Li_xMn_2O_4$ in a 4V battery is about 95 mAh/g and 93 mAh/g in a 3V cell. The practical capacity of $Li_{1-x}CoO_2$ in the Sony lithium ion battery is about 98 mAh/g (x = 0 to 0.7). Therefore the practical capacity of the manganese oxide-based mesostructural materials are better than those of the conventional intercalation cathodes.

5.3 Tin Oxide-Based Mesostructual Material as Anodes

Numerous carbonaceous materials which undergo reversible intercalation/deintercalation processes have been investigated for use in the anodes of rechargeable lithium-ion batteries during the past several years [29-42]. For example, well-crystallized graphite appears to be the most attractive carbon anode because its high capacity (e. g. one mole of lithium can be intercalated by six moles of carbon) and low electrode potential (0.01-0.2 vs Li). It has been observed that the electrochemical behavior of the carbon anodes depends not only on the type of carbon materials but also the solvent of the

electrolyte system used in batteries. Nonaqueous solvents such as ethylene carbonate (EC)/propylene carbonate (PC) and EC/dimethyl carbonate (DMC) have been successfully used as the electrolyte. Moreover, graphite shows negligible reversible but large irreversible capacity when PC or tetrohydrofuran (THF) is used as the major solvent of a electrolyte solution [43]. The irreversible capacity loss of the graphite anode has been attributed to the reduction of PC or THF on the graphite surface during the first Li-intercalation process [31, 39]. Fauteux and Koksbang [44] gave a review of anode materials for lithium batteries.

Transition metal oxides, such as $LiFeO_2$ [45], $Li_6Fe_2O_3$ [46], and $LiWO_2$ [47], alloys such as LiAl, LiSi, and $Li_{4.4}Sn$ [48], and conducting polymers [49] have been studied for potential use in anodes of lithium batteries. Recently tin oxide and tin-substituted compounds were also reported for the use in the anodes of lithium rechargeable batteries. Lithium tin oxide has tremendous electrochemical capacity (up to 10 mole Li per mole of tin oxide) [50, 51]. Bagshaw *et al.* [27] prepared tin oxide mesostructrual materials using a PEO-based surfactant under hydrothermal conditions, however his work has focused on the catalytic properties of this material. In this part, the preliminary results of tin-based mesostructrual materials utilized as intercalation anodes are reported.

5.3.1 Sol-gel preparation of tin oxide

Tin (IV) acetate was added to a 2M LiOH solution with the Li : Sn ratio 2 : 1, and the suspension was agitated at 70 °C overnight. The precipitate was filtered, washed with distilled water and dried in a vacuum oven at 110 °C until its weight did not change with further drying. The final product was obtained upon heating the dried product at 400 °C for four hours.

5.3.2 Hydrothermal preparation of mesostructrual tin oxides

Tin oxide mesostructures and tin-substituted silicates were prepared using CTAB or nonionic PEO-surfactants as templates. The gel compositions of the reactants and reaction conditions are summarized in Table V-4.

Table V-4. Gel compositions and reaction conditions

Samples	SiO_2	SnO_2	Li_2O	Templates	H_2O	Synthesis condn.
Tin-1	--	1.00	1.00	0.15 PEO	120.00	160 °C 48 hours
Tin-2	--	1.00	1.00	0.30 CTAB	120.00	175 °C 24 hours
Tin-3	1.00	1.00	1.00	0.30 CTAB	240.00	135 °C 24 hours
Tin-4	1.00	1.00	1.00	0.30 CTAB	240.00	135 °C 24 hours

The synthesis procedures of tin oxide compounds are similar to those of the manganese oxide mesostructures. $SnCl_4$ was the source of SnO_2 and $LiOH{\cdot}H_2O$ was added as the Li_2O species. Tetramethyl orthosilicate and tetraethyl orthosilicate were used in Tin-3 and Tin-4, respectively, as the silicate sources. The tin-containing gels were agitated and then placed in a Parr pressure reactor for hydrothermal treatment. The final products were calcined at about 500 °C before electrochemical characterization.

5.3.3 Electrochemical experiments

Although the tin oxide mesostructural materials are being developed as anode materials, their electrochemical performance was assessed in a cell in which they functioned as a cathode against metallic lithium as an anode. This is the standard practice in the battery research field.

The cycling experiments were performed in a two-electrode cell

metallic lithium foil | Li^+ electrolyte | Tin composite cathode

with the following composition:

Tin composite cathode: 83 wt % of tin-based mesostructures

15 wt % Katjen carbon black

2 wt % PVDF binder

Li^+ electrolyte: 1 M $LiClO_4$ in a 1:1 mol PC/DMC solution

Metallic lithium anode: lithium foil with 2 mm thick

The charge/discharge experiments were performed galvanostatically with a constant current density at room temperature. The potential change of the cell was recorded as a function of time.

5.3.4 Cycling results and discussion

The discharge curves of tin oxide and the tin-based mesostructures are shown in Fig. V-10 through Fig. V-14. Their capacities are summarized in Table V-5.

Table V-5. Capacities of the tin oxide-based anodes

Sample #	Current (mA)	Active anode (mg)	Elepsed time (hour)	Capacity (mAh/g)
tin oxide (sol-gel)	0.10	15.50	19.84	128.00
Tin-1	0.15	15.75	18.12	172.60
Tin-2	0.10	9.67	16.30	169.00
Tin-3	0.10	6.89	11.16	162.40
Tin-4	0.10	17.50	30.27	173.50

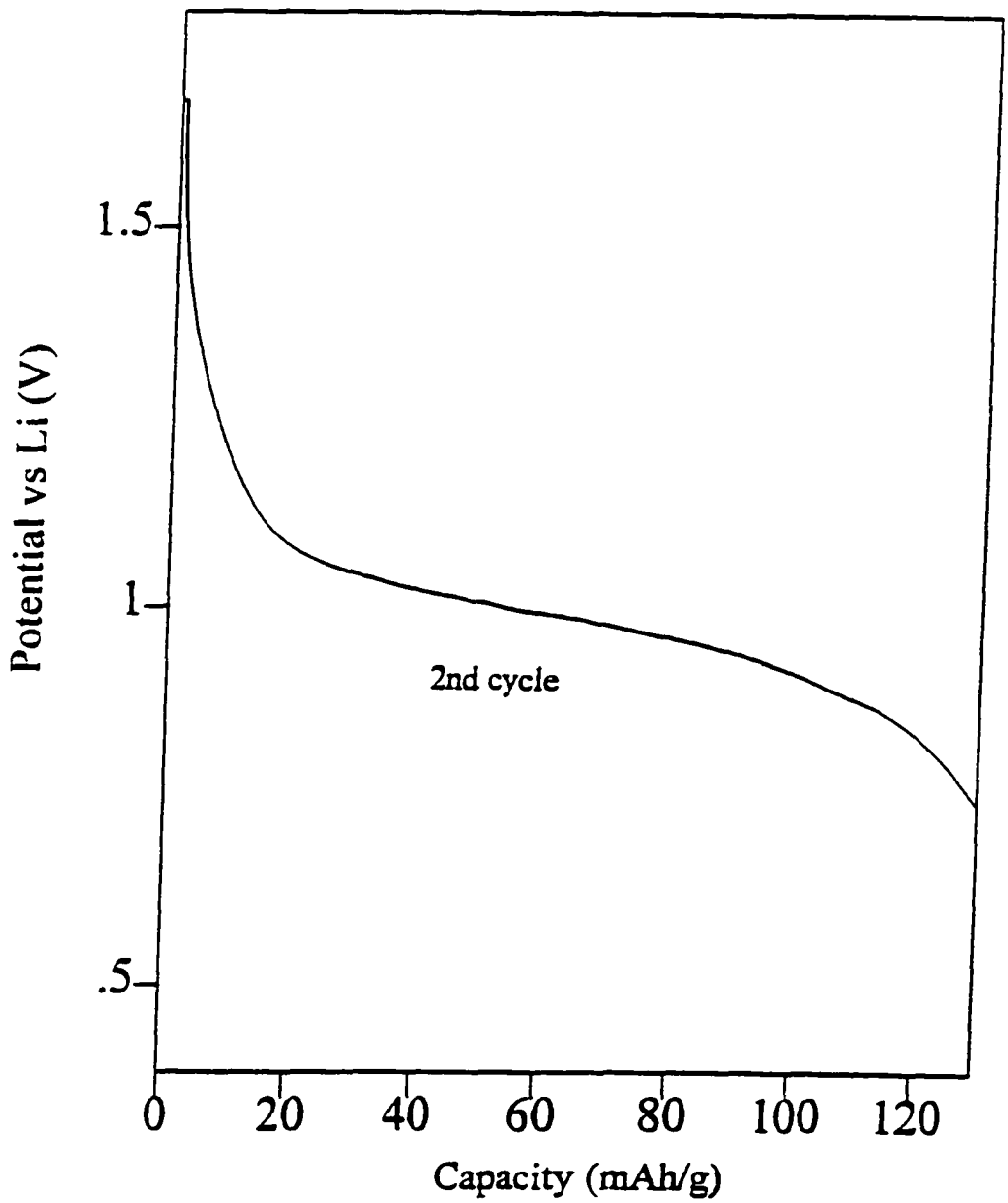

Fig. V-10 Discharge curve of tin oxide composite anode from sol-gel reaction during the second cycle

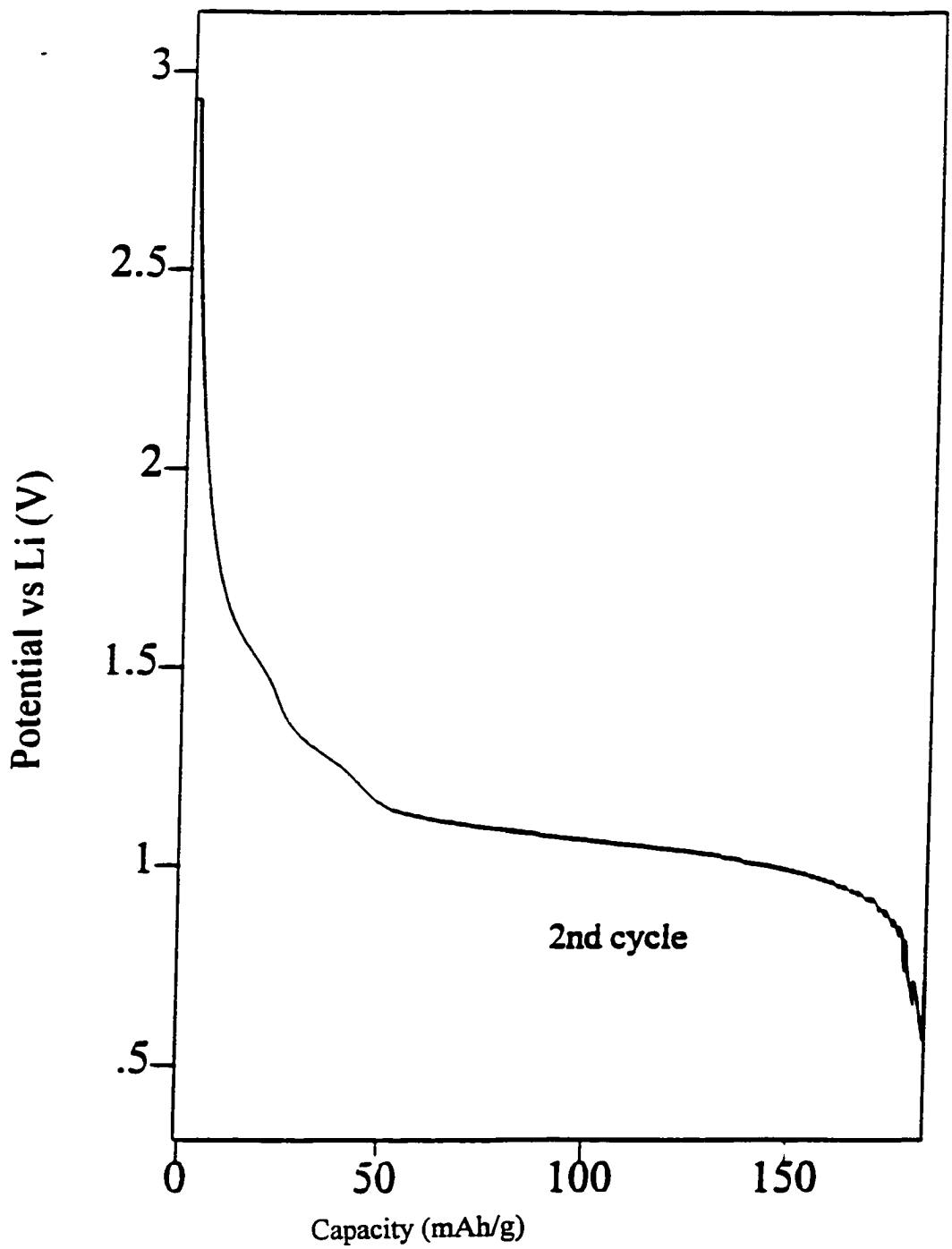

Fig. V-11 Discharge curve of tin oxide framework, sample Tin-1 during the second cycle.

Tin oxide-based mesophases (except sample Tin-2) have a potential plateau around one volt with a capacity above 160 mAh/g (Table V-5). The mesostructural materials have a higher capacity than the amorphous tin oxide from sol-gel synthesis (128 mAh/g). Several anode candidates for lithium rechargeable batteries are listed in Table I-2. However most of the listed materials are not suitable for practical applications due to the poor safety considerations (metallic lithium), irreversible insertion reactions (LiAl, $Li_{4.4}Si$ and $Li_6Fe_2O_3$), too high anode voltage ($LiMoO_2$ and $Li_7Ti_5O_{12}$) and physical or chemical stability (polymer anode materials). As a result, intercalation carbon materials are currently the only practical choice as anodes for lithium rechargeable batteries.

Although well-crystalized graphite has a density of 2.2 g/cm^3, the density of amorphous carbon powders is well below 1.0 g/cm^3. A lithium ion battery using a carbon anode usually has a low volumetric energy density. Furthermore, carbon anodes may react with organic solvents such as PC and THF to form electrochemically inactive phases, which will further reduce the energy density and battery life. Tin oxide-based anodes appear to be a promising candidate for use in the lithium rechargeable battery [52, 53]. Indeed tin oxide-based mesostructural materials may become critically important as anode materials in the development of high energy density batteries.

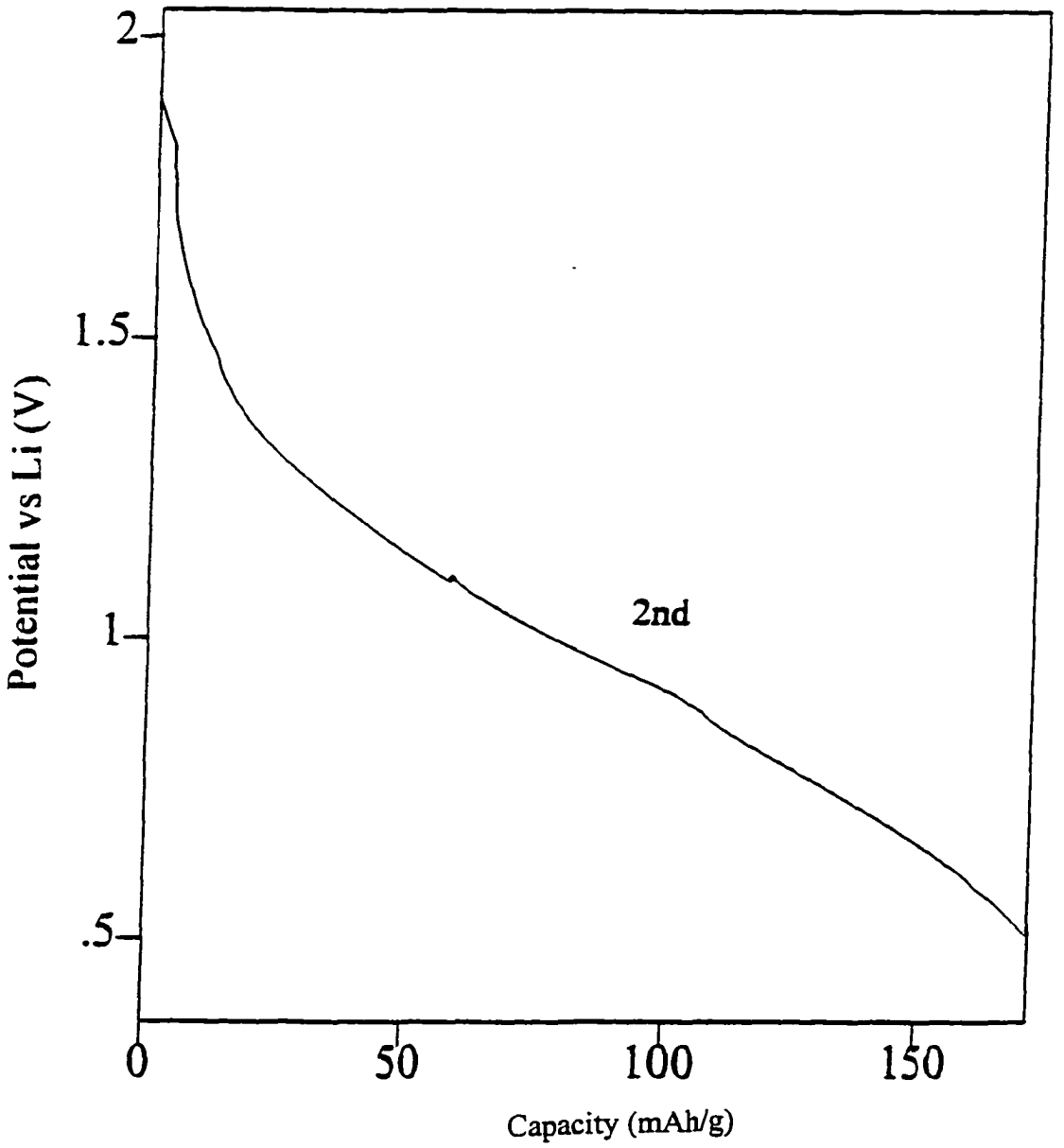

Fig. V-12 Discharge curve of tin oxide framework Tin-2 during the second cycle

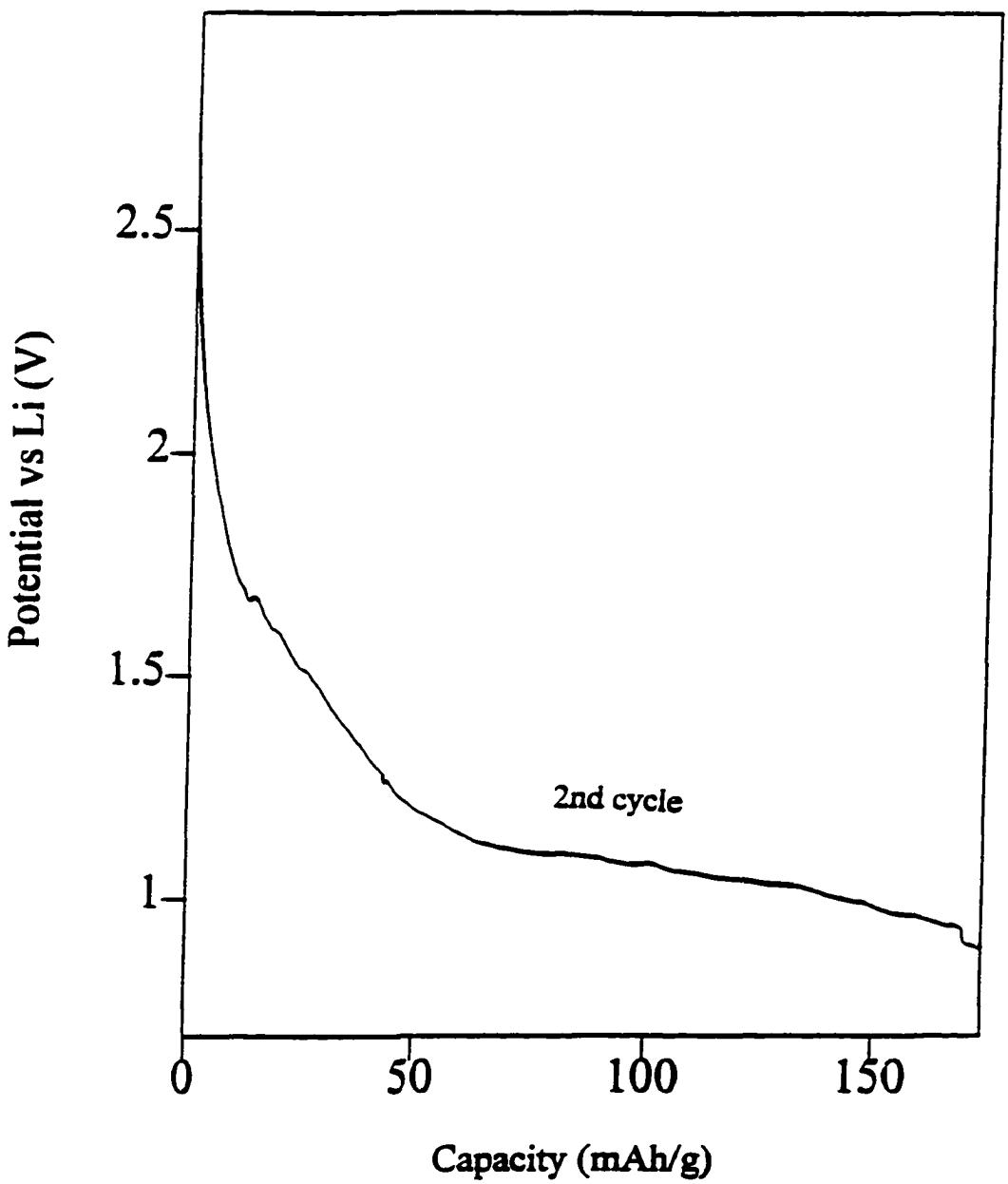

Fig. V-13 Discharge curve of Sn-substituted mesosilicate Tin-3 during the second cycle

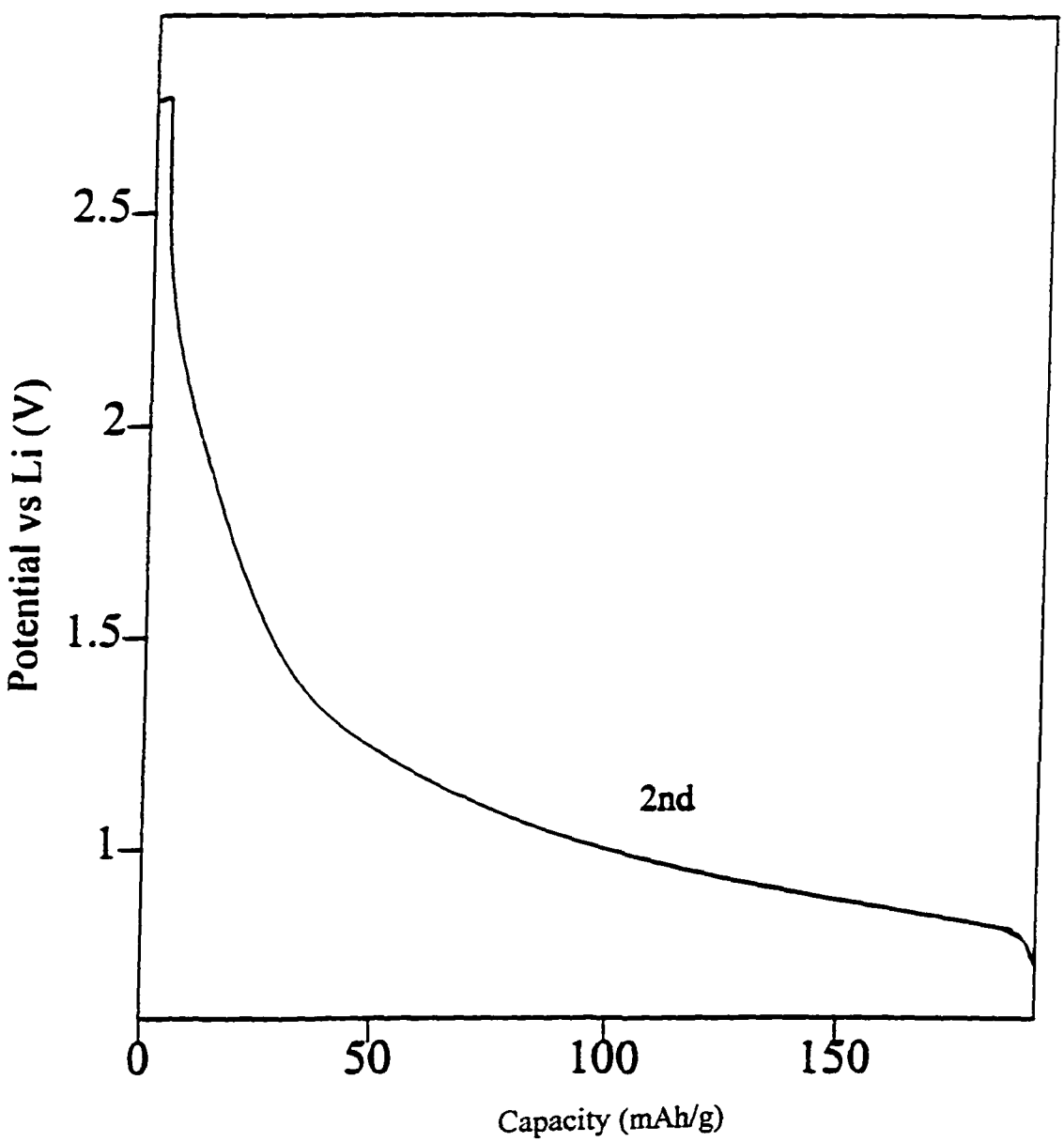

Fig. V-14 Discharge curve of Sn-substituted mesosilicate Tin-4 during the second cycle

5.4 Summary

Mesoporous materials have been extensively explored as heterogeneous catalysts since 1992 [16, 19, 22, 23, 27, 54]. However their use as electrode materials has not been reported. The preliminary results of the cycling experiments indicate that the new mesostructural materials may find important applications in lithium rechargeable batteries.

The existence of the mesochannels presents a novel and unique way to enhance the discharge capacity and reversibility of lithium rechargeable batteries. As mentioned before, lithium intercalation into traditional intercalation compounds usually causes structural modifications, as illustrated in the following examples. An expansion of layer spacing was observed in layered compounds such as graphite and $Li_xV_2O_5$ upon insertion of lithium ions. In a well-ordered graphite crystal the interlayer spacing increases by about 10% during Li intercalation to form C_6Li [55]. A similar interlayer expansion was reported in the $Li_xV_3O_8$ cathode [56]. Lithium intercalation into Li_xCoO_2 leads to a lattice distortion from hexagonal to monoclinical symmetry and a strong first order transition was also observed in the region at $0.75<x<0.93$ [28]. A Jahn-Teller distortion occurs in spinel $Li_xMn_2O_4$ at $x=1$ where lithium ions begin to occupy the tetrahedral sites between the Mn-O layers [28]. These structural modifications are related to both electronic and geometrical requirements for the inserted Li ions. The discharge capacity of an intercalation compound is determined by the amount of lithium

ions which can be inserted into the host without significant structural changes. Graphite materials have larger interlayer spacing (3.5 Å) than transition metal oxides (around 2.5 Å). Therefore graphite has much higher theoretical discharge capacity compared to transition metal oxide compounds (372 mAh/g to about 200 mAh/g).

One important issue which needs to be explored is how the lithium ions coordinate with the transition metal species inside the mesopores. Sato *et al.* [57] recently reported that highly disordered graphite can take one mole of Li per two moles of C (C_2Li) with a specific discharge capacity of 680 mAh/g. This extra specific capacity is attributed to the formation of Li_2 molecules between the carbon layers. The capacity has no limit imposed by the electronic balance requirement because the insertion of lithium ions involves little change in the electronic state of the host; consequently the capacity increase is limited only by steric and geometrical considerations. A similar conclusion may be applied to the mesostructural materials in lithium intercalation processes. Mesostructural materials have open channels with pore sizes in a range from 20 to 100 Å, and it is this unique structural property which provides an ideal system for the lithium intercalation. Lithium intercalation in a mesochannel and in a layered compound is schematically shown in Fig. V-15. The open channel system can accommodate more lithium ions and enhance lithium ion transport during the charge/discharge processes.

The coordination environments of transition metal ions in the mesostructures are not understood at present time. The transition metal oxide polyhedra may either attach to

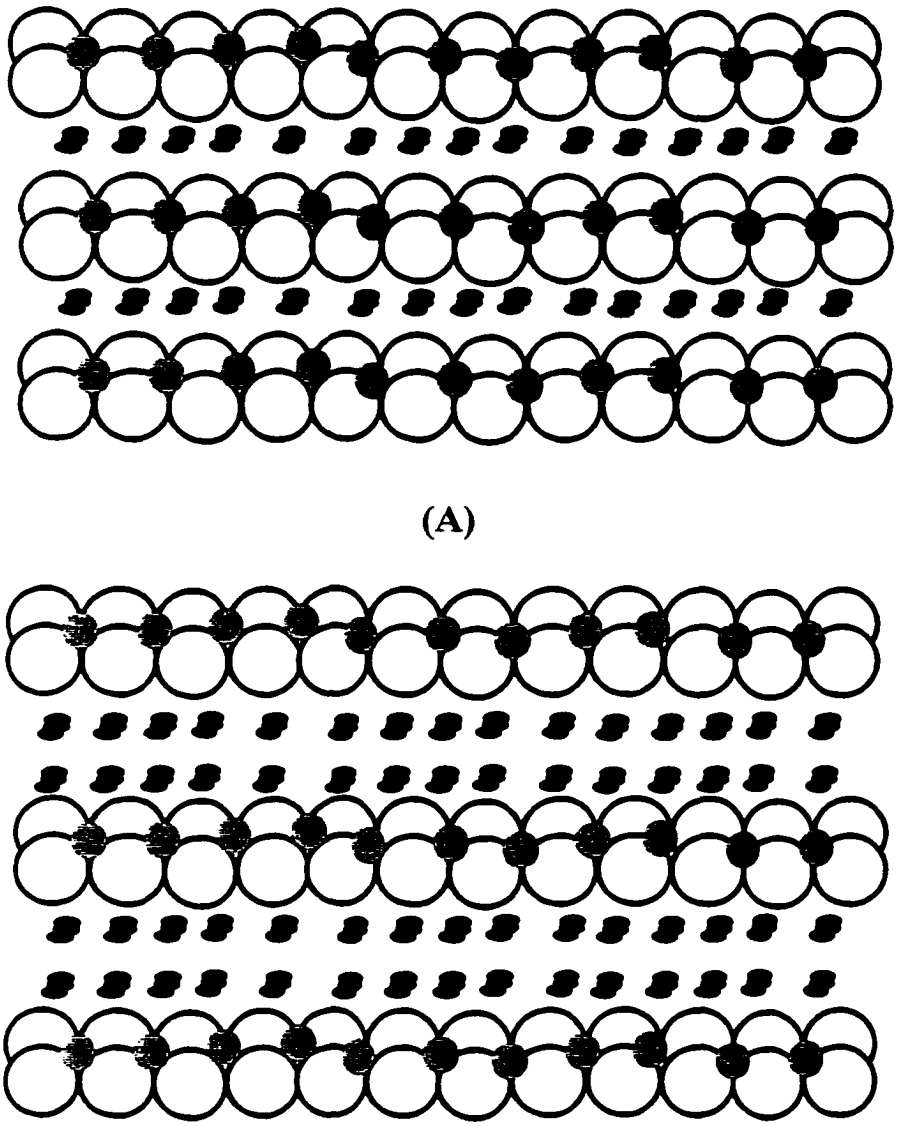

Fig. V-15 Schematical representation of lithium ions in: (A) regular insertion compounds and (B) mesostructural materials

the silicate wall or incorporate into the silicate framework. According to Morey *et al.* [26], the substituting atoms (V, Ti, Mn, etc) are most likely incorporated into the wall. For heterogeneous catalytic applications, mesostructural materials are designed to have rigidly crystalline walls with isolated, active catalytic sites. In contrast, a high content of transition metal atoms will decrease the crystallinity of the wall, which may facilitate lithium diffusion in battery applications. Furthermore a high concentration of transition metal ions in the wall can increase the discharge specific capacity. To this end, a consistent effort was made to synthesize mesostructural materials with a high content of transition metal oxide species.

The cathode capacity shown on the first cycle is about 30% higher than that on the second cycle for the most mesostructural materials (data not shown). The capacity loss is attributed to the presence of OH groups in the samples obtained from hydrothermal reactions. These OH groups can exist even after heat treatment at 500 °C (see Fig. V-3). Lithium ions may be trapped by the OH groups and contribute to the irreversibility in the subsequent charge process. Kanno *et al.* [45] and Chirayil [13] also reported the existence of hydroxyl groups in cathode materials prepared from hydrothermal reactions.

These preliminary results show that mesostructural materials from templating syntheses are electrochemically active and may find important applications in lithium rechargeable batteries. The unique structural properties of the mesostructual materials are ideal for

cathodes and anodes undergoing intercalation/deintercalation reactions. Much research work needs to be done in the future, including:

1) Optimization of synthesis conditions

2) New precursors for pure transition metal oxide mesostructural materials

3) Structural characterization

4) Elucidation of the mechanism of lithium intercalation

5) Detailed studies of electrochemical properties

References:

1. Chirayil, T., Zavalij, P., and Whittingham, M.S., *Solid State ionics*, **84** 163 (1996).
2. Liu, W., Farrington, G.C., Chaput, F., and Dunn, B., *J. Electrochem. Soc.*, **143** 879 (1996).
3. Gao, Y. and Dahn, J.R., *J. Electrochem. Soc.*, **143** 1783 (1996).
4. Pistoia, G., Pasquali, M., Wang, G., and Li, L., *J. Electrochem. Soc.*, **137** 2365 (1990).
5. Barboux, P., Tarascon, J.M., and Shokoohi, F.K., *J. Solid State Chem.*, **94** 185 (1991).
6. Zhecheva, E., Stoyanova, R., Gonova, M., Alcantara, R., Morales, J., and Tirado, J.L., *Chem. Mater.*, **8** 1429 (1996).
7. Liu, Y.J., DeGroot, D.C., Schindler, J.L., Kannewurf, C.R., and Kanatzidis, M.G., *Chem. Mater.*, **3** 992 (1991).
8. Costa, J.L., Morales, E., Paleo, M., and Jurado, J.R., *Eur. Polym. J.*, **32** 13 (1996).
9. Manev, V., Momchilov, A., Nassalevska, A., Pistoia, G., and Pasquuali, M., *J. Power Sources*, **54** 501 (1995).
10. Leroux, F., Koene, B.E., and Nazar, L.F., *J. Electrochem. Soc.*, **143** L181 (1996).
11. Nanjundaswamy, K.S., Padhi, A.K., Goodenough, J.B., Okada, S., Ohtsuka, H., Arai, A., *Solid State ionics*, **92** 1 (1996).

12. Davis, M.E. and Lobo, R.F., *Chem. Mater.*, **4** 756 (1992).

13. Chirayil, T.A., Zavalij, P., and Whittingham, M.S., *J. Electrochem. Soc.*, **143** L193 (1996).

14. Chen, R., Chirayil, T., Zavalij, P., and Whittingham, M.S., *Solid State Ionics*, **86-88** 1 (1996).

15. Soghomonian, V., Chen, Q., Haushalter, R.C., Zubieta, J., O'Conner, C.J., and Lee, Y., *Chem. Mater.*, **5** 1690 (1993).

16. Beck, J.S., Vartuli, J.C., Roth, W.J., Leonowicz, M.E., Kresge, C.T., Schmitt, K.D., *J. Am. Chem. Soc.*, **114** 10834 (1992).

17. Huo, Q., Margolese, D.I., and Stucky, G.D., *Chem. Mater.*, **8** 1147 (1996).

18. Beck, J.S. and Vartuli, J.C., *Current Opinion in Solid State and Materials Science*, **1** 76 (1996).

19. Cheng, C.F., Zhou, W., and Gladden, L.F., *J. Chem. Soc., Faraday Trans.*, **93** 359 (1997).

20. Beck, J.S., Vartuli, J.C., Kennedy, G.J., Kresge, C.T., Roth, W.J., and Schramm, S.E., *Chem. Mater.*, **6** 1816 (1994).

21. Reddy, K.M., Moudrakovski, I., and Sayari, A., *J. Chem. Soc., Chem. Commun.*, 1059 (1994).

22. Park, D.H., Cheng, C.F., He, H., and Klinowski, J., *J. Mater. Chem.*, **7** 159 (1997).

23. Zhao, D. and Goldfarb, D., *J. Chem. Soc., Chem. Commun.*, 875 (1995).

24. Tanev, P.T., Chibwe, M., and Pinnavaia, T.J., *Nature*, **368** 321 (1994).

25. Cheng, C.F. and Klinowski, J., *J. Chem. Soc., Faraday Transactions*, **92** 289 (1996).

26. Morey, M., Davidson, A., Eckert, H., and Stucky, G., *Chem. Mater.*, **8** 486 (1996).

27. Bagshaw, S.A., Prouzet, E., and Pinnaia, T.J., *Science*, **269** 1242 (1995).

28. Reimers, J.N. and Dahn, J.R., *J. Electrochem. Soc.*, **139** 2091 (1992).

29. Ohzuku, T., Iwakoshi, Y., and Sawai, K., *J. Electrochem. Soc.*, **140** 2490 (1993).

30. Dahn, J., *Phys. Rev.*, **B44** 9179 (1991).

31. Fong, R., can Sacken, U., and Dahn, J., *J. Electrochem. Soc.*, **137** 2009 (1990).

32. Dahn, J., Sleigh, A., Shi, H., Way, B., Eydanz, W.W., Reimers, J., *Lithium Batteries*. Industrial Chemistry Library, ed. G. Pistoia. Vol. 5. 1994, Amsterdam and London: Elsevier.

33. Dahn, J.R., Sleigh, A., Shi, H., Reimers, J., Zhong, Q., and Way, B., *Electrochim. Acta*, **38** 1179 (1993).

34. Xu, J., Myrtle, K., and Dahn, J., *J. Electrochem. Soc.*, **142** 2927 (1995).

35. Tran, T., Feikert, J., Song, X., and Kinoshita, K., *J. Electrochem. Soc.*, **142** 3297 (1995).

36. Matsumura, Y., Wang, S., and Mondori, J., *J. Electrochem. Soc.*, **142** 2914 (1995).

37. Satoh, A., Takami, N., and Ohsaki, T., *Solid State Ionics*, **80** 291 (1995).

38. Aurbach, D. and Ein-Eli, Y., *J. Electrochem. Soc.*, **142** 1746 (1995).

39. Shu, Z., McMillan, R., and Murray, J., *J. Electrochem. Soc.*, **140** 922 (1993).

40. Sawai, K., Iwakoshi, Y., and Ohzuku, T., *Solid State Ionics*, **69** 273 (1994).

41. Sata, K., Noguchi, M., Demachi, A., Oki, N., and Endo, M., *Science*, **264** 556 (1994).

42. Imanishi, N., Kashiwagi, H., Ichikawa, T., Takeda, Y., and Yamamoto, O., *J. Electrochem. Soc.*, **140** 315 (1993).

43. Aurbach, D., Ein-li, Y., Chusid, O., Careli, Y., Babai, M., and Yamin, H., *J. Electrochem. Soc.*, **141** 603 (1994).

44. Fauteux, D. and Koksbang, R., *J. Appl. Electrochem.*, **23** 1 (1993).

45. Kanno, R., Shirane, T., Kawanoto, Y., Takeda, Y., Takano, M., Ohashi, M., *J. Electrochem. Soc.*, **143** 2435 (1996).

46. Morzili, S., Scrosati, B., and Sgarlata, F., *Electrochim. Acta*, **30** 1271 (1985).

47. Murphy, D.W., DiSalvo, F.J., Carides, J.N., and Waszczak, J.V., *Mat. Res. Bull.*, **13** 1395 (1978).

48. Holmes, R.W. *LiSn Anode.* in *Proceedings of the ECS Symposium on Lithium Batteries*. 1984. Pennington, NJ.

49. Shacklette, L.W., Maxfield, M., Gould, S., Wolf, J.F., Jow, T.R., and Baughman, R.H., *Synth. Met.*, **18** 611 (1987).

50. Stromme, M., Isidorsson, J., Niklasson, G.A., and Granqvist, C.G., *J. Appl. Phys.*, **80** 233 (1996).

51. Maekava, Y., Myasaka, T., Kagawa, O., and Matsufuji, A., *Secondary Nonaqueous-Electrolyte Lithium Batteries with Improved Anodes*, in *Kokai Tokkyo Koho*, Ed. 1995, Fuji Photo Film: Japan.

52. Ishizuka, H. and Tomiyama, H., *Tin Anode*, in *Fuji Photo Film Co. Ltd.*, JP 03,982,788. 1997: Japan.

53. Nakajima, Y., Nakamatsu, S., Shimamune, T., and Matsuda, Y., *Tin Oxide as Anode in Lithium Battery*, in *Denki Kakagu Oyobi Kogyo Butsuri Kagaku*, JP 1,272,049. 1997, Permelec Electrode Ltd.: Japan.

54. Kloster, G.M., Thomas, J.A., Brazis, P.W., Kannewurf,C.R., and Shriver, D.F., *Chem. Mater.*, **8** 2418 (1996).

55. Guerard, D. and Herold, A., *Carbon*, **13** 337 (1995).

56. de Picciotto, L.A., *Solid State Ionics*, **62** 297 (1993).

57. Sato, K., Noguchi, M., Demachi, A., Oki, N., and Endo, M., *Science*, **264** 556 (1994).

IMAGE EVALUATION
TEST TARGET (QA-3)

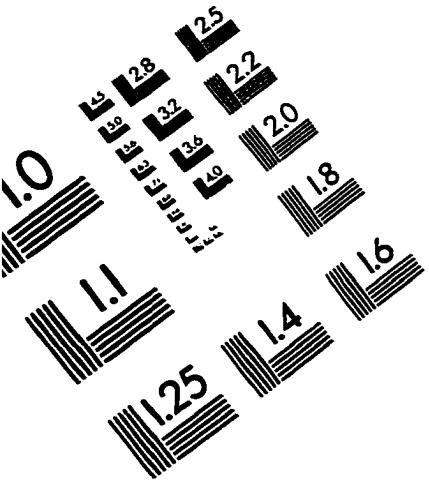

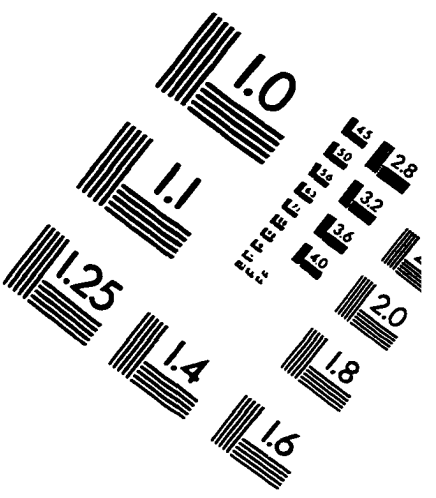

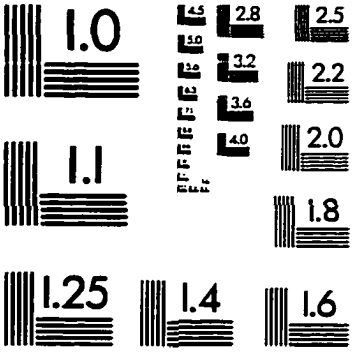

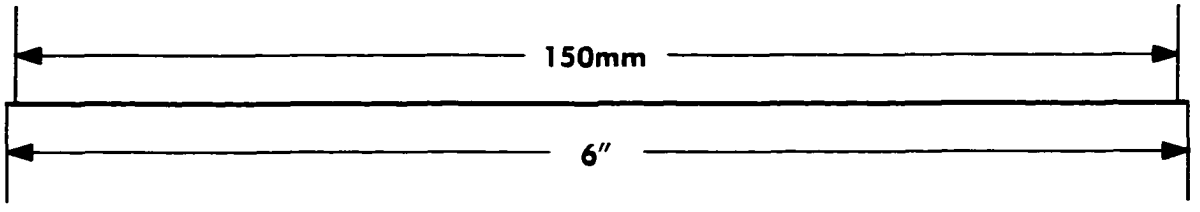

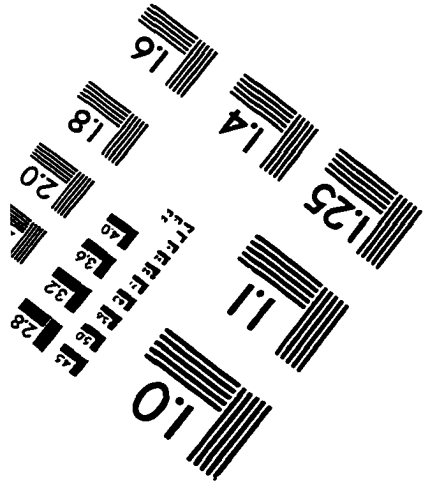

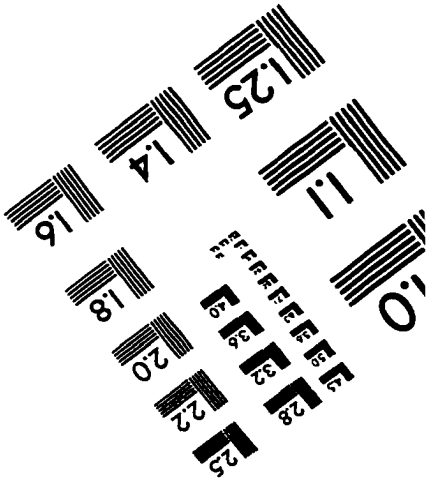

APPLIED IMAGE, Inc
1653 East Main Street
Rochester, NY 14609 USA
Phone: 716/482-0300
Fax: 716/288-5989